Directed Biomolecular Assembly of Functional Nanodevices

Erika Penzo

Submitted in partial fulfillment of the
requirements for the degree of
Doctor of Philosophy
in the Graduate School of Arts and Sciences

COLUMBIA UNIVERSITY

2014

ABSTRACT

Directed Biomolecular Assembly of Functional Nanodevices

Erika Penzo

One of the objectives of nanotechnology is to develop ways to build functional nanoscale devices from nanostructures. Whether these nanodevices will constitute the basis for new technologies rests on the ability to precisely manipulate the nanostructures in such a way that large numbers of functional devices can be built in parallel, with each nanodevice precisely located and addressed.

In this work nanostructures dispersed in solution are organized onto surfaces by means of molecular-scale directed assembly. This technique combines top down high resolution lithographic patterning to bottom up self-assembly: specific molecular interactions take place at locations precisely defined by lithography, resulting in the parallel assembly of an arbitrarily large number of devices into complex and precisely ordered arrangements. While different molecules are used in this study, DNA plays a key role throughout the work due to the specificity of its interactions, its programmability and outstanding chemical flexibility.

Two approaches are developed to direct the assembly of nanostructures on a surface. The first involves the patterning and selective functionalization of metallic nanodots that are used as anchors for the attachment of DNA molecules, proteins, DNA nanostructures and single-wall carbon nanotube

(SWCNT) segments wrapped by DNA. Different strategies are explored to maximize the yield of the desired assembly. This platform also allows the monitoring of DNA-protein interactions with single molecule resolution, which has many potential biomedical applications. In the second approach, lithographic patterning is used to define regions of high surface energy that promote the binding of DNA origami and SWCNT segments. The high patterning resolution again allows for single nanostructure manipulation. This method facilitates the assembly of SWCNT field effect transistors from DNA-wrapped SWCNT segments.

The formation of multi-component nano-objects in solution, by directing the linkage of properly functionalized nanostructures, is also studied. The products of these reactions are suitable for surface placement with the developed directed assembly techniques, thereby resulting in a hierarchical directed assembly process. Among others, the synthesis of SWCNT-dsDNA heterostructures is described. These hybrid objects can be used to electrically probe dsDNA using the SWCNTs as electrodes, by assembling solid state devices by means of the directed assembly methods, and also by conductive AFM. The results of some electrical measurements of double stranded DNA are discussed.

The techniques developed in this thesis are directly applicable to fundamental studies of electron transport in molecules and other nanostructures, but they also have utility in other fields, such as chemistry and biology, where single molecule resolution is required. In addition, the approaches developed in this work may facilitate the advancement of new electronics technologies, including, but not limited to, future circuits based on single-wall carbon nanotubes with specific electronic properties.

Table of Contents

List of figures

List of tables

Acknowledgments

First of all, I would like to thank my advisor, Prof. Shalom Wind, for patiently guiding me through these years of scientific research. Working with/for him has been a great pleasure, and I am firmly convinced that, if I didn't have the privilege to deal with such a nice and intelligent person, I probably would not have made it to the end. He has been able to gently and knowledgeably direct me along my PhD, giving excellent explanations and suggesting crazy ideas, and always being available to talk about experiments that were inevitably never working the way they were supposed to. He has been encouraging when my hypercritical side was coming out (does it ever not come out?) and has calmly dealt with me getting into the "nothing is ever gonna work" mood. Very importantly for my mental sanity, he has never been pushy, and he has always given me the space and freedom that my indomite nature needs. He has never stopped believing in my capability and talents, especially when I was the one giving up faith in them. I am very grateful for all the excellent opportunities that he gave me: the many interesting conferences that he encouraged me to attend (oftentimes in fabulously exotic parts of the world) and the great trips to visit collaborators and work in their labs, where I not only learnt a great deal about different ways of doing science, but I also found friends and mentors, and I got to discover different cultures. I also would like to thank him for the frank and honest relationship that we have maintained during these six years, and that I know will continue in the future.

Many other people contributed to my doctoral adventure and listing all of them is going to be hard. Dr. Matteo Palma taught me everything I know about

surface chemistry and was a great partner in crime. He has been very much missed after he went back oversea to start his career as a chemistry professor. Dr. Risheng Wang has been my DNA bible and has never lacked a smile, even when she had to experience some of my dark moods (sorry Risheng!). Dr. Mark Schvatzman taught me everything I know about nanofabrication (starting from level zero, six years ago) and noticeably he did it applying my father's methods: "What doesn't kill you, makes you stronger." I grew up with that stuff! Haogang Cai was the best student I have ever had and he has way surpassed his teacher in becoming an expert nanofabricator. I wish him great success in his research and in his career. Dr. Teresa Fazio has been an awesome lab-mate, kind and professional, and always fun to work with. And she had the cutest dog, which accompanied me in many relaxing walks around Columbia. I would like to thank the members of my lab: the hyper energetic Diego Scarabelli, who has always been ready to help me, Simon Vecchioni and Jinyu Liao, for patiently listen to my long and detailed explanations.

I would like to thank Prof. James Hone for giving me a desk in his lab, for letting me use all the equipment, and for making me feel like a member of the lab. There are many Hone Lab students and postdocs (present and past) that I need to thank for the help in many occasions, and for the interesting conversations, about science, and not. Thanks Adam Hurst, Daniel Chenet, Ghidewon Arefe, Sunwoo Lee, Alexander 'Sasha' Gondarenko, Justin Abramson, Arend van der Zande and Zhengyi Zhang. A special thank goes to Nick Petrone, because he has really taught me plenty about engineering and clean room processes, and because he was always ready to drop everything and help me

when somehow I found myself in the middle of disaster. He is also always ok putting up with the worse of me, and he is a champ in cheering me up.

I would like to thank Prof. Michel Sheetz for letting me work in his lab, which is full of good bio equipment and fun people. Thanks in particular to my friends Luis Santos and Thomas Iskratsch for the great chat breaks.

I am grateful to Prof. Nuckolls for letting me work in his lab and to Prof. Latha Venkataraman and Prof. Aron Pinczuk for the good teachings and advice.

I would like to thank some collaborators outside Columbia University for opening the doors of their laboratories, for allowing me to work with them and to learn from their expertise: Prof. Jennifer Cha and Dr. Albert Hung at UCSD, and Prof. Danny Porath, Dr. Dvir Rotem, Gideon Livshits, Dr. Haichao Huang and Avigail Slutzkin at Hebrew University.

There are many friends that I need to thank: in particular Clara Orbe, Sarah Goler, Alice Gavin, Giulia Paoletti and Ryan Cooper, for their support, their wisdom, and all the fun we shared.

Finally I want to thank my parents Maria Teresa and Edoardo for always supporting me and especially for giving me complete freedom, in any occasion, when choosing the path I thought was best for my life. At last I want to thank my grandma Rosi, for raising me, for loving me unconditionally and for teaching me math, since early age, while rolling tagliatelle.

To my parents, Maria Teresa and Edoardo, because without their support I would have never made it here; and to Nick, the best companion in this adventure.

Chapter 1

Introduction

During the past few decades, intense research in the fields of nanoscience and nanotechnology produced a variety of nanosized materials, or nanostructures, displaying unique electronic, optical, magnetic, mechanical, thermal and chemical properties. Examples are nanoparticles, quantum dots, nanowires, nanorods, fullerenes (carbon allotropes, such as carbon nanotubes and graphene), as well as biomolecule-based nanostructures (e.g., DNA origami). The properties of these nanostructures that generally attract the most interest are largely a result of quantum confinement: the nanoscale dimensions, and therefore relatively small number of atoms/molecules constituting the objects, produce completely novel behaviors that are unseen in their macroscopic counterparts [1, 2]. One of the goals of nanotechnology is to develop ways to build nanodevices that, by taking advantage of the unique characteristics of nanostructures, are capable of highly improved and/or entirely new functionalities.

Much work has been done in the past several years investigating the properties of myriad new nanodevices, usually by employing serial techniques, i.e. making one (or a few) devices at the time. Present day technologies, though, are comprised of large numbers of elements combined together into highly complex architectures, which ultimately lead to their powerful capabilities. New technologies based on nanoscale devices should outperform existing technologies but should also be integratable with them. In doing so the main obstacles are a matter of reliability and organization. Since the properties of nano-objects are highly dependent on their atomic structure, the realization of devices that are able to consistently operate in the same way requires extremely pure and homogeneous nanostructures to start with. This implies the need for synthesis methods with high purity yield and/or sufficiently capable purification techniques. In order to obtain reliable nano-devices the use of uniform nanostructures is not sufficient. A working device is usually made by combining the nanostructures with other components and, again, this needs to be done with nanoscale precision to obtain uniform functioning. The development of new technologies utilizing nanoscale devices will necessitate the ability to precisely manipulate nanostructures in building large numbers of functional devices in parallel. Each nanodevice must be precisely located and addressed.

It is this last issue that constitutes the topic of this thesis. The main technique studied is molecular-scale directed assembly, in which high resolution lithographic patterning is combined with self-assembly. Lithography 'guides' the

parallel assembly of an arbitrarily large number of devices into complex and precisely ordered arrangements.

The focus will be in how to utilize nanostructures that are either synthesized or dispersed in solution to create large arrays of individually addressable nanodevices on a surface. The choice of using nanostructures in solution, instead of, for example, directly growing them, is dictated by the chemical flexibility of the solution state, the higher compatibility with other processing techniques (since there is no requirement for high temperature) and the fact that a wide variety of nanostructures are synthesized in solution or can be easily solubilized. Moreover, for many nanostructures, effective purification techniques have been developed in solution, whereas direct growth hasn't demonstrated the ability of producing monodisperse samples yet.

The key principle underlying molecular-scale directed assembly is to use lithographic patterning to precisely define specific sites on a surface where selected molecular interactions take place, resulting in the placement/assembly of a nanospecies of choice on the surface in the desired locations by means of molecular recognition.

While many different molecules may be used for the type of assembly considered here, DNA plays a key role throughout the work due to the specificity of its interactions, its programmability and outstanding chemical flexibility. These properties have made DNA a particularly intriguing material for potential future technological applications.

Even before considering future technological applications, the techniques developed in this work would benefit many fundamental studies (in fields ranging from physics to chemistry to biology). All of them require a large number of data to generate statistically significant data that can establish a particular pattern. Current methods often rely on ensemble measurements. Nanoscale devices can enable the observation of phenomena at the single nanostructure or molecule level, revealing mechanisms that are not visible from macroscopic samples. Having large arrays of nominally identical and individually addressable devices yield data that would never be practically available with conventional (serial) methods.

As a final note, a wide range of nanoscale materials is already found in nature, mostly in solution. Proteins and viruses are some examples and, as just mentioned, DNA is a particularly interesting one. Nowadays there is a great deal of activity aimed at applying techniques from the physical sciences in biology and medicine, and the methods developed in this thesis are well suited to this endeavor.

The next three sections review the fundamentals of the two primary nanomaterials studied in this work, i.e. DNA and carbon nanotubes, together with previous work in directed assembly.

1.1 DNA in nanotechnology

Beyond its central role in biology, DNA has recently attracted considerable interest as a technological material.

1.1.1 The DNA structure

With a diameter of 2 nm in its double stranded form, and a 3.4 nm length for a complete 10-base helical turn, DNA is intrinsically a nanomaterial. DNA is a biopolymer, its fundamental units are the two purine bases adenine (A) and guanine (G) and the two pyrimidine bases cytosine (C) and thymine (T). An enormous amount of structural information is encoded its base sequence. The structure of DNA is the well known double helix, discovered by Watson and Crick in 1953. Two single strands are held together by hydrogen bonds between complementary bases (A-T and C-G), leading to the formation of a duplex DNA structure [3].

1.1.2 Chemical and enzymatic manipulation of DNA

A variety of enzymes can react with DNA (and RNA as well). For example, polymerase or reverse transcriptase replicate oligonucleotides, telomerase elongates single nucleic acid strands, and sequence-specific enzymes such as endonucleases or nicking enzymes can cleave DNA at specific locations. These

enzymes constitute a unique "toolbox" for manipulating DNA, and, together with the ability to synthesize any DNA sequence by automated chemical methods and to replicate the products by the polymerase chain reaction (PCR), enable the cost-effective preparation of large quantities of nearly any DNA sequence. Also, ingenious organic synthesis protocols for the preparation of new nucleotide bases [4] and their biopolymers, such as peptide nucleic acids (PNAs) [5] or locked nucleotides (LNAs) [6], introduce new man-made DNA analogues with unique properties. These artificial DNA analogues can be conjugated to native DNA to form hybrid systems exhibiting different properties and functions [7]. In addiction, nucleotides can be chemically functionalized with, for example, redox groups [8], photoactive units [9], chemical functionalities (amine, thiol, azide, etc.), or molecular labels, such as biotin, providing new building blocks for incorporation into the DNA chains. Thus, DNA reveals to be an extremely capable and versatile molecule, an ideal building block for the "bottom-up" self-assembly of nanostructures.

1.1.3 DNA structural nanotechnology

Nadrian Seeman was the first person to envision the possible use of DNA as a structural nanomaterial. In 1982 he wrote: "It is possible to generate sequences of oligomeric nucleic acids which will preferentially associate to form migrationally immobile junctions, rather than linear duplexes, as they usually do." [10] At the time Seeman's aim was to organize proteins in three-

dimensional crystals in order to study their structure with X-ray crystallography. Three decades later DNA has demonstrated utility far beyond the arrangement of proteins into a crystal. Complex DNA nanostructures have been constructed, and DNA has been used to organize a variety of functional nano-objects [11].

When trying to make 2D or 3D structures out of DNA, two problems arise: the need to extend the dimensionality of a material that's topologically 1D, and the necessity for greater rigidity than is provided by the DNA duplex. These problems were addressed with the invention of DNA tiles. DNA tiles are constructs in which DNA duplexes are held together by junction points in which single strands are exchanged and shared among the different duplexes. These junctions allow the nanostructure to span two or three dimensions, with directions determined by the helical turns of the tile, and they also grant the rigidity necessary for the structure to maintain stability. Another feature of DNA tiles is the availability of single-stranded "sticky-ends," which are extensions of a strand beyond its complement. This allows the interhybridization of DNA tiles and their self-assembly into objects of higher complexity [12]. Several examples of DNA tiles are shown in Figure 1.1. Among these are crossover motifs: the double-crossover (DX) [13] structure consists of two helices conjugated along their long axes, while the triple-crossover (TX) [14] structure consists of three double-stranded DNA helices lying in a plane and linked by strand exchange at four crossover points. In 2009 Seeman and co-workers demonstrated the formation of 3D macroscopic DNA crystals from the assembly of DNA tiles; such

crystals are capable of diffracting X-rays to a 4 Å resolution [15].

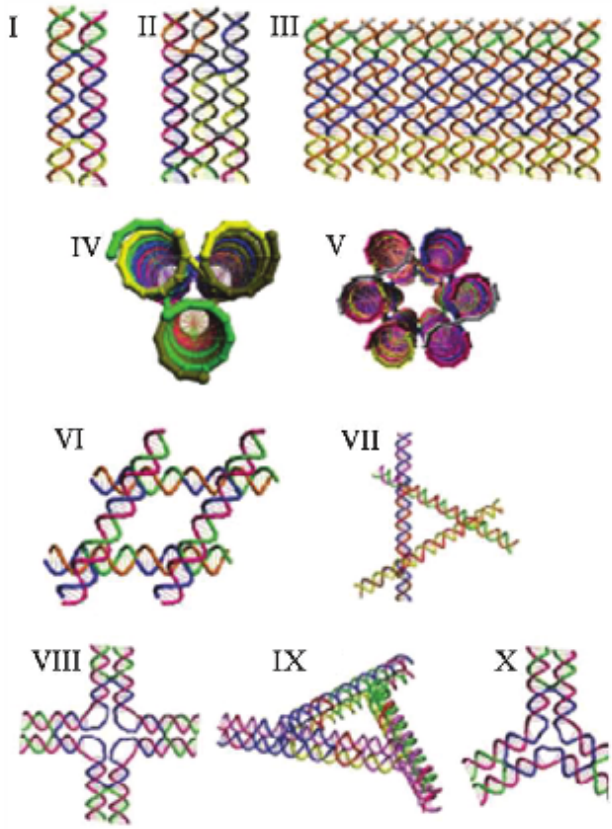

Figure 1.1: Examples of DNA tiles. (I) a double-crossover tile (DX), (II) a triple-crossover tile (TX), (III) a 12-helix tile, (IV) a 3-helix bundle tile, (V) a 6-helix bundle tile, (VI) a rectangular motif composed of four 4-arm junctions, (VII) a triangular motif composed of 4-arm junctions, (VIII) a cross-shaped tile, (IX) a triangular DX tile, and (X) a 3-point star DNA tile. (Figure from Wilner et. al. [16].)

DNA origami, invented by Paul Rothemund in 2005, has proven to be one of the most important developments in structural DNA nanotechnology since the introduction of the crossover motif. DNA origami are formed by folding a long single strand (from the M13 phage genome, ~7,429 nucleotides long) through

the hybridization with hundreds of short 'staple' strands [17]. As shown in Figure 1.2, complex shapes can be precisely obtained just by programming the base sequences of the staples. Specialized computer software is available for the design of DNA origami shapes [18].

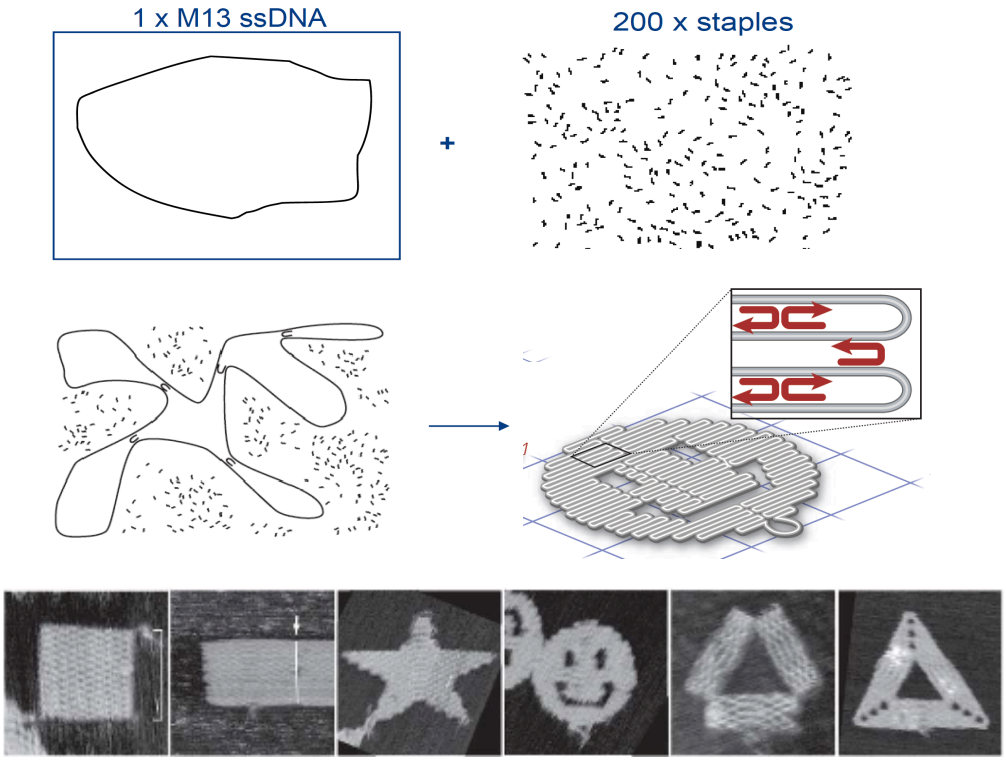

Figure 1.2: (Top) Schematic of the DNA origami assembly. (Bottom) AFM images of some 2D DNA origami. (Figure adapted from Rothemund et. al. [17].)

Three strategies have been developed to extend DNA origami to the third dimension. One relies on folding interconnected individual or continuous DNA origami sheets into hollow 3D cages [19]. Another method builds 3D shapes by constraining layers of helices to a honeycomb [20] or square lattice [21]; the

targeted insertion and deletion of base pairs within such blocks allows the making of twisted and curved 3D objects [22]. The third strategy is to stack concentric double-helical circles having differing circumferences, reflecting the different numbers of turns they are made of, so that they match the rounded contours of a target object [23]. Recently complex 2D shapes, similar to the ones produced by the origami technique, have been demonstrated with a tile approach [24].

1.1.4 DNA nanostructures as scaffolds

Taking advantage of their sequence specificity and the resulting spatial addressability, many of the DNA nanoarchitectures listed above have been used for the organization of smaller nanostructures. 2D arrays of DNA tiles were used to organize nanoparticles (NPs), proteins and antigen-antibody complexes in 2D crystals.

Four different DX tiles were designed to self-assemble into 2D lattices by sticky-end cohesion (Figure 1.3A). One of the tiles contained a protruding single strand, modified with a thiol group on its 5' end. Au NPs (1.4 nm in diameter) modified with a maleimide residue were covalently linked to the thiol-functionalized tile and the subsequent hybridization of the four tiles resulted in the assembly of Au-nanoparticles ordered arrays [25]. Similarly, making use of the specificity of sticky-end cohesion, Au NPs of different sizes were assembled on a 2D DNA scaffold, consisting of four different tiles, through base-pairing

hybridization [26] (Figure 1.3C). Two 3D DX triangle tiles were designed to produce, upon their self-organization, a rhombic lattice arrangement [27] (Figure 1.3F). Two sides of the equilateral tile contained sticky-end domains that enabled the self-organization of the nanostructure. The third side included a thiolated functionality to which Au NPs could be linked. By the mixing of the two types of tiles, 2D arrays with ordered Au NPs arrangements were prepared. In the same way, arrays of antibodies or proteins were obtained by incorporating in the DNA tiles functional groups capable of associating with the protein or antibody of interest (e.g. fluorescein antigen/antifluorescein antibody [28] or biotin/streptavidin [29]). In a related study, a DNA Kagome lattice was used as a template for the organization of proteins, and the single-molecule imaging of the proteins was demonstrated [30].

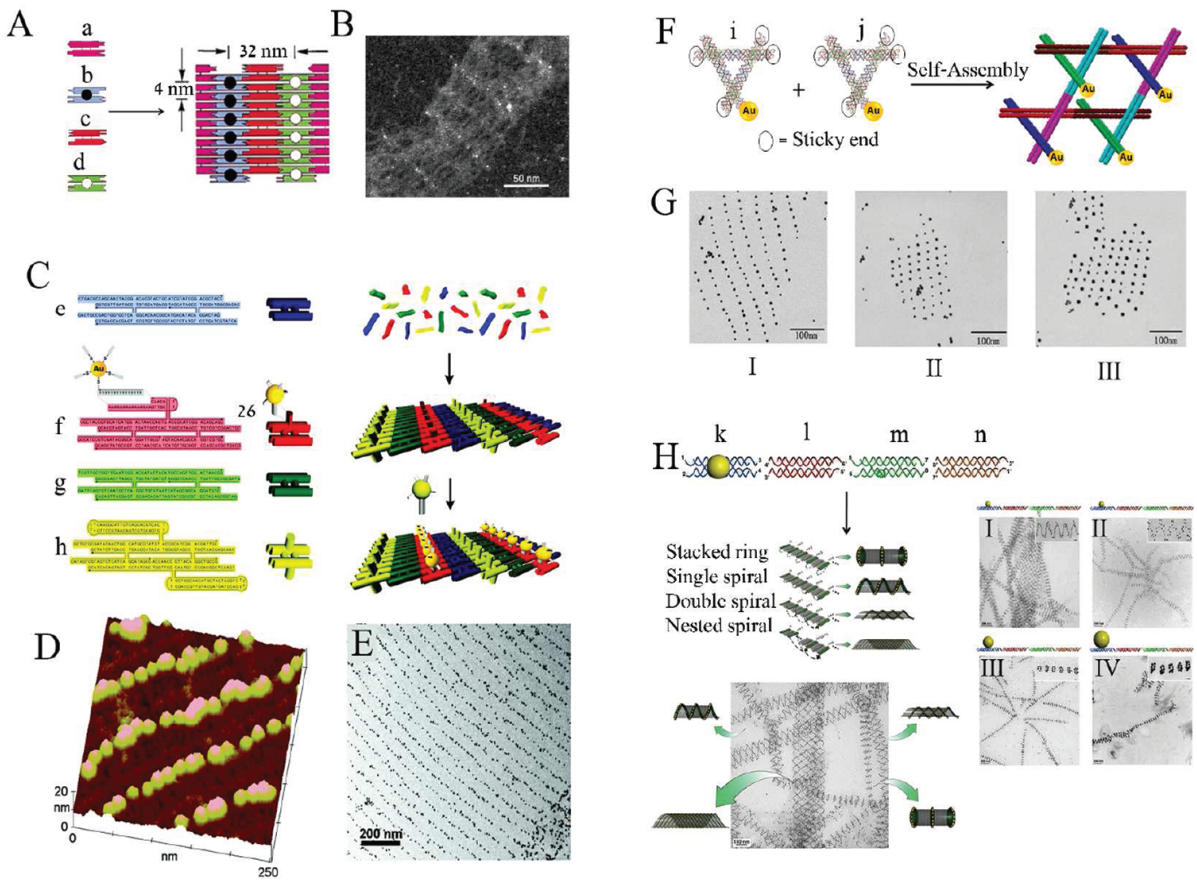

Figure 1.3: (A) Self-assembly of a 2D DNA nanostructure consisting of four complementary double-crossover tiles that include on tile b a protruding thiolated nucleic acid for the programmed immobilization of Au NPs. (B) TEM image corresponding to the spatially ordered Au NPs on the 4-tile 2D DNA array. (C) The self-assembly of four double-crossover tiles e-h, where tile f includes a protruding nucleic acid tether, and the secondary hybridization of Au NPs (6 nm) functionalized with a nucleic acid complementary to the protruding tether to yield a spatially ordered array of NPs. (D) AFM image of the resulting Au NPs array. (E) TEM image of the resulting Au NPs array. (F) Self-assembly of two different triangular tiles i and j, each consisting of three-dimensional double-crossover units and modified with Au NPs. (G) TEM images corresponding to (I) the 2D array formed by tiles i modified with 5 nm Au NPs and the bare tiles j. (II) The 2D array formed by tiles i and j modified with 5 nm Au NPs. (III) The 2D array formed by tiles i modified with 5 nm Au NPs and tiles j modified with 10 nm Au NPs. (H) Self-assembly of an antigen-functionalized 4-arm tile into a tetragonal square array, and the ordered binding of an antibody to the antigen sites. On the left, AFM images of the antigen-modified array and of the array functionalized with the antigen-antibody complexes. (Figure adapted from Wilner et. al. [16].)

The DNA origami structure can display patterns of binding sites with 6 nm resolution. This property has been utilized to organize NPs, quantum dots (QDs), proteins and carbon nanotubes (CNTs).

Au NPs were incorporated into rectangular origami structures by linking the NP to one or more of the staple strands. Alternatively Au NPs were functionalized with ssDNA complementary to sticky-ends on a triangular DNA origami, and they were hybridized to the already formed origami triangle. This method realized the ordered assembly of Au NPs of variable sizes (15, 10, and 5 nm) by functionalizing the NPs with different ssDNA sequences [31].

CdSe/ZnS quantum dots (QDs), 15-20 nm in diameter, were also assembled on DNA origami by means of a biotin/streptavidin linker. Biotinylated staple strands on specific locations linked streptavidin-labeled QDs [32]. The simultaneous assembly of ssDNA functionalized Au NPs and streptavidin-labeled QDs, on the opposite sides of a DNA origami triangle, exhibiting complementary sticky-ends and biotin groups, was also demonstrated [33].

A rectangular DNA origami was also used to assemble CNT segments perpendicularly on opposite side of the scaffold (Figure 1.4). The CNT segments were wrapped in ssDNA with protruding portions complementary to the sticky-ends on the DNA origami. The resulting CNT 'cross' was electrically characterized by placing it on a Si substrate and connecting the nanotubes to Au/Pd electrodes. Field effect transistor (FET) behavior was observed [34].

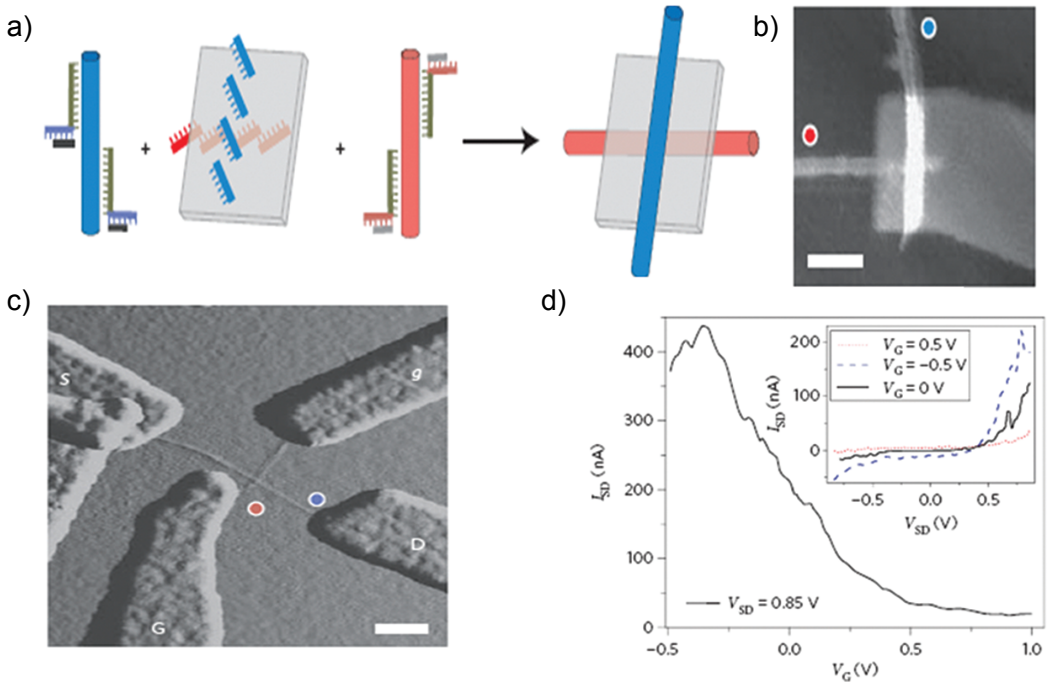

Figure 1.4: (a) Schematic of CNT attachment to rectangular DNA origami with protruding tethers above and below the origami plane. Carbon nanotubes (CNTs) were wrapped with nucleic acids that included sticky-ends with specific complementarity to the tethers above and below the origami plane. This resulted in the orthogonal deposition of the CNTs on the respective domains. (b) AFM height image of the CNTs of the resulting origami/CNTs hybrid. (c) AFM amplitude image of the origami-CNTs nanostructure deposited on a four-microelectrode pattern. (d) Current-voltage curve of the resulting device demonstrating transistor behavior. (Figure adapted from Wilner et. al. [16].)

The origami scaffold was also used for the distance-dependent multivalent ligand-protein binding and for driving specific reactions with precise positioning of proteins at the single molecule level [35, 36].

Several of these DNA-directed assemblies have led to unique and improved functional properties, such as increased enzyme-cascade activities [37, 38] due to spatially positioned enzyme pairs, and shifts of surface plasmon resonance

controlled by custom arrangement of nanoparticles [39-41] through DNA-mediated self-assembly.

The controlled aggregation of DNA-modified Au NPs led to the formation of crystalline NPs structures [42, 43]. Both face-centered cubic (fcc) crystalline structures and body-centered cubic (bcc) crystalline structure of Au NPs were demonstrated.

These examples of DNA assembly demonstrate the utility and versatility of this new technology.

1.1.6 DNA in nanoelectronics

As silicon transistor scaling, as prescribed by Moore's law, proceeds towards its anticipated end some time in the next decade or two [44], the semiconductor industry is faced with the necessity of developing alternative technologies to silicon that are capable of producing improved electronic function. One approach is to use DNA to template the assembly of nanodevices and nanocircuits.

In one example, DNA-based nanoelectronic systems were created by DNA metallization or by specific attachment of semiconductors to DNA scaffolds. A λ phage DNA was stretched between two microelectrodes, by hybridizing it to the ssDNA protruding from the electrodes. Ag^+ ions were associated with the phosphate groups of the λ phage DNA, they were reduced to Ag^0 nanoclusters

by hydroquinone under base conditions, and enlarged by a catalytic electroless deposition of silver, leading to the formation of a continuous Ag nanowire [45]. The I-V curves of the resulting metallic nanowire showed a non-ohmic behavior probably due to defects in the contacts between the metallic nanoclusters composing the nanowire itself. The formation of addressable conductive domains on DNA templates and the fabrication of DNA templated carbon nanotube transistors were demonstrated as well [46]. This task was accomplishing by employing the bacterial protein RecA, which participates in gene repair and homologous recombination, as an organizing element of the nanodevice (Figure 1.5). A single-stranded DNA was coupled with the RecA protein, and the resulting complex was incorporated into an addressed domain of a long duplex DNA through homologous recombination, to yield a duplex DNA patterned with RecA. The incorporation of nanotubes onto the duplex DNA template was achieved by first binding biotinylated anti-RecA to the protein, and then attaching streptavidin-modified carbon nanotubes. The further modification of the protein-free duplex DNA domains with Ag^+ ions, their reduction to nanoclusters, and the electroless catalytic deposition of Au on the Ag nanoclusters, yielded electrical contacts that were separated by the semiconducting carbon nanotubes. With similar approaches, the selective deposition of Pd [47] and CdS [48] on DNA was achieved as well, resulting in the formation of DNA templated metallic or semiconducting nanowires.

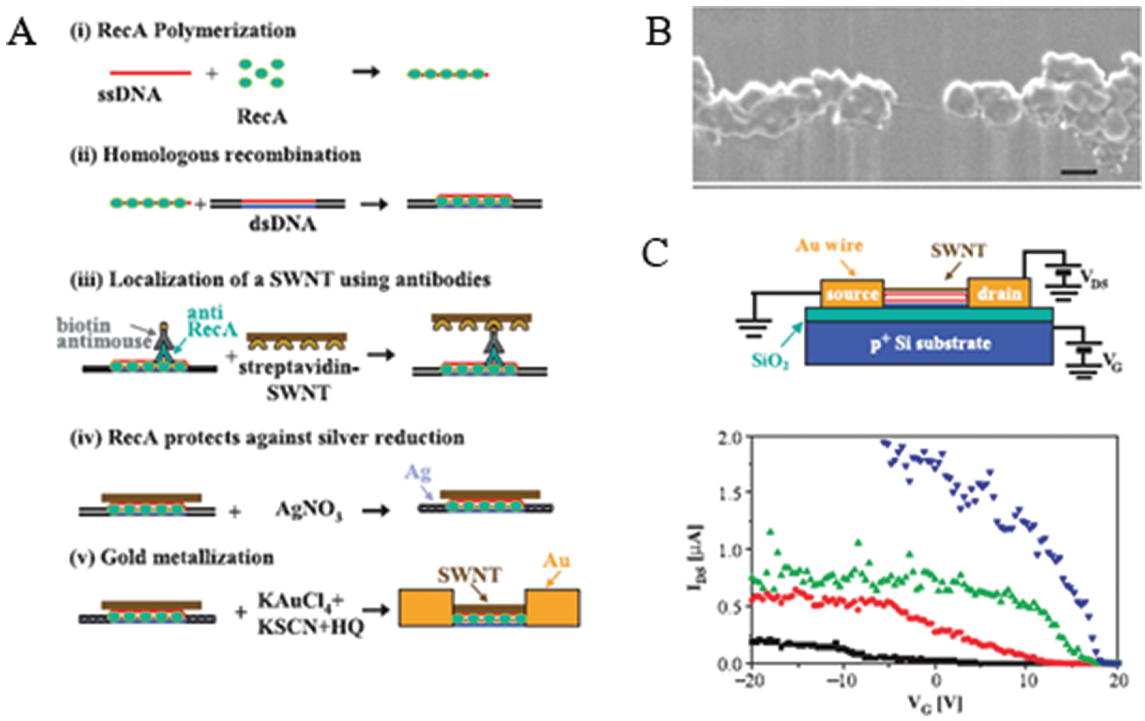

Figure 1.5: (A) Stepwise assembly of a nanotransistor by the ordered deposition of a CNT on Ag metallic patterns generated on a DNA template. (B) SEM image of a CNT bridging the Ag nanowires deposited on the DNA template. (C) Schematic of the device and experimental I-V curves at different source-drain potentials. (Figure from Wilner et. al. [16].)

It has been proposed that DNA itself might be capable of transporting electrical current, behaving either as a conductor or as a semiconductor [49]. Many experiments have been performed in an attempt to gain insight into the electron transport properties of DNA. A wide range of conductivity values have been reported, varying from insulating to superconducting, probably depending on the very different conditions in which the experiments were performed [50]. Recently transport through individual DNA duplex strands has been probed using CNTs as electrodes [51]. The binding between the CNT and the DNA

molecule was a covalent amide bond resulting from the interaction of carboxyl groups on the CNT and amine groups at the ends of the DNA molecule. This experiment gave clear evidence of DNA conductance that could be modulated by introducing a base-pair mismatch into the DNA.

1.2 Carbon nanotubes

Carbon nanotubes (CNTs) are hollow cylinders whose walls are made of one or more sheets of graphene (i.e. a single layer of carbon atoms in sp^2 configuration arranged in a honeycomb lattice). CNTs can be single-wall (SWCNTs) or multi-wall (MWCNTs) but only the first kind will be considered in this thesis.

SWCNTs demonstrate excellent electrical, optical, chemical and mechanical properties. They hold great potential for a wide range of applications in solid state devices and are considered as one promising candidate for beyond-silicon electronics.

1.2.1 SWCNT electronic structure

SWCNT diameters typically range between 0.5 and 2 nm while their length can reach centimeters; this small diameter and high aspect ratio make them a quasi one dimensional structure with respect to nearly all electron processes and result in quantum confinement effects. As is the case for most nanomaterials,

the electronic properties of SWCNTs are highly dependent on their atomic structure, which is in turn uniquely defined by the chiral vector, $\boldsymbol{C_h}$, spanning the diameter of the tube:

$$\boldsymbol{C_h} = n\hat{\boldsymbol{a}}_1 + m\hat{\boldsymbol{a}}_2$$

where $\hat{\boldsymbol{a}}_1$ and $\hat{\boldsymbol{a}}_2$ are the unit vectors of the graphene honeycomb lattice. In this way, any SWCNT can be described by a pair of integers (n,m) that define its chiral vector (Fig. 1.6a). The nanotube diameter is given by:

$$d_{CNT} = \frac{|C_h|}{\pi}$$

The electrical properties of CNTs can be illustrated starting from the electronic structure of graphene, whose band diagram and hexagonal first Brillouin zone are shown in Fig. 1.6b. The energy surfaces describing the occupied π and unoccupied π^* states touch at six points (Fermi points) lying at the Fermi level. Because of this band structure, graphene is a zero-gap semiconductor: while allowed states exist at the Fermi level E_F, the dimensionality of the system (2D) results in a vanishing density of states when integrating over the Fermi surface. In the case of a tube, the electrons are confined along the circumference of the SWCNT. Owing to the periodic boundary conditions imposed in the circumferential direction, only a certain set of the graphene $\boldsymbol{k}$ states are allowed. The circumferential component of the reciprocal lattice vector $\boldsymbol{k}_\perp$ is quantized and it fulfills the condition:

$$\boldsymbol{k}_\perp \cdot \boldsymbol{C_h} = 2\pi j$$

where $\boldsymbol{C_h}$ is again the chiral vector and j is an integer [52]. On the other hand, the component of the reciprocal lattice vector parallel to the axis of the tube $\boldsymbol{k}_{||}$ is a continuous variable, and the electron motion along the axis is free. As a result, each band of graphene divides into a number of 1D sub-bands labeled by j. The allowed energy states of a SWCNT are 1D sections of the graphene band structure (Fig. 1.6b). When the allowed states of a CNT pass through a Fermi point the tube is metallic, while if no states pass through the Fermi point the tube is a semiconductor [53, 54].

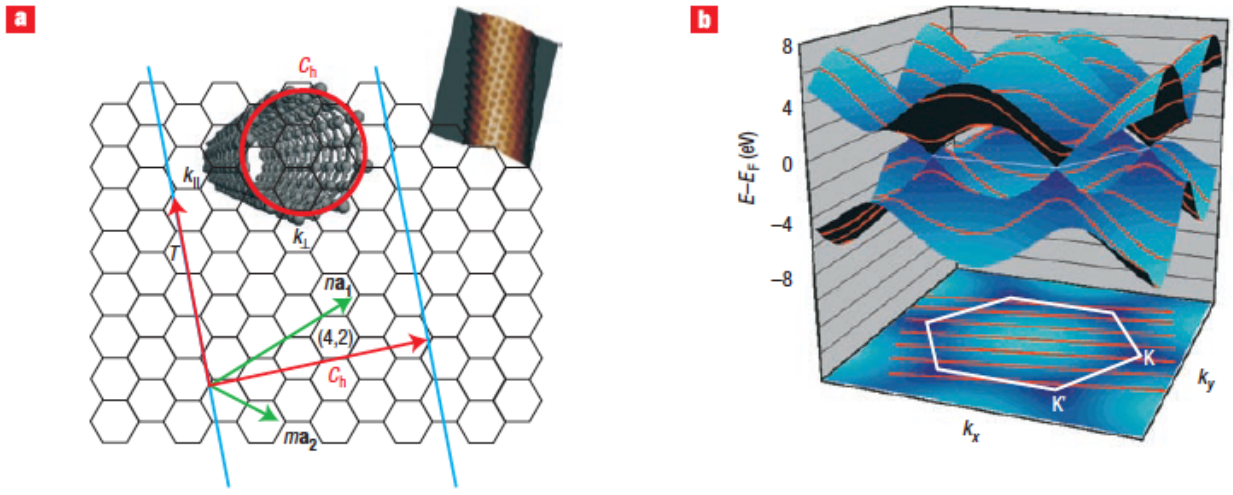

Figure 1.6: The structure of graphene and carbon nanotubes. (a) The carbon atoms in a single sheet of graphene are arranged in a honeycomb lattice. A nanotube can be formed by rolling a ribbon of graphene along a chiral vector, $\boldsymbol{C_h}$, defined by two integers. The insets show the definitions of $\boldsymbol{k}_\perp$ and $\boldsymbol{k}_{||}$ (left), and a scanning tunneling microscope image (right) of a single-walled nanotube. (b) The band structure (top) and Brillouin zone (bottom) of graphene. The valence band (which is of π-character) and the conduction band (π*-character) touch at six points that lie at the Fermi energy, but only two of these points — the K and K' points — are inequivalent. At these Dirac points, the density-of-states of graphene is zero. At low energies, the dispersion is linear, determined by the conical sections involving the K and K' points. The quantization of the

circumferential momentum, $\boldsymbol{k}_{\perp}$, leads to the formation of a set of discrete energy sub-bands for each nanotube (red parallel lines). The relation of these lines to the band structure of graphene determines the electronic structure of the nanotube. If the lines pass through the K or K' points, the nanotube is a metal: if they do not (as in b), the nanotube is a semiconductor. (Figure from Avouris et. al. [55].)

The general rules for the metallicity of the SWNTs are as follows: (n, n) tubes are metals; (n, m) tubes with n − m = 3i, where i is a non-zero integer, are very small gap semiconductors; and all others are large gap semiconductors. Strictly within the band-folding scheme, the n − m = 3i tubes would all be metallic but, because of curvature effects, a tiny gap opens for the case that i is non-zero. Since the band gaps of the large gap and small gap varieties decrease with $1/d_{CNT}$ and $1/(d_{CNT})^2$ respectively, for most experimentally observed carbon nanotube sizes, the gap in the small-gap variety is so small that, for most practical purposes, all the n − m = 3i tubes can be considered as metallic at room temperature [56].

At low energies (i.e. a few hundred meV from the Fermi energy E_F) the band structure of a metallic SWCNT can be approximated by two linear bands intersecting at k_F and -k_F. Electrons with dE/dk > 0 move to the right, while electrons with dE/dk < 0 move to the left. In semiconducting CNTs the two bands do not cross at E_F, but a diameter-dependent band gap develops. In a simple tight-binding model the band gap is given by:

$$E_{GAP} = \left(\frac{4\hbar v_F}{3d_{CNT}} \right)$$

where d_{CNT} is the tube's diameter and v_F the Fermi velocity [57, 58].

The above picture is a single electron model that accounts well for many of the SWCNT ground state properties. Interactions between electrons, however, can modify some of the SWCNT properties, like the band gap size and the nature of the excited states [59].

1.2.3 SWCNT electrical properties

Individual SWCNT can be characterized by a set of electrical properties – resistance, capacitance and inductance – which arise from the nanotube structure and its interaction with other objects.

The SWCNT conductance is given by Landauer's equation [60]:

$$G = \left(\frac{2e^2}{h}\right) \cdot \sum_i^N T_i$$

where $2e^2/h$ is the quantum of conductance and T_i is the transmission of a contributing conduction channel. The sum involves all bands whose energy lies between the electrochemical potentials of the left and right reservoirs to which the nanotube is connected. In the absence of any scattering, i.e. when all $T_i = 1$, the resistance ($R = 1/G$) of a metallic SWCNT is $h/(4e^2) \approx 6.5$ kΩ (as discussed above, $N = 2$ because there are two sub-bands crossing at E_F). This quantum mechanical resistance R_Q is a contact resistance due to the mismatch of the number of conduction channels in the SWCNT ($N = 2$) and the number of

conduction channels of the metallic contacts (N ≈ 10^6 for a 1 μm metal lead) [61]. When this is the only resistance, the transport in the SWCNT is ballistic, that is, no carrier scattering or energy dissipation takes place in the body of the tube. The length over which a SWCNT can behave as a ballistic conductor depends on its structural perfection, temperature and the magnitude of the driving electric field. Under proper conditions, ballistic transport can be achieved over lengths ~ 100 nm [62, 63]. When CNTs are long, or under high bias, many scattering events can take place and the transport is diffusive. In this regime carriers have finite mobility, but this mobility can be very high, as much as 1000 times higher that the one of bulk silicon [55].

In a 1D material scattering by small angles is not allowed, carriers can move only forward or backwards. Since the momentum transfer required for back scattering is high and can only be provided by sharp defects and high energy optical phonons, carrier back scattering is suppressed, especially under low-field conditions [64]. Long-range Coulomb scattering is weak, resulting in an elastic mean free path that can be up to a few microns [65]. On the other hand, the inelastic scattering by low energy acoustic phonons and radial breathing mode (RBM) phonons can be significant [66, 67]. Scattering phase-space restrictions in one-dimensional CNTs result in an inverse relationship between carrier mobility and temperature (1/T) as opposed to the $1/T^5$ behavior in three-dimensional metals. Therefore, at room temperature the low field carrier mobility can be very high. At high bias, energetic electrons can interact with optical phonons resulting in current saturation in metallic SWCNTs [68, 69]

and velocity saturation in semiconducting SWCNTs [70]. At even higher energies, strong electron–electron interactions can induce impact excitation.

The optical phonon scattering mean free path in semiconducting SWCNTs was estimated to be about 10–20 nm, and the saturation velocity of carriers is about 2×10^7 cm/s [70].

In addition to the quantum mechanical contact resistance, there are other sources of contact resistance, such as those produced by the existence of metal-nanotube interface barriers, or poor coupling between the SWCNT and the contacts. These types of resistance strongly depend on the details of the device fabrication, and they can dominate the electrical transport of the nanotubes [55].

The capacitance of CNTs has two components: one is an electrostatic capacitance (C_G) which depends on the device geometry and electric structure; the other is called the quantum capacitance (C_Q), which is related to the density of states and is usually small, ~ 10^{-16} F/μm[71]. The two capacitances combine in series, so that the smaller one dominates ($1/C_{total} = 1/C_G + 1/C_Q$). In most experimental CNT field effect transistors (CNTFETs) C_G is smaller than C_Q, but in a highly miniaturized CNTFET with a high dielectric-constant insulator, C_Q <~ C_G and therefore C_Q can dominate the total capacitance and determine the performance of the device. A small capacitance enables low switching energies, efficient gate coupling, and minimal parasitic capacitance for low-power, high-speed electronics.

The CNT inductance is made of two components as well: the resistance to the change of the electrons kinetic energy gives place to a kinetic inductance (L_K), while the CNT diameter, geometry of the structure and the magnetic permeability of the medium produce a classical inductance (L_c). The total inductance is the sum of the two values, so that the larger inductance, L_K, dominates ($L_K \approx 16$ nH/μm, $L_c \approx 1$ nH/μm) [72].

1.2.4 SWCNT field effect transistors

Transport in semiconducting SWCNTs can be switched 'on' and 'off', making them suitable for the role of the active channel in a transistor. For a transistor, desired properties are high channel mobility, high on/off ratios (10^4 - 10^6) and low off-currents. Additional metrics of device performance are transconductance and sub-threshold swing. Transconductance ($d(I_d)/d(V_g)$) is the variation in drain current (I_d) with respect to gate bias (V_g) at a constant drain bias (V_d), while sub-threshold swing is given by ($d(V_g)/d(\mathrm{Log}(I_d))$), which indicates the variation in gate bias required for an order of magnitude change in drain current. A high transconductance and a low sub-threshold swing are highly desirable for high-speed electronic circuits.

The first carbon nanotube field effect transistors (CNTFET) were reported in 1998 [73, 74]. A single SWCNT bridged two noble metal electrodes prefabricated by lithography on an oxidized silicon wafer. The two metal electrodes worked as source and drain, while the heavily doped silicon wafer itself was used as the

gate (back-gate). These CNTFETs behaved as p-type FETs, due doping by atmospheric absorbates like oxygen. They had an I_{on}/I_{off} current ratio of ~10^5, but they demonstrated a high parasitic contact resistance (≥1 MΩ), low drive currents (a few nA), low transconductance $g_m \approx 1$ nS, and high inverse subthreshold slopes $S \approx 1–2$ V/decade. To a large extent the unsatisfactory characteristics were due to bad contacts. The CNT was simply laid on the gold electrodes and was held by weak van der Waals forces.

Electrical contacts are one of the crucial aspects of CNTFETs functioning. The different work functions of the metal and the CNT lead to transfer of charge at their interface. The resulting interface dipole produces a Schottky barrier [75]. The alignment of the Fermi levels of the metal and CNT, and therefore the Schottky barrier height, depend on their respective work functions (Φ), the CNT bandgap and the details of chemical bonding at the interface. There are two Schottky barriers in a FET: one at the source and another at the drain. As long as one of the barriers is much higher than the other, the FET operates as a unipolar device; that is, it transports one type of carrier: electrons, or holes. Contacts made with metals with low or high work functions result in nearly barrier-free contact for electrons or holes, respectively. n-type or p-type FETs can thus be obtain from a CNT by choosing the proper metal for the contacts. Pd for example, forms a nearly ohmic contact for holes [62]. Due to the 1D character of CNTFETs, the contact Schottky barrier can be made thin enough that the transport through the CNT-metal interface becomes dominated by tunneling [76]. In thin gate oxide CNTFETs the barriers can be thin enough to

allow, depending on the bias, injections of either electrons or holes, or both, simultaneously, resulting in an ambipolar transistor [75]. Control of the Schottky barrier thickness has been demonstrated either by doping of the contacts [77] or by using independent gates [78].

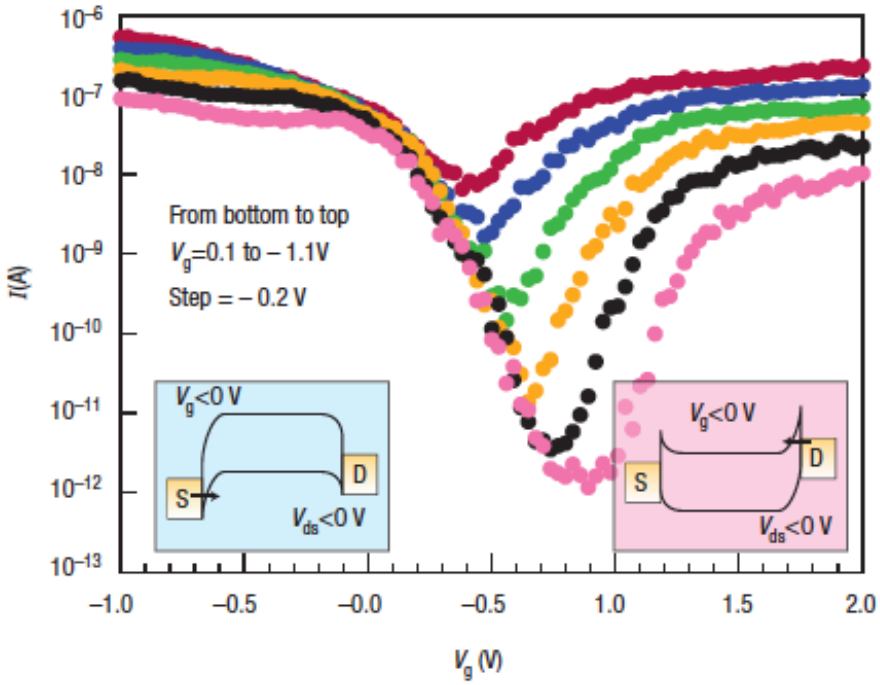

Figure 1.7: Ambipolar transfer characteristics (current versus gate voltage) for a single nanotube transistor. Drain bias increases from –0.1 V to –1.1 V in –0.2 V steps. Left inset: schematic of the band structure of a Schottky barrier semiconducting CNT in a FET under negative gate bias. Holes are injected from the source (S). Right inset: under positive gate bias electrons are injected from the drain (D). (Figure adapted from Avouris et. al. [55].)

Considerable improvement has been made on early devices. State of the art CNTFETs have channels scaled down to 10 nm [79], top gates made with thin high-*k* dielectrics (like ZrO_2 or HfO_2) [69, 80] or 'wrap around' gates [81]. They

demonstrate current ratios up to 10^7 and transconductance as high as 30 μS [69]. A sub-threshold swing lower than the thermal limit (40 mV per decade) has been achieved via band-to-band tunneling in dual-gated CNTFETs [82]. The fabrication of CNTFETs have advanced beyond single transistor devices to more complex structures. A 5-stage ring oscillator on a single CNT, with operating frequencies up to 52 MHz, have been built utilizing Pd gates for pFETs and Al gates for nFETs [83]. Further advances in CNT-based circuits have been limited by challenges in organizing CNTs on surfaces in circuit-friendly topologies.

1.2.5 CNT synthesis and sorting

SWCNTs are produced when a carbonaceous feedstock is exposed to a metal catalyst at high temperature. The most common ways of synthesizing SWCNTs include: (1) arc discharge [84], where a plasma is struck between graphite rods; (2) laser ablation [85], where a high-intensity laser beam is focused on a graphite rod; (3) chemical vapor deposition [86], where a gas containing a carbon feedstock is heated in a furnace. Although some progress has been made in controlling the type of tubes formed during growth, none of these synthetic techniques produces identical populations of SWCNTs. The resulting lack of uniformity in the properties of the SWCNT samples is one of the main obstacles for the development of commercially viable electronics technologies using SWCNTs. In an effort to overcome this limitation, post-synthetic sorting schemes, capable of isolating monodisperse groups of SWCNTs, have been

developed. Typically these techniques are based on some chemical reaction in which molecules selectively bind to the CNT based on their electronic type, diameter, length, and chirality. The chemical interaction can be covalent or non-covalent. Non-covalent interactions are preferable because they allow easier recovery of the pristine CNT characteristics. Once attached to CNT of a certain type, the molecules are used to separate these from the rest. Separation techniques include chromatography, ultracentrifugation, electrophoresis, density gradient ultracentrifugation (DGU) and agarose gel methods [87].

DNA is one of the molecules that have shown the best selectivity to different types of CNTs. Single stranded DNA (ssDNA) effectively disperses SWCNT in aqueous solutions by wrapping around the exterior of the tube [88]. The interaction between the SWCNT sidewall and the ssDNA is due to π-stacking: the π orbitals of the CNT interact with the ones of the aromatic DNA basis. Length sorting of DNA wrapped SWCNTs has also been demonstrated by size exclusion chromatography (SEC) [89]. Different DNA sequences have different affinities with SWCNT depending on their chirality. Using a sequence-pattern expansion scheme, Zheng et al. have identified more than 20 DNA sequences that each select for a specific SWNT chirality [90]. Ion-exchange chromatography (IEX) has been used for the separation. As seen in Figure 1.8, the chiral purity is nearly perfect, as the optical absorbance spectra show low background and little additional structure beyond the known optical transitions for the assigned SWNT chirality.

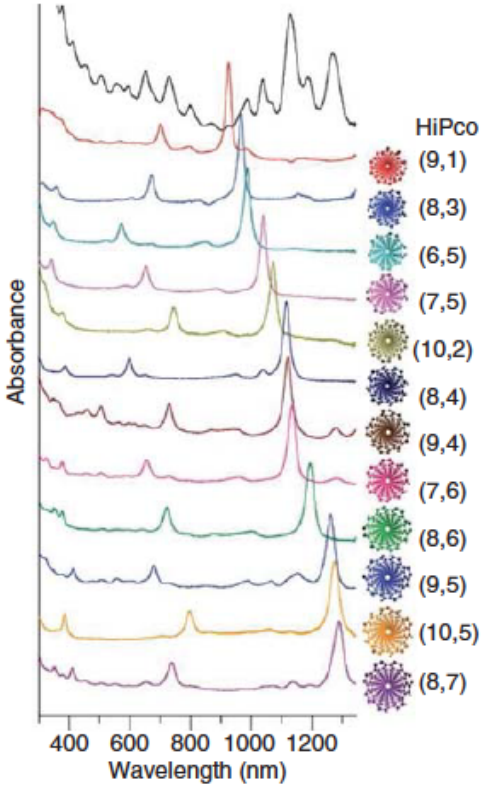

Figure 1.8: Optical absorbance spectra for as-synthesized HiPco single-walled carbon nanotubes (top) and 12 single chirality samples—with (n,m) values at far right—produced by ion exchange chromatography. In each single-chirality sample, a different DNA sequence was used for structure-specific recognition. (Figure adapted from Tu et. al. [89].)

As an alternative method, selective removal of metallic CNTs has been shown for tubes in a three terminal device configuration. While the gate electrode switches off the semiconducting tubes, a large current is flown through the metallic ones, producing their electrical breakdown [91]. This technique has been employed to eliminate individual shells from MWCNTs and to selectively remove metallic nanotubes in a SWCNT bundle [92]. Alternatively, chemical

methods have been developed to suppress the conductivity of metallic CNT [93]. While early approaches inevitably resulted in some damage of the surrounding semiconducting tubes, Jin et. al. have recently demonstrated a method to produce high density arrays of aligned semiconducting SWCNTs by a selective removal process [94]. No degradation of the s-SWCNTs was observed, and high mobility, current ratio and output current were reported.

1.3 Lithographically directed self-assembly

Self-assembly is a process in which separated components combine in an ordered fashion by mean of some kind of information that is encoded in the components themselves. In the case of directed self-assembly, the assembly is guided by some external factor – e.g. mechanical force, temperature, electric or magnetic fields, etc. Lithographic patterning has been used for decades in modulating surface morphology and chemistry. It also appears to be well-suited for controlling the assembly of nanostrucures on a surface.

Block copolymers are an excellent example to illustrate this concept. They can be thought of as macromoleculecules composed of chemically distinct homopolymers (blocks) linked end-to-end. Their self-assembly is driven by the separation of the chemically dissimilar polymer segments into different domains. Above a certain temperature, called order-disorder transition temperature (T_{ODT}) and which depends on the specifics of the system under consideration, the block copolymers are randomly mixed. Below T_{ODT} the

copolymer crystallizes into a specific morphology, based on the assembly conditions. By controlling the crystallization process different periodic arrangements can be obtained, with periodicities ranging between ~ 3-150 nm. Block copolymers are usually divided into bulk and thin film. The threshold between the two is usually somewhere between 2 μm and 200 nm [95]. While electric fields, magnetic fields, temperature gradients and directional solidification are effective tools to direct the assembly of bulk block copolymers, the best results – i.e. high resolution, large area, low defects assembly – have been obtained with thin film copolymers on lithographically pre-patterned substrates [96, 97]. In this case, relatively large patterned features serve as a guide for the copolymer to assemble into a much smaller pattern, without defects over arbitrarily large areas. Irregular patterns have been demonstrated with this approach as well.

In the same way as with block copolymers, 'top-down' lithographic patterning can be combined to 'bottom-up' self-assembly to organize molecules and nanostructures, in solution and on a surface, to yield functional devices that can be integrated with existing technologies. Examples include the assembly of nanoparticles [98, 99], quantum dots [100] and nanowires [101]. This approach has been also used for the nanoscale control over the organization of biomolecules. Biomolecules nanoarrays offer several advantages over their macroscale counterparts: unmatched sensitivity, smaller test sample volumes in molecular diagnostics, and high-throughput analysis through the ability to monitor (distinct) biorecognition events in parallel on the same chip [102-106].

As illustrated in section 1.1, DNA has shown to be a particularly useful and versatile biomolecule. Various approaches have been used to control the placement of DNA nanostructures on surfaces. Electron-beam lithography has been used to pattern hydrophilic regions in a hydrophobic matrix (on the substrate surface) to which DNA origami could physisorb [107]. The same process has been used to organize Au NPs on a substrate [108]. The NPs are attached to the corners of a triangular DNA origami that are selectively placed on a prepatterned surface. Other strategies rely on non-covalent interactions, such as ionic attractions on carboxyl-functionalized Au surfaces [109], or physisorption on nanopatterned, and chemically modified, graphene films [110]. Covalent strategies, such as thiol attachment on Au, have been employed to bridge gold islands (~60 nm in diameter) with DNA nanotubes (~320 nm in length) [111]. This facilitated a certain degree of orientational control of large DNA nanostructures on a patterned surface. In a recent work that scales to finer dimensions, DNA nanostructures have been chemisorbed through DNA base pairing on arrays of gold nanoparticles formed from diblock copolymers [112].

As explained in section 1.2, SWCNTs have excellent electronic properties, but synthesis methods produce mixtures of tubes with different properties. Solution based purification methods have been developed, but, to produce solid state devices, they necessarily need to be complemented with deposition techniques. The combination of lithographic patterning and self-assembly has demonstrated the ordered deposition SWCNT [113, 114]. Recently arrays of purified

semiconducting SWCNT with densities as high as 10 tubes/μm have been reported [115]. Even higher densities (100-500 tubes/μm) have been shown by organizing arrays of CNTs (bundles of ~ 2 – 10 CNTs) in solution by DNA scaffold-assisted assembly [116].

Solution-processed SWNT transistors generally show inferior performance than transistors made with CVD tubes. (Reported average effective mobility for s-SWNTs in the range of 20-200 $cm^2 V^{-1} s^{-1}$ [117], as compared to CVD tubes, whose effective mobility is typically above 1000 $cm^2 V^{-1} s^{-1}$ [118, 119].) This performance reduction is due to increased scattering in the channel, probably given by a higher number of defects originating from the suspension and/or purification processes [120]. The contact resistance though, is comparable to that of CVD devices. Therefore, solution-processed s-SWNTs are expected to provide performance similar to that of CVD-grown nanotubes in ultimately scaled FETs, where electron transport is largely limited by contacts rather than channel scattering.

This thesis is motivated by the need for an engineered approach to the creation of large numbers of single-molecule (or single-nanoobjects) devices that can be interrogated individually in an efficient manner. To this end, techniques are developed that use directed assembly to organize various molecules and nanostructures. These techniques are directly applicable to fundamental studies of electron transport in molecules and other nanostructures, but they

also have utility in other fields, such as chemistry and biology, where single molecule resolution is desired. In addition, the approaches developed in this work may facilitate the advancement of new electronics technologies, including, but not limited to, future circuits based on single-wall carbon nanotubes with specific electronic properties.

Chapters 2 and 3 detail two approaches to direct the assembly of nanostructures on a surface. The first one (chapter 2) involves the patterning and selective functionalization of metallic nanodots that are used as anchors for the attachment of DNA molecules, proteins (streptavidins), DNA nanostructures (a double crossover 1D motif and DNA origami) and DNA-wrapped SWCNT segments. Different strategies are explored to maximize the yield of the desired assembly. This platform also allows the monitoring of DNA-protein interactions with single molecule resolution. The second approach is described in chapter 3; here lithographic patterning is used to create high surface energy regions that promote the binding of DNA origami and SWCNT segments. The high patterning resolution again allows for single nanostructure manipulations. This method yields to the assembly of SWCNT FETs from DNA-wrapped SWCNT segments. Chapter 4 concerns the formation of multi-component nano-objects in solution by directing the linkage of properly functionalized nanostructures. The products of these reactions are suitable for surface placement with the techniques of chapters 2 and 3, thereby resulting in a hierarchical directed assembly process. One of the methods described in chapter 4 produces SWCNT-dsDNA heterostructures that can be used to electrically probe dsDNA using the

SWCNTs as electrodes, by assembling solid state devices by mean of the techniques developed in chapters 2 and 3.

Chapter 2

Self-assembly on biomolecular nano-anchors

2.1 Introduction

The techniques described in this chapter are inspired by polyvalent interactions, a phenomenon widely observed in biology. Polyvalent interactions are characterized by the simultaneous binding of multiple ligands on one biological entity (a molecule, a surface) to multiple receptors on another. Polyvalent interactions can be collectively much stronger than corresponding monovalent interactions, and they can provide the basis for mechanisms that are fundamentally different from those observed in monovalent systems [121, 122].

Following this principle we have developed methods to assemble nanostructures functionalized with multiple binding sites, precisely arranged in a way that matches the dimensionality and shape of the nanostructure, onto surfaces pre-patterned with matching attachment points. The concept is illustrated in Fig. 2.1 in which one dimensional (1D) nanostructures are functionalized with two binding sites, one at each end, two dimensional (2D) nanostructures with

triangular shape are functionalized with three binding sites, one at each corner, 2D nanostructures with rectangular shape have four binding sites, one at each corner, etc.

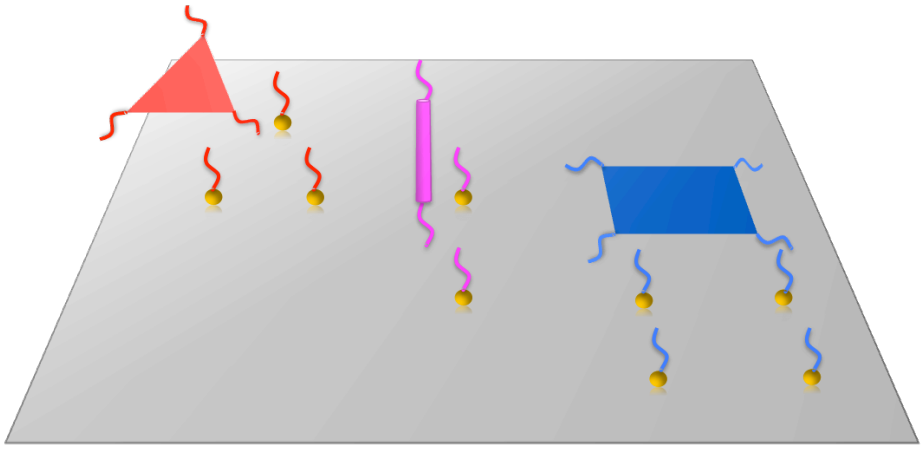

Figure 2.1: Schematic of the directed-assembly technique involving surface bound nanodot-anchors and nanostructures with matching binding sites.

The surfaces upon which the nanostructures assemble are patterned with arrays of metallic nano-dots made by nanoimprint lithography. Nanoimprint lithography facilitates the inexpensive and high throughput production of high-resolution nano-patterns. Our nanodots can be made with a diameter as small as ~ 2 - 3 nm and they can be arranged as close as 15 - 20 nm with positional error in the nanometer regime. In practice we can exactly match the arrangement of the binding sites of all the nanostructures of interest for our assembly.

A key element of the process is the selective functionalization of the metallic nanodots with (bio)molecular species that are complementary to the ones

present at the binding sites of the nanostructures. When the nanostructures are incubated on the functionalized substrates, molecular interactions drive the selective attachment of the nanostructures on the patterned nanodots. The polyvalent nature of the interactions confers the desired positional and orientational precision. This technique has been implemented with various 1D and 2D nanostructures:

- 1D nanostructures:
    - A rigid 1D nanostructure made of double crossover DNA (DFX)
    - DNA-wrapped SWCNT segments
- 2D nanostructures:
    - DNA origami

2.2 Nanodot array fabrication

The arrays of nanodots are made by thermal nanoimprint lithography (NIL) followed by a self-aligned pattern transfer process [123]. In the nanoimprint step a mold with the desired features in relief is brought into contact with a substrate coated with a thin film of thermoplastic polymer (imprint resist). A high pressure is applied and the temperature is raised above the glass transition point (T_g) of the polymer [124]. Mold and substrate are then cooled and separated, resulting in the polymer being a negative replica of the mold pattern (Fig. 2.2). The pattern is then transferred through metallization and lift-off (Fig. 2.4, below).

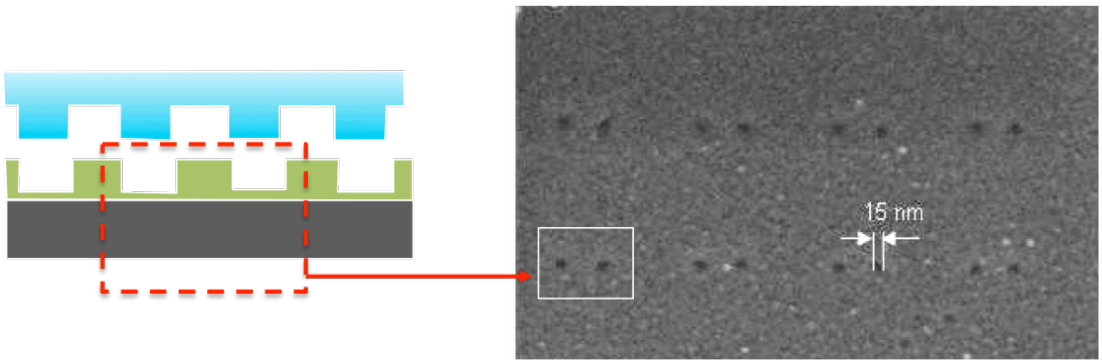

Figure 2.2: (Left) Schematic of the imprint process. (Right) SEM image of imprinted PMMA.

The choice of nanoimprint lithography has several advantages over direct-write electron-beam (e-beam) lithography. While the mold does need to be fabricated with a serial patterning technique such as e-beam lithography – at least for the feature size required in this work – it can then be replicated in parallel by nanoimprint. The process is thus faster and cheaper than e-beam lithography but it achieves the same fine resolution [125]. The nanoimprint process is also robust, i.e. it has a good tolerance to fluctuation of its parameters (mainly imprint temperature and pressure) and the necessary equipment is relatively simple and inexpensive.

2.2.1 NIL mold fabrication

On order for a thermal nanoimprint process to succeed, i.e. reliably produce the desired features on each imprinted sample, the nanoimprint molds need to

comply with a few requirements:

(a) Molds need to be hard and durable since they have to sustain repeated imprint cycles in which high temperature and pressure are applied, followed by mechanical stress during the mold/substrate separation. The features on the molds are often in the nanometer scale with high aspect ratios and are thus intrinsically fragile.

(b) Molds need to posses a low thermal expansion coefficient to prevent features distortion or stress accumulation when the temperature is increased to the polymer glass transition point.

(c) Molds need to have a low surface energy to facilitate separation between mold and imprinted sample. This is usually achieved by applying a hydrophobic coating to the mold surface.

In this work the nanoimprint molds were made by e-beam lithography using hydrogen silsesquioxane (HSQ) as both the resist and the mold material. E-beam lithography is a versatile patterning technique in which an electron beam is scanned according to a programmed pattern onto a resist, typically a polymer film that is spin-coated on a substrate. Resists can have a positive or a negative tone. The polymer chains in a positive resist undergo chain scission when exposed to the electron beam, and the exposed polymer is washed away in the subsequent development step. In contrast, the polymer chains of a negative resist are crosslinked by the electron beam and remain on the substrate after development. HSQ is a negative tone e-beam resist that yields high-resolution

features (~10 nm). Its monomer is $H_8Si_8O_{12}$; when irradiated with electrons Si-H bonds are broken and Si-O bonds between adjacent monomers can be formed[126].

HSQ (Dow Corning ® XR-1541 e-beam resist dissolved in MIBK at a concentration of ~ 2% by weight) is spin-cast onto silicon wafers with a thickness of about 25 nm. No post-apply bake is used in order to minimize thermal cross-linking of the HSQ. E-beam patterning is done using a scanning electron microscope (FEI XL-30 Sirion) equipped with a Nabity NPGS pattern generator or with a Nanobeam nB4 electron beam lithography system. Circular shapes with diameters ranging from 10 to 20 nm are written (Fig. 2.3). The HSQ is developed for 6 min in Microposit MF CD-26W developer at room temperature, followed by a deionized (DI) water and isopropyl alcohol rinse. The molds are then exposed to an oxygen plasma for 1 min (Diener Plasma Etch System) annealed in air, on a hot plate at 540 °C for 2 h. These steps are necessary to convert the HSQ from a porous network to a smooth, glassy silicon oxide. Finally the molds surface is coated with a fluorosilane anti-adhesion layer deposited in a vapor phase coater (NanonexUltra-100). The molds are exposed to an oxygen plasma for 1 min (Diener Plasma Etch System) prior the molecular vapor deposition step. This is done in vacuum, at 80°C for 15 minutes.

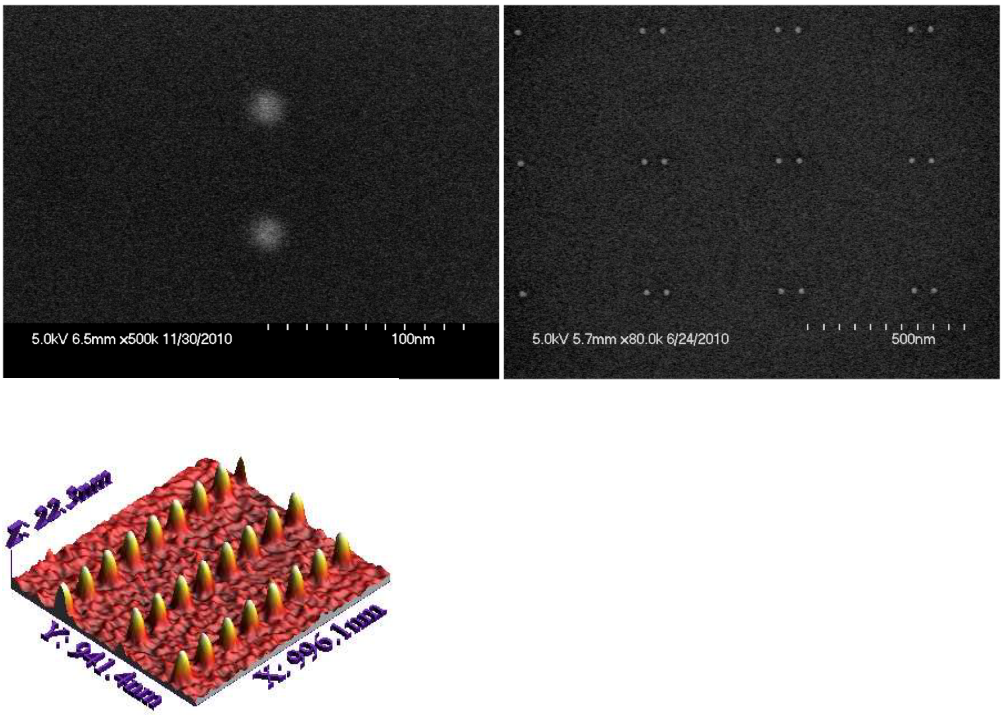

Figure 2.3: (Top) SEM images and (Bottom) 3D AFM image of an e-beam written HSQ mold

2.2.2 Nanoimprint process

Thermal NIL is executed at a temperature of 180 °C, a pressure of 500 psi, and imprint time of 5 min, using a Nanonex BX200 imprinter. The imprint resist is poly(methylmethacrylate) (PMMA, M_w = 35 K Microresist) spin-cast to give a thickness of ~50 nm. The imprint substrates are highly doped silicon with 300 nm of thermally grown silicon oxide for SEM and AFM studies; they are glass coverslips of thickness 150 μm (Corning #1.5) or fused silica slides for the experiments involving fluorescence microscopy. Prior PMMA spinning, Si wafers

are cleaned with acetone and isopropyl alcohol, prebaked at 185 °C for 5 minutes and exposed to a one minute oxygen plasma (Diener Plasma Etch System). Glass coverslips or fused silica slides are cleaned in a boiling solution of 7X detergent (MDBio) diluted 1:4 in DI water for 2 minutes, then rinsed in DI water, blown dry with nitrogen and exposed to a 1 minute oxygen plasma (Diener Plasma Etch System).

2.2.3 Pattern transfer process

After thermal NIL each sample features a negative replica of the mold pattern. The imprinted resist is then typically used as a mask for etching or for metallization and lift-off, which is the option adopted in this work.

As shown in Fig. 2.4, the NIL process leaves a thin residual layer of resist at the bottom of the imprinted features. In order to transfer the pattern by lift-off, this layer must be removed, usually with a plasma etch. This descum step needs to be highly controlled since it might result into lateral broadening of the features due to less than perfect etch anisotropy. The additional fact that it is theoretically impossible to obtain negatively sloped side walls of imprinted features, makes pattern transfer by metallization and lift-off very challenging, especially for features in the sub-100 nm regime. Since our features are 20 nm or smaller, we used a process that employs an angle-evaporated metal hard mask is formed on the imprinted resist [123].

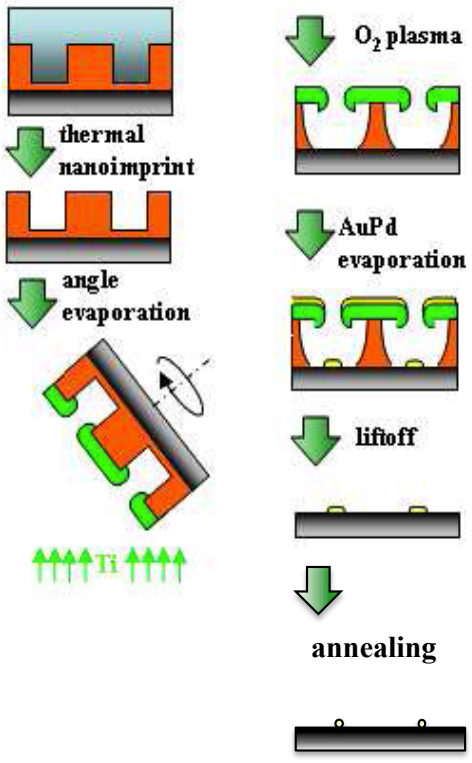

Figure 2.4: Schematic of nanoimprint and pattern transfer processes.

This is obtained by depositing ~10-12 nm of Ti by electron beam evaporation (Semicore SC2000, 0.02 nm/s) tilting the samples at a 30° to 45° angle. The PMMA residual layer was then removed with an O_2 reactive ion etching (150 s, Diener Plasma Etch System). The presence of the hard mask considerably reduces the sensitivity to the descum etch conditions, and enables clean removal of the residual layer without erosion of the imprint resist layer – even if the etch process is not perfectly anisotropic [123]. A ~0.8-1 nm Ti adhesion layer and ~2.5–3 nm of AuPd (60:40) were deposited by electron beam evaporation (Semicore SC2000, 0.01 nm/s). Fig. 2.5 shows the structure after

AuPd deposition but before lift-off. Visible are the imprinted PMMA beneath the Ti mask; the AuPd features can be seen on the substrate.

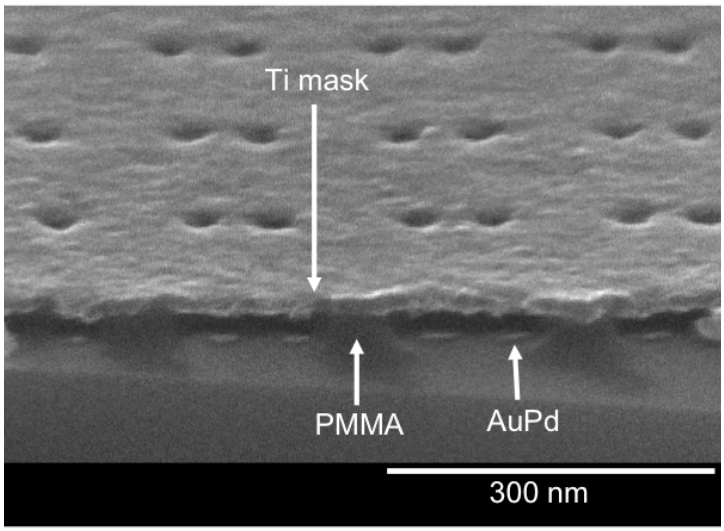

Figure 2.5: Cross-section SEM image showing imprinted PMMA, Ti mask and AuPd features before lift-off and annealing.

Lift off in boiling acetone (15 min) and overnight soaking in acetone is followed by annealing at 450 °C for 24 h, resulting in approximately spherical nanodots [123], ~5–10 nm in diameter, depending on the parameters chosen for the process (diameter of the HSQ mold features, thickness of the Ti mask, tilt angle, thickness of the evaporated AuPd). Nanodot arrays are characterized with scanning electron microscopy (SEM, Hitachi 4700) and atomic force microscopy (AFM, XE-100 Advanced Scanning Probe Microscope PSIA, non-contact mode imaging, Mikromasch NSC16 tips made of n-type silicon phosphorus doped with spring constant 40 N/m; AFM images are analyzed with XEI software, version 1.7.6). Figure 2.6 shows an example of the nanodots arrays.

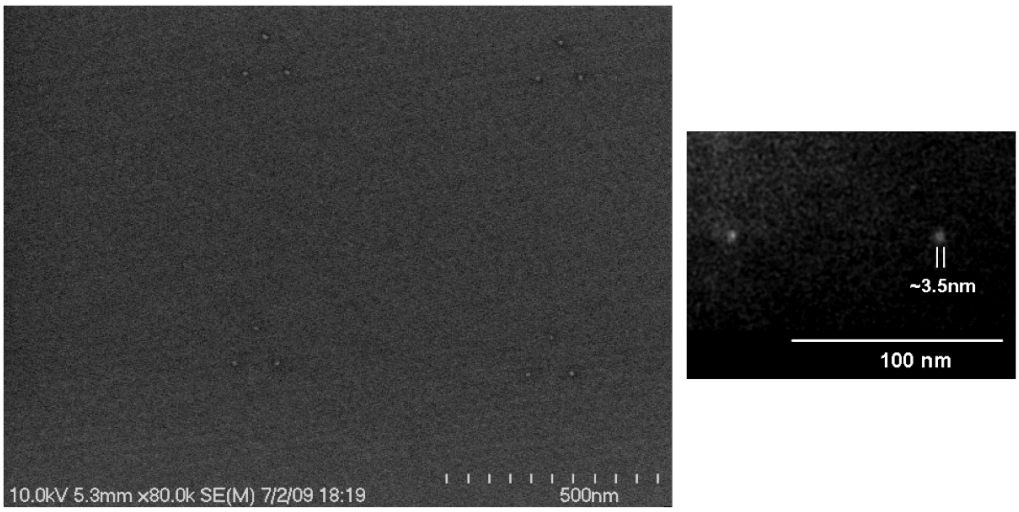

Figure 2.6: SEM images of AuPd nanodot arrays after lift-off and annealing. (Left) Array of nanodots arranged in trimers. The spacing between the dots within each trimer is 120 nm; trimers are 600 nm apart. (Righ) Example of nanodots with ~ 3.5 nm diameter.

2.3 Biofunctionalization of nanodot arrays

Different functionalization schemes have been developed to selectively bind molecules (or biomolecules) to the patterned nanodots. Every approach is based on a thiol group binding to the AuPd nanodots [127]. The simplest scheme (attachment of amine groups or ssDNA to the dots) does not involve any passivation of the SiO_2 surface because of the weak adhesion of DNA to SiO_2. A protein repellent film of polyethylene glycol (PEG) passivation layer is required when proteins (streptavidin) are involved in order to prevent nonspecific binding [128]. These two functionalization schemes are illustrated in Fig. 2.7.

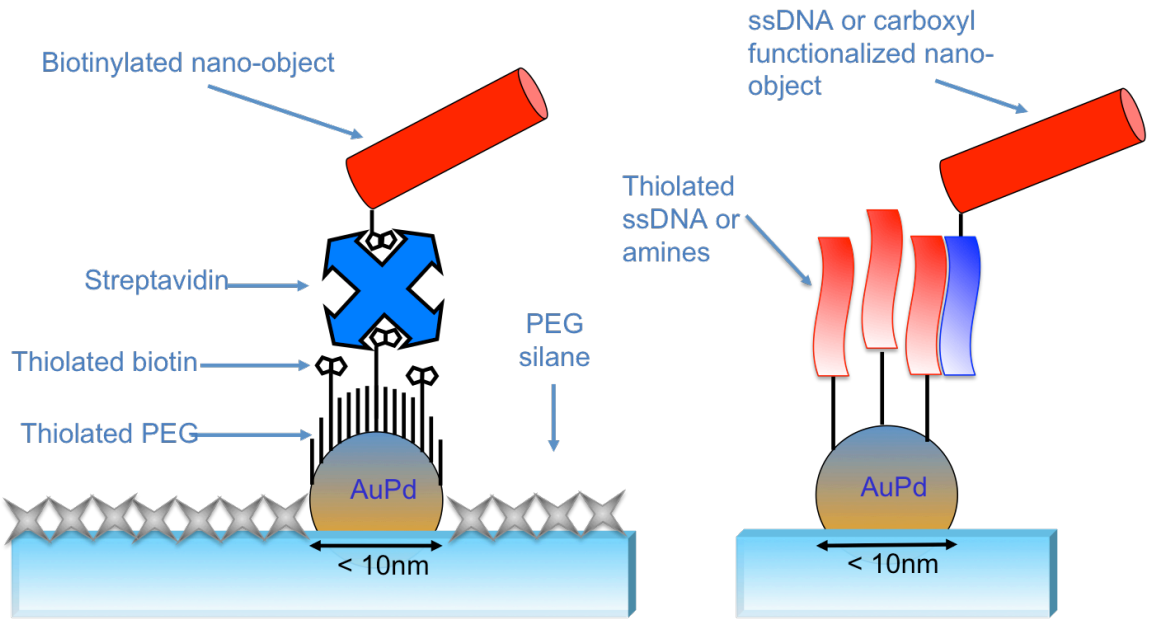

Figure 2.7: (Left) Schematic of nanodots functionalization through biotin-streptavidin. (Right) Schematic of nanodots functionalization through direct thiolation.

2.3.2 Functionalization through direct thiolation

In this functionalization method molecules are directly attached to the AuPd nanodots through a thiol linkage [129-131] (Fig. 2.7-right).

Patterned substrates are first cleaned in an aged (1.5 h old) piranha solution (3:1 H_2SO_4 : H_2O_2) followed by a de-ionized (DI) water rinse, an ethanol rinse and they are then blown dry with an inert gas (Ar or N_2). The dry samples are put in an UV–ozone cleaner (Harrick PDC-32G) for 5 min at 18 W, then immediately incubated in a freshly prepared thiol-DNA or thiol-amine solution: 1 μM HS-ssDNA (a 3' thiol modifier was used: /3ThioMC3-D/) purchased from

Integrated DNA Technologies (IDT), in 1.5 ml phosphate buffer (Gibco™ Dulbecco's phosphate buffer saline –DPBS– 1X, no magnesium, no calcium, 2.7 mM potassium chloride, 0.14 M sodium chloride, 1.5 mM potassium phosphate, and 8 mM sodium phosphate, pH 7.4, Invitrogen) or in 2 ml of 10 μM 11-Amino-1-undecanethiol hydrochloride (Sigma Aldrich) in DI water. Samples are immersed in the thiol solution for 18 h (overnight) on a shaker to allow the formation of a self-assembled monolayer (SAM) of ssDNA or amine groups on the metal dots. Following the reaction, the substrates are rinsed in a stream of DPBS buffer or DI water to remove non-specifically bound thiolated molecules. Kimwipes are used to wick off excess liquid from the edge.

2.3.2 Functionalization with biotin-streptavidin

In this second approach, a mixed SAM of thiolated alkanes and thiolated alkanes presenting a biotin group is formed on the metal nanodots. The biotin end groups can be used for the subsequent immobilization of streptavidin that acts as a binding bridge for biotin-functionalized nanoobjects [132, 133] (Fig. 2.7 left).

Patterned substrates are first cleaned in an aged (1.5 h old) piranha solution (3:1 H_2SO_4 : H_2O_2) followed by a de-ionized (DI) water rinse, an ethanol rinse and they are then blown dry with an inert gas (Ar or N_2). The dry samples are put in an UV–ozone cleaner for 5 min at 18 W, then immediately immersed in 1.5 ml of an anhydrous ethanol 1 mM mixed solution of HS–$(CH_2)_{11}$–$(C_2H_6O_2)_3$–

OH and HS–$(CH_2)_{11}$–$(C_2H_6O_2)_3$–biotin (Prochimia) at a 3:1 ratio. The substrates are incubated in this solution for 18 h (overnight) on a shaker to allow the formation of a SAM presenting biotin groups on the metal dots. Samples are then rinsed in ethanol, blown dry in Ar and immersed in a 13.3 μM solution of polyethylene glycol (PEG)-silane (average M_w = 5000, LaysanBio) in anhydrous toluene. Acetic acid (30 μl for 30ml of toluene-PEG solution) is added as a catalyst to the solution directly prior to immersing the samples. Samples are incubated for 24 to 48 hours to allow a uniform PEG layer to form on the SiO_2 so that it will then successfully prevent nonspecific binding of the subsequently added proteins. Samples are then rinsed with acetone and ethanol, blown dry with Ar and finally rinsed with DPBS prior to immersion in a 130 nM solution of streptavidin, which is labeled with the fluorophore AlexaFluor488 (Invitrogen), in a 15 mM solution of chicken egg white albumin (Sigma Aldrich) in DPBS. The purpose of albumin is to block nonspecific binding between streptavidin and any passivation defects in the PEG layer. They are incubated for 2 hours, then rinsed with DPBS and incubated with a 2 μM solution of biotin functionalized ssDNA or dsDNA in DPBS for 3 hours. The samples are finally rinsed in DPBS.

Different DNA strands are attached to the streptavidin depending on the purpose of the experiment. The ssDNA strands, of different length and sequence, are functionalized with a biotin group on the 5' end. dsDNA is hybridized prior attachment to the streptavidin. Two 2 μM solutions of complementary ssDNA strands in TPBS (ThermoScientific BupH™ PBS, 0.1 M sodium phosphate and 0.15 M sodium chloride, pH 7.2) are mixed at room

temperature and heated to 65 °C at a rate of 2 °C/minute. The solution is maintained at 65 °C for 15 minutes then brought at 75 °C and maintained at that temperature for 1 hour and 30 minutes. The solution is cooled down following the same process in reverse order. Typically one of the two complementary strands is functionalized with a biotin group on the 5' end, the other strand is functionalized with a fluorophore on the 5' end. In this way, after hybridization the flourophore is located at the end of the DNA opposite to the biotin group.

2.3.3 Fluorescence microscopy

Fluorescence microscopy is utilized to measure the specificity of the nanodot fuctionalization, to detect nonspecific binding and to monitor molecular interactions on the functionalized nanodots.

Epifluorescence microscopy is performed on an Olympus IX81 inverted microscope equipped with a 60x and 100x oil-objectives (Olympus) and a 512 x 512 pixel Cascade II CCD Camera (Photometrics, Inc.). Streptavidin is purchased labeled with Alexa-488 or Cy-5 (Invitrogen). DNA is labeled with Cy-3 or RhodRed (IDT). Glass coverslips of thickness 150 μm (Corning #1.5) or fused silica slides are patterned with nanodots (or clusters of nanodots) spaced 2 μm apart. This allows individual nanodots (or nanodot clusters) to be optically resolvable.

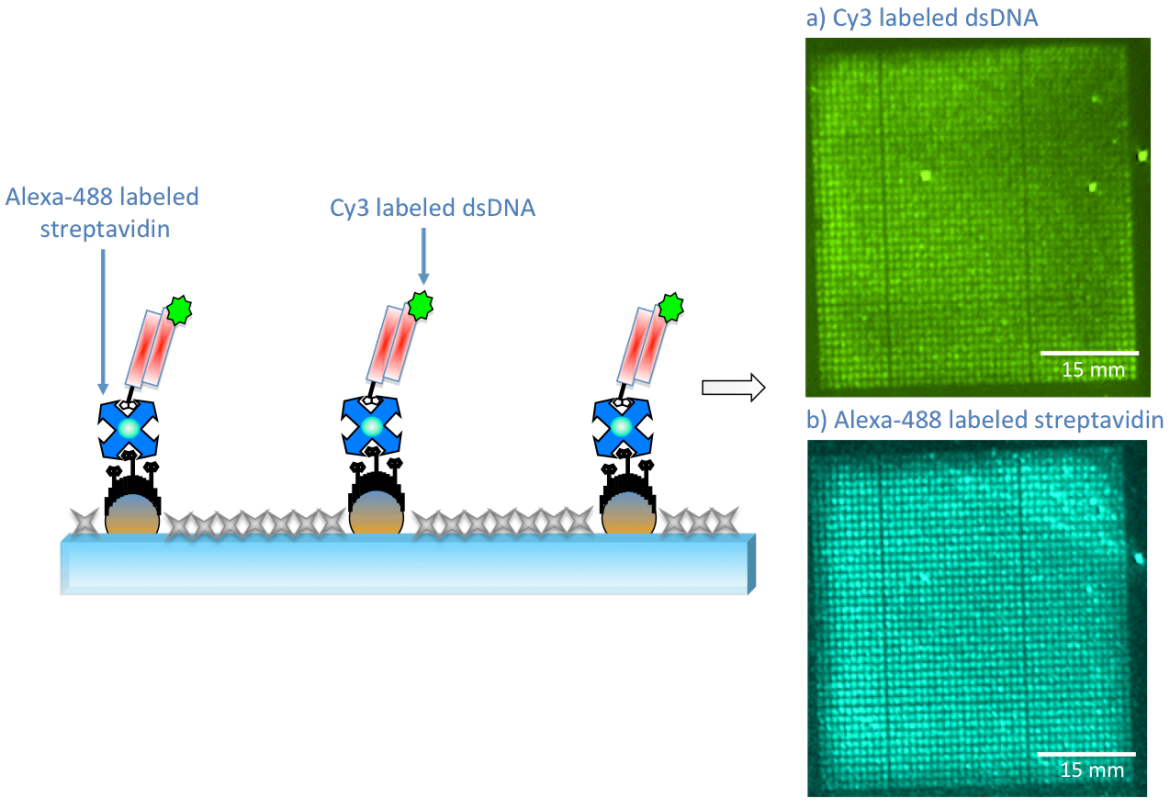

Figure 2.8: Fluorescently labeled streptavidin and dsDNA attached to the nanodots. a) Fluorescence microscopy image of dsDNA labeled with Cy3. b) Fluorescence microscopy image of streptavidin labeled with Alexa-488. The two images are taken from the same substrate imaged through different channels. The fluorescent signal comes from the same pattern, which corresponds to the position of the AuPd nanodots.

Fig. 2.8-b shows the immobilization of fluorescently labeled streptavidin on the nanodot sites, while Fig. 2.8-a shows the subsequent immobilization of fluorescently labeled dsDNA. Each DNA molecule is labeled with one fluorophore on the distal end of the duplex (i.e., on the end not attached to the surface-bound streptavidin). The fluorescence background is measured in the uniformly passivated regions between the nanodots. The amount of nonspecific

adsorption is determined by measuring the average background fluorescence intensity of the glass surface before and after exposure of the substrate to fluorescently labeled DNA and it is found to be 0.1 - 0.5 μm^{-2} (i.e., less than one DNA molecule every 2 μm^2).

Comparable results are found attaching fluorescently labeled dsDNA to the nanodots through direct thiolation (Fig. 2.9).

2.4 Biomolecular interactions on nanodot arrays

2.4.1 Hybridization in situ

ssDNA immobilized to the patterned nanodots is hybridized in situ with the complementary strand functionalized with a fluorophore on the far end of the strand (i.e., the one not attached to the nanodots), enabling fluorescence microscopy imaging.

Nanodots functionalized through direct thiolation are incubated with a 1 μM solution of complementary ssDNA in 1X tris-acetate-EDTA (TAE) buffer with 125 mM $MgCl_2$ for at least 3 hours, and up to about 18 hours, at RT. Nanodots functionalized through biotin-streptavidin are incubated with a 2 μM solution of complementary ssDNA in TPBS with 3 mM NaCl and 125 mM $MgCl_2$ for a similar time at RT. It is worth noting that the experiments are carried out in different buffers not out of necessity, since both buffer solutions can work for this experiment. The important parameter is the relatively high salt

concentration, which is necessary to screen any repulsive interactions taking place between the phosphate groups of the complementary DNA strands, as they can prevent effective hybridization from taking place at RT. The incubation is done by depositing about 10/20 μl of solution on top of the pattern area, in a sealed container with a moist atmosphere in order to prevent evaporation. After incubation, the samples are rinsed in DPBS and imaged by fluorescence microscopy (Fig. 2.9).

Hybridization in situ is performed with different DNA sequences (strands are purchased from IDT).

- Biotin-streptavidin: one 20-mer with a biotin functional group at the 5' position (5'-/52-Bio/GTC ACT TCA GCT GAG ACG CA-3') on the dots; hybridized with the complementary strand with a Cy3 fluorophore at the 5'-end (5'-/5Cy3/TGC GTC TCA GCT GAA GTG AC-3').
- Direct thiolation: one 20-mer with a thiol functional group at the 5' position (5'-/thiol/AAA AAA AAA AAA AAA AAA AA-3') on the dots; hybridization is done with complementary strands of different length (ranging from 8 thymines to 30 thymines) with a Cy3 fluorophore at the 5'-end (example: 5'-/5Cy3/TTT TTT TTT TTT TTT TTT TT-3').

In both functionalization approaches, hybridization between non-complementary strands does not yield any fluorescence signal.

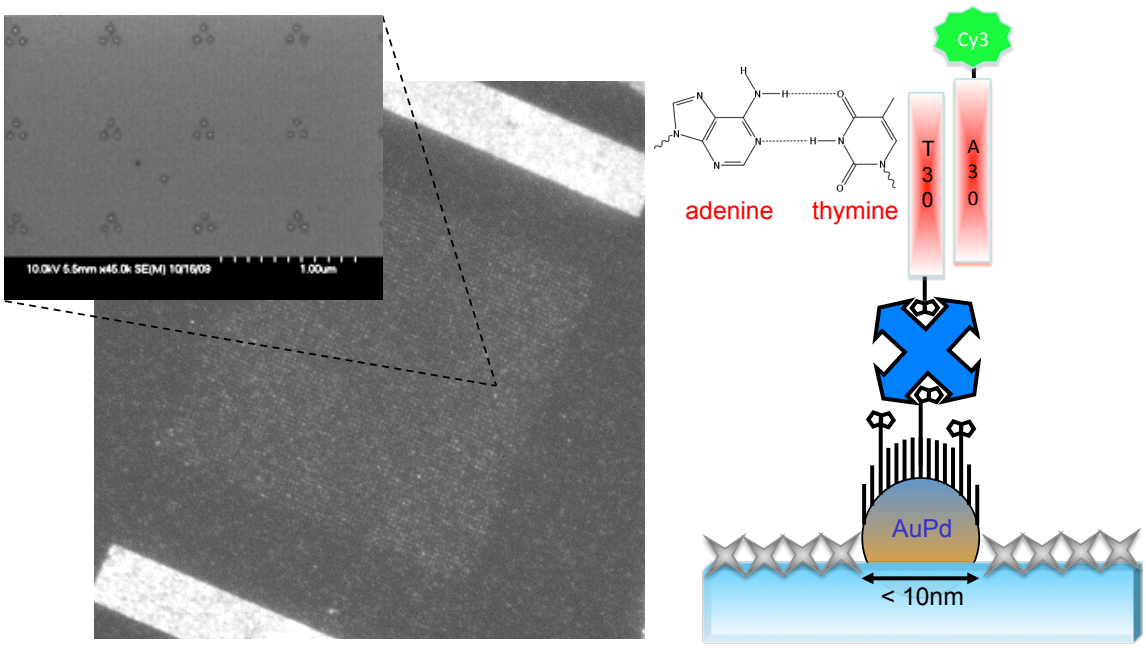

Figure 2.9: (Left) Fluorescence image of Cy3 labeled ssDNA hybridized to the complementary ssDNA immobilized on nanodots. The inset shows an SEM image of the nanodots, which, in this case, are patterned in trimers. (Right) Schematic of the experiment.

2.4.2 dsDNA cleavage by a restriction enzyme

The suitability of the functionalized nanodot platform for real-time monitoring of biomolecular interactions is demonstrated by performing the cleavage of dsDNA anchored to the nanodots by a restriction enzyme [134]. In this experiment, the nanodots are functionalized with a 20 base pair (bp) dsDNA labeled with RhodRed fluorophore on the distal end of the duplex, which is attached to the nanodot via the biotin-avidin linkage, as described in section 2.3.2.. The DNA duplex is made of one 20-mer with a biotin functional group at the 5' position (5'-/52-Bio/GTC ACT TCA GCT GAG ACG CA - 3') and the

complementary strand with a RhodamineRed fluorophore at the 5'-end (5'-/5RhoR-XN/TGC GTC TCA GCT GAA GTG AC - 3').

The arrays of functionalized nanodots are incubated with a 7.7 nM solution of PvuII-HF (New England Biolabs) in NEB buffer (New England Biolabs, 10 mM magnesium acetate). The experiment is conducted at 37°C. PvuII-HF is a well-known and commercially available restriction enzyme that cleaves DNA at the 5'-CAGCTG-3' recognition site [135]. A complete loss of fluorescence intensity, localized at the individual nanodots, is observed within seconds of addition of the enzyme (Fig. 2.10). This is presumably due to DNA cleavage by the enzyme and consequent loss of the fluorescently labeled segment of the anchored DNA (scheme in Fig. 2.10). In order to prove that this is the case, the same experiment is performed using a strand that lacked the 5'-CAGCTG-3' PvuII-HF recognition site (it contains the sequence –TCATAT- instead). Notably, no loss of localized fluorescence intensity at the nanodots is observed in this case – even after 30 minutes, indicating that the PvuII enzyme did not cleave the DNA (Fig. 2.11).

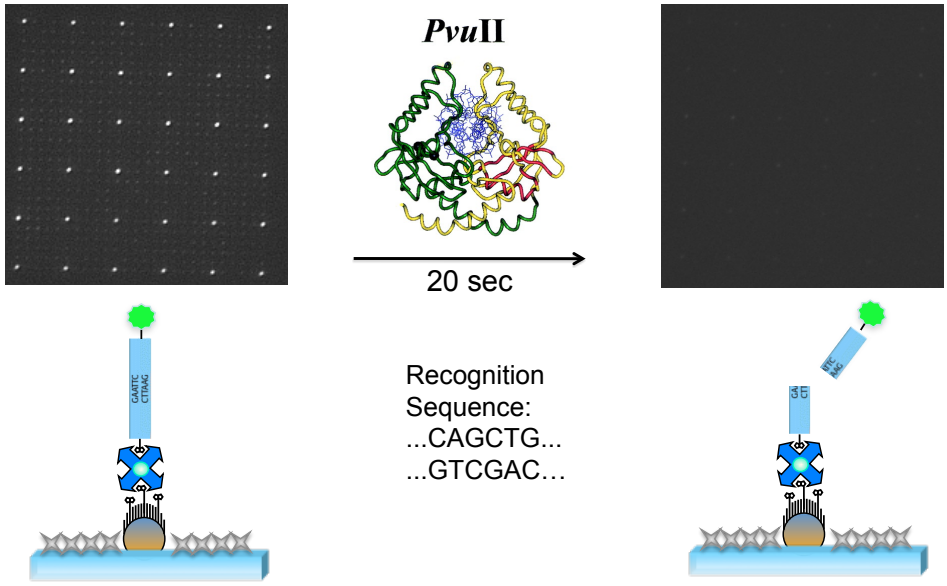

Figure 2.10: Fluorescence signal from nanodots functionalized with dsDNA tagged with RhodRed before and after incubation with the restriction enzyme PvuII, in the case when the dsDNA contains the sequence recognized by the PvuII.

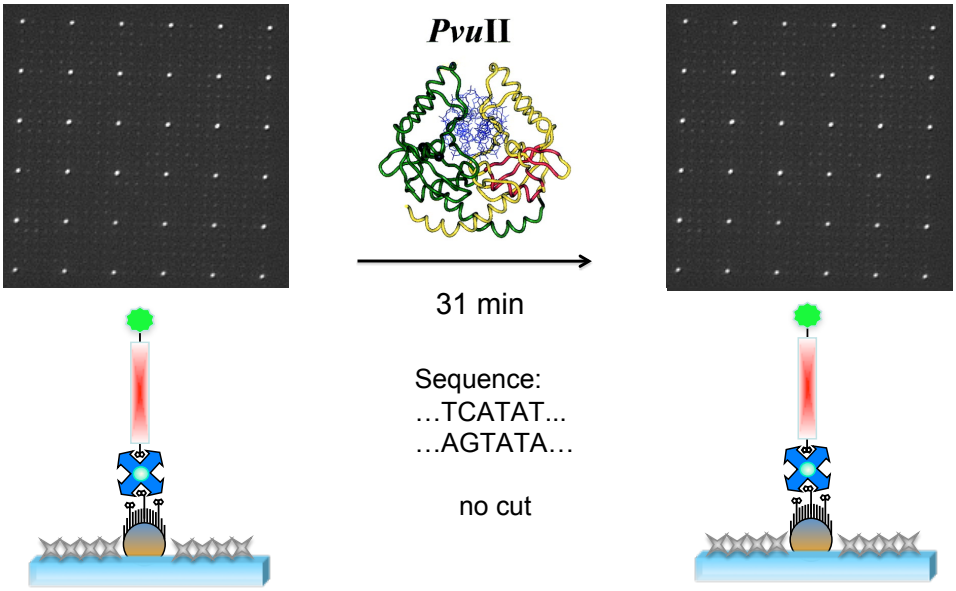

Figure 2.11: Fluorescence signal from nanodots functionalized with dsDNA tagged with RhodRed before and after incubation with the restriction enzyme PvuII, in the case when the dsDNA does not contain the sequence recognized by the PvuII.

The minimized crowding of the immobilized DNA that arises from the nanoscopic size and microscopic spacing of the nanodots, combined with the high selectivity and consequently high signal-to-noise ratio achieved, enables single-molecule resolution in monitoring the DNA-PvuII interaction. Each nanodot in the array is optically resolvable from its neighbors because of the 2 μm spacing, so it is possible to monitor the loss of fluorescence due to the restriction enzyme cleavage at the single-molecule level. This is manifested by a decrease in the fluorescence intensity in discrete steps, as shown in Fig. 2.12. A histogram of single-molecule fluorescence extinction as a function of time is built by extracting the time delay between when initial delivery of PvuII to the nanoarray and the point in time when each drop in fluorescence intensity is observed (Fig. 2.12 left). The histogram is well described by a difference of two exponentials (as shown in Fig. 2.12 right); this implies the existence of at least two rate-determining steps in the PvuII-DNA cleavage reaction, consistent with the existence of a Michaelis-Menten complex [136]. In addition, the extrapolated value of the overall catalytic rate constant (i.e., the " turnover rate constant", k) for PvuII ($k = 1\ s^{-1}$) is comparable to previously reported values obtained from ensemble measurements under the same buffer conditions ($k = 0.3\ s^{-1}$) [137-139].

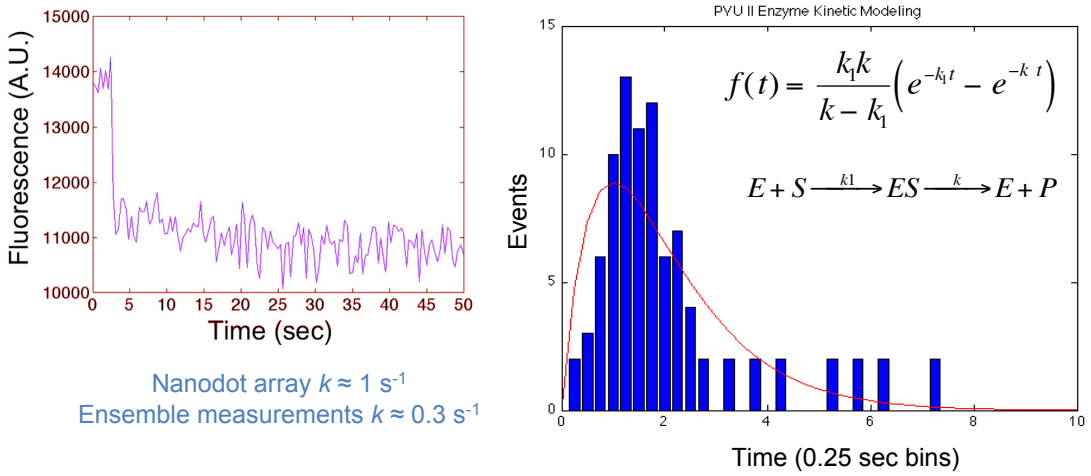

Figure 2.12: (Left) Fluorescent signal from one single nanodot showing the step produced by an enzyme cutting event. (Right) Histogram showing the distribution of the cutting time. The histogram is fitted with a difference of exponentials, implying the existence of two rate determining steps. The extrapolated value of the overall catalytic constant k is comparable to values found in ensemble measurements [137-139].

In order to demonstrate the selectivity of this process, two different 20 bp DNA molecules, one endonuclease-active and the other not, are co-assembled on a substrate. The PvuII-active DNA is labeled with a RhodRed fluorophore, while the inactive DNA (i.e., lacking the PvuII recognition site) is labeled with a Cy3 dye molecule; in each case, the fluorophore is localized at the distal end of the duplex. The presence of the two different DNA sequences on the same nanoarray is verified by multichannel epifluorescence microscopy, as shown in Fig. 2.13: the RhodRed-labeled DNA is imaged in the green channel and the Cy3-labeled DNA in the red channel. The functionalized nanoarray is then incubated with PvuII. Within seconds of the addition of the enzyme, a loss of fluorescence is observed for the PvuII-activeDNA (green channel), as shown in

Fig. 2.13, attributable to DNA cleavage by the enzyme and consequent loss of the fluorescently labeled segment of the anchored DNA. No loss of fluorescence intensity is observed on the same nanoarray for the DNA lacking the PvuII recognition site and labeled with the Cy3 fluorophore (red channel in Fig. 2.13), consistent with a lack of DNA cleavage by the enzyme.

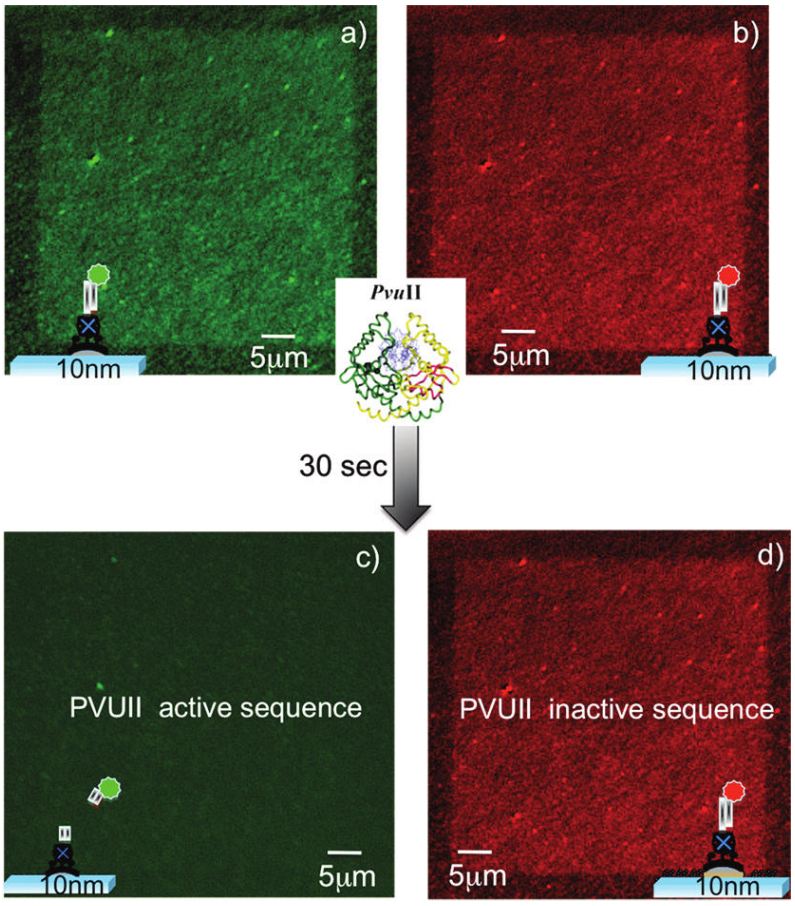

Figure 2.13: Epifluorescence microscopy images (100 ms exposure time) of a nanodots array functionalized with RhodRed-labeled dsDNA exhibiting the PvuII recognition site (green channel) and Cy3-labeled dsDNA lacking the PvuII recognition site (red channel). (a, b) Images taken before the addition of the enzyme. (c, d) Images showing that within seconds of the addition of the enzyme, the PvuII-active DNA is cleaved, as evidenced by the loss of fluorescence (green channel), while the PvuII-inactive DNA is not affected by the presence of the enzyme (red channel).

2.5 Assembly of 1D DNA nanostructures: DFX DNA

2.5.1 The DFX nanostructure

As explained in section 1.1.3, the crossover motif (DX) is a DNA nanostructure in which two different DNA duplexes are bound together by "crossing over" strands from one duplex to another [13]. The result is a rigid, one-dimensional nanostructure with a persistence length that exceeds that of a linear DNA duplex[140]. The DFX nanostructure is an example of such a crossover motif. It is comprised of two anti-parallel duplexes connected by five crossover points [141]. Double crossover DNA is a stiff DNA structure, having a persistence length about twice that of a linear DNA duplex. The DFX nanostructure is designed to be a rigid ribbon ~60 nm long and ~4 nm wide. Both ends of the DFX molecule are functionalized with a single sticky-end linker comprising 20 adenines, and a Cy-3 fluorophore is embedded in the middle of the nanostructure (Fig. 2.14).

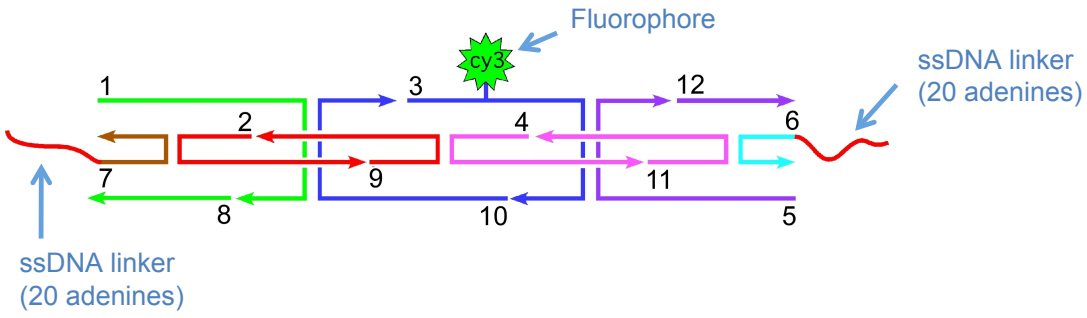

Figure 2.14: Schematic drawing of the DNA DFX nanostructure. The DFX contains two DNA duplexes joined together by five crossover points. It has twelve different oligonucleotides, different color-coded arrows indicate simplified strands running from 5′ to 3′. Single sticky-ends comprising 20 adenines are

added on both ends (red color). A fluorescent dye (Cy3) is attached to the middle of the nanostructure.

The DNA sequences are designed by applying the principles of sequence symmetry minimization, using the program SEQUIN [142]. All DNA strands are purchased from IDT with high-performance liquid chromatography (HPLC) purification. The DFX is formed by mixing a stoichiometric quantity of each strand, as estimated by OD260, in TAE buffer (40 mM Tris, 20 mM acetic acid, 2 mM ethylene-diamine-tetra-acetic acid -EDTA-) with 12.5 mM magnesium acetate, then it is annealed from 90 °C to room temperature in a 2 l water bath stored in a styrofoam box over the course of 40 h.

The sequence of the DNA DFX nanostructure (the sequence number is corresponding to the labeling in Fig. 2.14):

DFX1: 5'-CATTCCTCGGTTCTAGTGCTGTTGATAGCAGTGACGTTCGACTTGTCCG AAGGAGATGCGTATCTGCACCTATATTGACG-3'

DFX2: 5'-AGTCGAACGTCACTGCTATCAAGCTCGCAATGTGACTCGTCAATATAG GTGCAGATACGTGGACTCTGTGCGTG-3'

DFX3: 5'-(Cy3)CGGTGAATGGCACCACCGACACTACTGCAAGGAACGACTATCGC ACTCAAGAAACCACTGGGTACAAGCACAAC-3'

DFX4: 5'-TCGTTCCTTGCAGTAGTGTCGGATGAGCATGGGTCCCGTTGTGCTTGT ACCCAGTGGTTGAACACCTTCCAGCT-3'

DFX5: 5'-AGATGTCTACTCCTGTCGCAGCCTTCAGAGCAGCGTAGAAGAAGCTG GAAGGTGTTCCACACAGTCGCTCTCAGGCGT-3'

DFX6: 5'-TCCTGCTTCGTGTCCAGGTAACTGCGACAGGAGTAGACATCT-3'

DFX7: 5'-CTAGGACGGACGATGAAGCGTCAGCACTAGAACCGAGGAATG-3'

DFX8: 5'-AGTCACATTGCGAGCACGCTTCATCGTCCGTCCTAG-3'

DFX9: 5'-GTCAACTCGGGTCACCTGATACTGGTGCCATTCACCGGCTCCAGAGAC GACCAGGCAGTCATCTCCTTCGGACA-3'

DFX10: 5'-GGGACCCATGCTCATGTATCAGGTGACCCGAGTTGACCACGCACAGA GTCCAACTGCCTGGTCGTCTCTGGAGC-3'

DFX11: 5'-TCTTCTACGCTGCTCTGAAGGGCATCGAGGTTGCACACGCCTGAGAG CGACTGTGTGTCTTGAGTGCGATAG-3'

DFX12: 5'-GTGCAACCTCGATGCTTACCTGGACACGAAGCAGGA-3'

Figure 2.15 shows DFX molecules physisorbed on a mica surface and visualized via atomic force microscopy (AFM). The average length of the DFX nanostructure is measured (via AFM, 49 samples) to be 61.4 nm ± 6.1 nm, which is consistent with the design (189 nucleotides). The length of the DFX structure is well below its persistence length of ~100 nm [140]. This grants sufficient rigidity to the nanostructure, so that it can be regarded as a 1D nanorod.

For AFM imaging 5 μL of DFX solution is spotted onto freshly cleaved muscovite mica (Ted Pella, Inc.) The sample is left to adsorb for 3 min. To remove buffer salts, 20–30 μL of doubly distilled water is placed on the mica, the drop is

wicked off and the sample is dried with compressed air. Atomic force imaging is done utilizing a Nanoscope IV microscope (Digital Instruments) tapping in air, with ultra-sharp 16 series (NSC 16) tips purchased from MikroMasch.

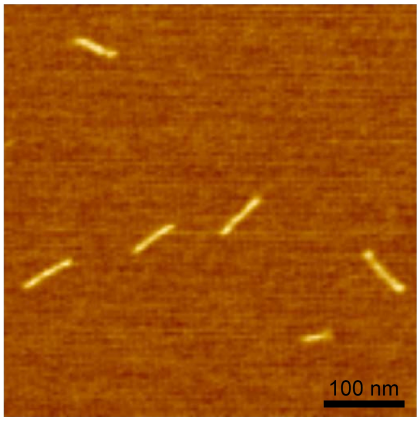

Figure 2.15: AFM image of the DFX nanostructure on a mica surface. The average length is ~61.4 nm ± 6.1 nm.

2.5.2 DFX DNA assembly on nanodot-pairs

For DFX assembly, the nanodots are patterned in arrays of dimers with an inter-dot spacing of 60 nm (Fig. 2.16) matching the length of the DFX molecule [141]. The dimers are spaced 2 μm apart in order to be optically resolvable (for fluorescence analysis) from neighboring pairs, and 400 nm apart for AFM studies. Fixed inter-dot spacing assures reproducibility of the binding conditions. Maintaining an inter-dimer spacing sufficiently greater than the inter-dot spacing eliminates “cross talk” between dimers, so that bivalent

binding can take place only between the two dots in each dimer. In addition, the nanodot size is close to the width of the DFX, so that, in principle, only one DFX should bridge the dimer gap. This affords precise control over the position and orientation of the DFX molecules on the substrate's surface.

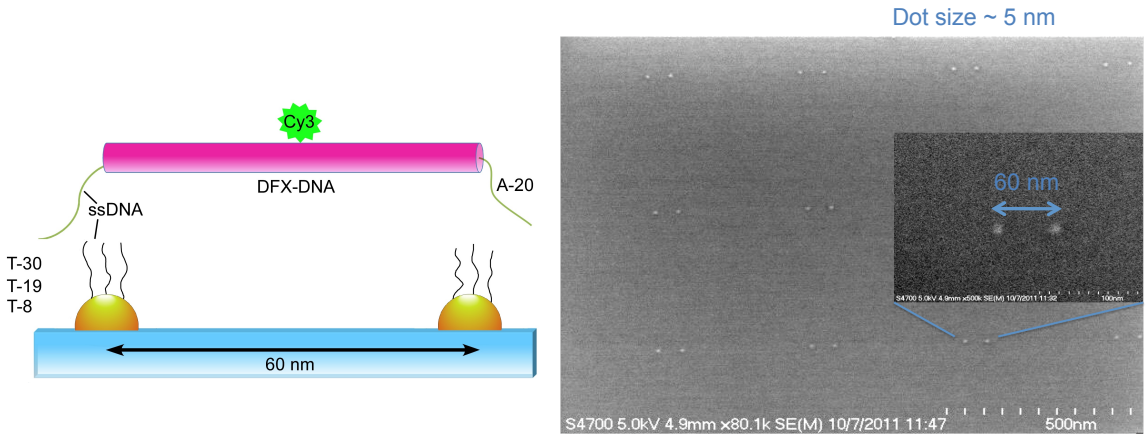

Figure 2.16: (Left) Schematic drawing of the DFX nanostructure attached to AuPd dot pairs 60 nm apart. The surface of the dots is functionalized with a thiol-ssDNA SAM. The length of the ssDNA is varied (30, 19 or 8 thymines). Single sticky-ends (20 adenines) extend from each end of the DFX. The distance between the two dots in one pair matches the length of DFX nanostructure. (Right) SEM image of an array of nanodots. Dimers are 400 nm apart.

A ssDNA SAM consisting of polythymines (i.e., complementary to the adenine linkers on the ends of the DFX) is formed on the nanodots through direct thiolation (method explained in section 2.3.1).

The system is designed to enable the DFX rods to bind to the nanodots via in situ hybridization, as shown schematically in Fig. 2.16. 15 µl of 10 nM DFX solution are dropped on the patterned area. The substrates are incubated in a humidified container for 4 h to allow hybridization. After the reaction, each

sample is dipped for 10 s in 10 ml of a mixture of ethanol (50%) and DI water (50%). The sample is then transferred to a well containing 10 ml of a 90% ethanol and 10% DI water solution, where it is allowed to sit for 50 min. It is then dried in air.

2.5.3 Results and discussion

Epifluorescence microscopy is used to measure the overall yield of DFX self-assembly over hundreds of μm^2 (up to 2500 μm^2 for each pattern) on uniform nanodot arrays on glass or fused silica substrates. Figure 2.17 shows that each and every dimer site is occupied by at least one DFX molecule. Images are collected with 300 ms exposure times, and analyzed with ImageJ.

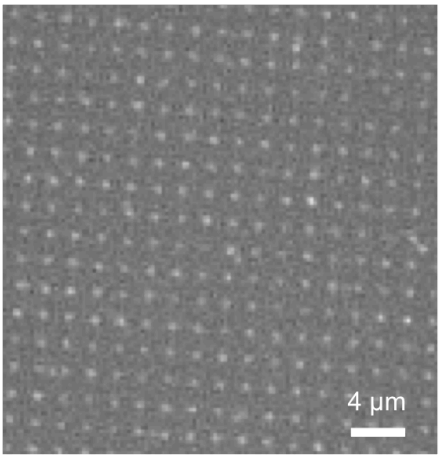

Figure 2.17: Epifluorescence microscopy image of the dot pairs array (on glass) bridged by DFX nanostructures (Cy3-labeled: Excitation wavelength: 550 nm, emission wavelength: 568 nm; exposure time: 300 ms). Each bright spot represents one dimer with 60 nm spacing. The dot pairs are spaced 2 µm apart.

Atomic force microscopy is used to characterize the DFX assembly with single

nanostructure resolution. For these measurements, the nanodot arrays are patterned on silicon wafers with a 300 nm-thick thermal oxide. Fig. 2.18 shows an array of nanodots bridged by DFX nanostructures. Consistent with the fluorescence microscopy observation, each nanodot dimer is bridged by at least one DFX. The AFM images also reveal that the DFX can bind to the nanodot dimers in different configurations. As seen in Fig. 2.18, the assembly results not only in the desired bivalent binding, in which a single DFX nanostructure is bridging a pair of nanodots, but there is evidence of monovalent attachment (i.e., attachment of DFX molecules to only one of the dots in a dimer), as well as multiple bridging, in which two or more DFX nanostructures bridge a pair of nanodots.

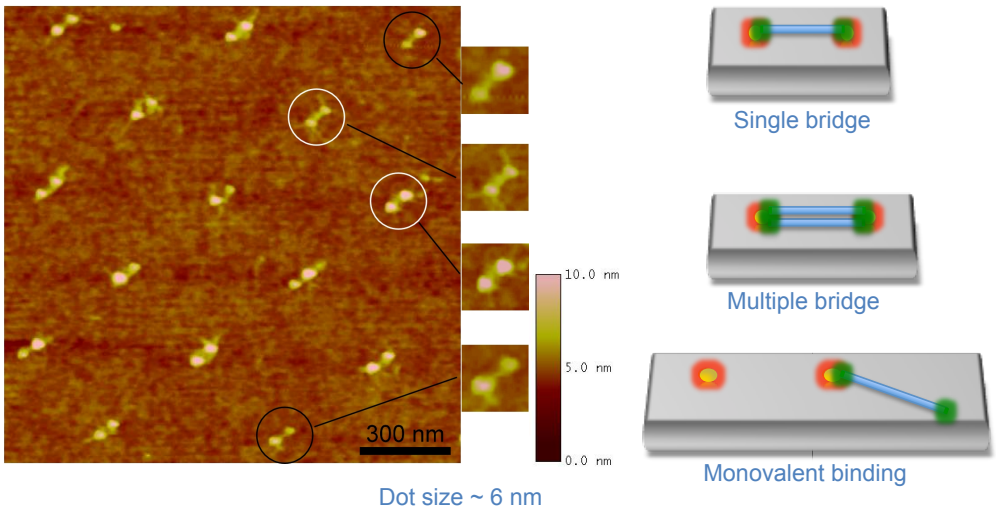

Figure 2.18: (Left) AFM image of dot pairs connected by DFX nanostructures. The surface of the dots is functionalized by 19T and the average dot size after functionalization is ~5.9 nm ± 1.0 nm. The distance between two dots is ~60 nm. Zoomed images display cases of single and multiple bridging (sometimes coexisting with monovalent binding). Single bridging is highlighted in black circles, multiple bridging is highlighted in white circles. (Right) Schematic of the possible binding configurations.

In order to determine the number of DFX molecules bridging each dot pair, height and width profiles (from topographical AFM images) of the DFX nanostructures interconnecting the nanodots are measured (Fig. 2.19 c and d). The average width and height of single DFX rods are determined by measuring the trace profiles on single DFX monovalently attached to individual nanodots (Fig. 2.19 a and b). This value is then used as a reference for comparison with the width of the DFX nanostructure bridging the nanodots. From this, the number of single vs multiple DFX bridging per dot pair can be determined. The analysis reveals a difference in the extent of multiple binding events, depending on the number of base pair matches between the ssDNA on the nanodots and the sticky ends on the DFX to which they hybridized.

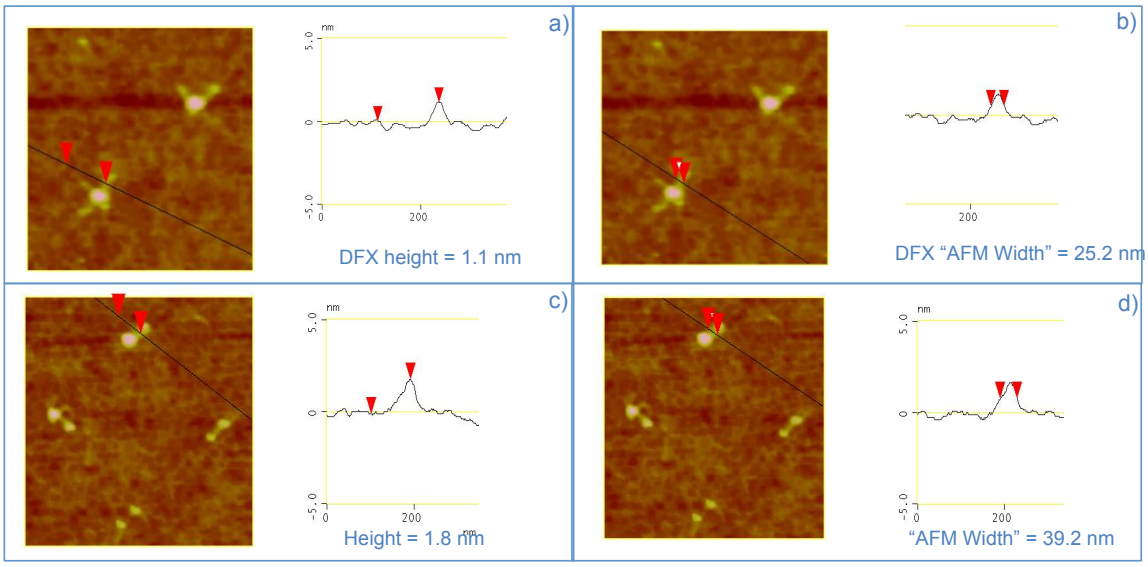

Figure 2.19: Cross-section profile analysis of AFM images showing single DFX nanostructures monovalently attached to the nanodots and DFX nanostructures connected to pairs of nanodots. (a) DFX height when monovalently bounded (1.1 nm). (b) Example of width measurement for DFX monovalently bounded. The average measured width is 25.2 nm (uncorrected for tip broadening) (86 measurements). These two values are used as reference

to discriminate between single and multiple DFX bridging a nanodots pair. If the height is less than 1.5 nm and width is less than 25 nm (uncorrected for tip broadening), the structure is evaluated as single bridging. (c) Example of height measurement for DFX bridging a nanodots-pair. The height of the bridging DFX nanostructure in this case is 1.8 nm so this is probably a case of multiple bridging. (d) The width is 39.2 nm (uncorrected for tip broadening) confirming the multiple bridging hypothesis.

The factors influencing the occurrence of one binding configuration vs. another are investigated by looking at the effects of the strength of the supramolecular interactions driving the self-assembly. This is done by systematically varying the length of the ssDNA functionalizing the nanodots, and hybridizing to the 20 adenines (A) on the DFX, from 8 to 30 thymines (T). With all three lengths of ssDNA on the dots (8T, 19T, or 30T) most of the DFX nanostructures have properly bridged the nanodot dimers with stable bivalent binding interactions, while some of them display monovalent attachment. The AFM scans show that the average number of nanodots presenting monovalently bound DFX motifs varies significantly with the number of base pairs (bp) available for hybridization, increasing from 48% to 69% when the linker length is varied from 8 bp to 19 bp (Fig. 2.20). In addition, the nanodots used with 30-thymine ssDNA (30T) are slightly larger (~8.5 nm ± 2.6 nm) than those used with the 8T and 19T (~5.9 nm ± 1.0 nm). The yield of monovalent attachment in this case (30T) goes up to 100% (i.e., on average every nanodot presented at least one monovalently bound DFX). Presumably, the larger dots can accommodate more ssDNA strands. This, together with the longer SAM layer on the dots surface, can dramatically increase the strength of the interaction with the DFX

nanostructure.

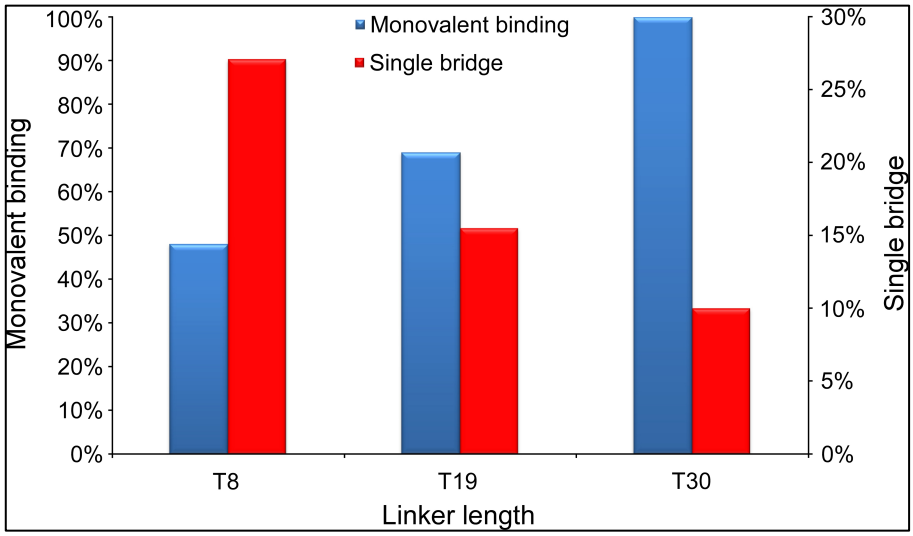

Figure 2.20: Histogram showing the yield of single-bridging and monovalent attachment of DFX to dots as a function of the thiol-ssDNA length on the dots surface. The single-bridging yield decreases as the length of ssDNA increases (red bars), while the monovalent attachment is found to increase with the length of the thiol-ssDNA functionalizing the dots (blue bars). The collected data for the T8 linker are from 96 measurements, for the T19 linker from 90 measurements, and for the T30 linker from 84 measurements.

Fig. 2.20 summarizes the results. Some 27.1% of the dot pairs functionalized with 8T exhibit single bridging, i.e., only one DFX molecule per dot pair. When the ssDNA on the nanodots is 19T this percentage decreases to 15.5%, while for nanodots functionalized with 30T, it goes down to 10.0%. This indicates that longer ssDNA on the dots surface can dramatically increase the hybridization possibility with DNA nanostructures, and therefore lead, as it is reasonable to expect, to multiple bridging of DFX per dot pair. The multibridging percentage increases indeed from ~70% to ~84%, as the SAM length increases from 8T to

19T. As the total length of ssDNA is extended, the access of DFX to the dot pairs is enhanced and this leads to higher yield of multiple bridging (90% for 30T in this case). So, while a small number of matching base pairs can improve the yield of single bridges, increasing the matching base pairs and the total length of the complementary strands, leads to higher yield of multiple bridging.

2.5.4 Thermodynamics of binding

In order to gain insight into the dependence of the DFX binding on the length of the ssDNA linker, a simple thermodynamic model has been developed to calculate the free energy of association ($\Delta G°$) for monovalent binding and for bivalent binding, as a function of the number of matching base pairs available for hybridization [141].

The calculations are performed for a bivalent system (two binding sites, given by the 20 adenines strands at the ends of the DFX molecule) with a rigid linking group (the DFX molecule itself) binding to anchoring points constrained on a surface (the poly-thymine strands on the dots), and spaced in a way to perfectly match the distance between the binding points of the bivalent system (see figure 2.16).

For this system, the change in enthalpy ($\Delta H°$) is entirely given by the DNA hybridization between the adenine strands on the DFX and the polythimines on the nanodots. The entropy change ($\Delta S°$) is due to both the DNA hybridization

and the motion of the rod.

The DNA hybridization contributions ($\Delta H°_{DNA}$, $\Delta S°_{DNA}$) are both calculated using thermodynamic nearest neighbor parameters for Watson-Crick base pairs [143]. The entropy change due to the motion of the rod is divided into rotational and translational components (there is no conformational component due to the rigidity of the rod).

$$\Delta G° = \Delta H° - T\Delta S° = \Delta H°_{DNA} - T \cdot [\Delta S°_{DNA} + (\Delta S°_{trans} + \Delta S°_{rot})_{rod}]$$

(All the thermodynamic quantities are for standard conditions, T = 298.15 K).

From the change in free energy ($\Delta G°$) the dissociation constant k_d is calculated according to:

$$\Delta G° = RT \cdot ln(k_d)$$

Monovalent binding

The change in free energy for monovalent binding is:

$$\Delta G°_{mono} = \Delta H°_{DNA\text{-}mono} - T \cdot [\Delta S°_{DNA\text{-}mono} + (\Delta S°_{trans\text{-}mono} + \Delta S°_{rot\text{-}mono})_{rod}]$$

The enthalpy change ($\Delta H°_{DNA\text{-}mono}$) is due only to the hybridization of the 20 adenine strand on the DFX to a complementary poly-thymine strand (8,19 or 30 thymines) on the nanodots, and it is calculated via the IDT online software "Thermodynamic calculator" (http://biophysics.idtdna.com) setting the parameters:

oligo and target concentration = 10 nM, Mg^{2+} concentration = 12.5 mM

This software calculates the standard enthalpy ($\Delta H°$), entropy ($\Delta S°$) and free energy ($\Delta G°$) of hybridization for free ssDNA in solution depending on DNA sequence (oligo and target), DNA concentration (oligo and target), and concentration of ions (Na^+, K^+, Mg^{2+}). It uses a nearest-neighbor model and various thermodynamic parameters [144-146].

The entropy change has three contributions: one due to the DNA hybridization ($\Delta S°_{DNA\text{-}mono}$) the other two due to the translational and rotational motion of the rod ($\Delta S°_{trans\text{-}mono}$ and $\Delta S°_{rot\text{-}mono,}$ respectively).

Thermodynamically, the system can be considered to be isolated and in equilibrium (volume, number of molecules and internal energy are fixed); the entropy is thus given by:

$$S = R \cdot \ln(V)$$

where R is the gas constant and V is the volume accessible to each molecule. For the rod, the loss in translational entropy upon monovalent attachment ($\Delta S_{trans\text{-}mono}$) is given by:

$$\Delta S_{trans-mono} = R \cdot \ln\left(\frac{V_{f-rod-trans}}{V_{i-rod-trans}}\right)$$

where $V_{i\text{-}rod\text{-}trans}$ and $V_{f\text{-}rod\text{-}trans}$ are the volume accessible to each molecule for a translational motion in the initial and in the final state respectively. The initial state corresponds to the rod free in solution, so:

$$V_{i-trans} = \frac{1}{conc \cdot N_A} = 0.166 \times 10^{-9} mm^3$$

where *conc* is the DFX molar concentration in solution, equal to 10 nM, and N_A is Avogadro's number.

In the case of monovalent binding the final state corresponds to the rod attached only to one dot. The final accessible volume is equal to the truncated spherical sector spanned by the rod when attached to the dot (Fig. 2.21). The motion on the nanodot is due to the fact that SAMs of thiolated molecules on Au are mobile with a velocity that depends on the nature of the molecule and the curvature of the substrate : for this calculation the value 10 Å/hour was used [147-149].

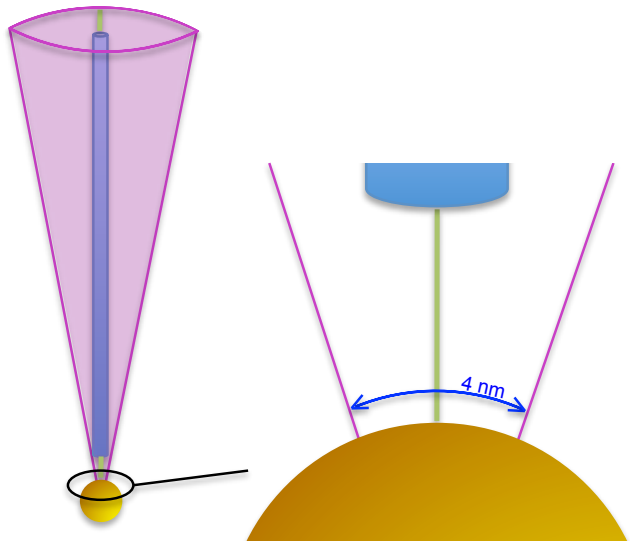

Figure 2.21: Schematic of the volume available for translational motion of the DFX molecule upon monovalent binding (truncated spherical sector in purple).

The value of the final volume will then be given by:

$V_{f\text{-}trans} = 153.7\times10^{-15}\ mm^3$

The final loss in translational entropy upon monovalent attachment ($\Delta S_{trans\text{-}mono}$) is therefore:

$\Delta S_{trans\text{-}mono} = -58.1\ JK^{-1}mol^{-1}$

The loss in rotational entropy of the rod upon binding to one dot ($\Delta S_{rot\text{-}mono}$) is given by the ratio of the volume spanned by free rotation in solution (a sphere), and by the volume spanned when constrained by the binding to the dot on the surface, which reduces to a semi-sphere:

$$\Delta S_{rot-mono} = R \cdot \ln\left(\frac{V_{f-rot}}{V_{i-rot}}\right) = R \cdot \ln\left(\frac{\frac{2}{3}\pi r^3}{\frac{4}{3}\pi r^3}\right) = -5.76\frac{J}{mol \cdot K}$$

where r is the length of the DFX.

In order to calculate $\Delta S_{DNA\text{-}mono}$ we have to then take into account that one of the ssDNA strands (the poly-T on the dot) is attached to the nanodot surface and has therefore a limited initial translational entropy; this leads to an increase (in absolute value) of $R \cdot \ln(2) = 5.67\ JK^{-1}mol^{-1}$ to the entropy change (as calculated using the IDT software).

$\Delta S_{DNA\text{-}mono} = \Delta S_{IDTsoftware} - R \cdot \ln(2)$

Bivalent binding

As in the previous case, the expression of the change of free energy in the case of bivalent binding is:

$\Delta G°_{bi} = \Delta H°_{DNA\text{-}bi} - T \cdot [\Delta S°_{DNA\text{-}bi} + (\Delta S°_{trans\text{-}bi} + \Delta S°_{rot\text{-}bi})_{rod}]$

For each bivalent binding event two DNA strands hybridize; therefore the enthalpy change is twice that of the monovalent case (i.e. $\Delta H_{bi} = 2\Delta H_{mono}$) [121, 150].

For the rod, the loss in translational entropy upon bivalent attachment ($\Delta S_{trans\text{-}bi}$) is:

$$\Delta S_{trans-bi} = R \cdot \ln\left(\frac{V_{f-rod-trans}}{V_{i-rod-trans}}\right)$$

The initial state is the same as in the previous case (free rod in solution) so the initial volume accessible to each molecule for a translational motion ($V_{i\text{-}trans}$) is again:

$$V_{i-trans} = \frac{1}{conc \cdot N_A} = 0.166 \times 10^{-9} mm^3$$

where *conc* is the DFX molar concentration in solution, equal to 1 nM, and N_A is Avogadro's number.

When bivalently bound, the rod can only translate on the dot surface via motion of the thiolated DNA molecules on the dot (as in the previous case, a velocity of 10 Å/hour was used)[147-149]. The volume spanned is approximately a cylinder with base radius r = 3 nm (equal to the radius of the nanodots) and height h = 60 nm (which is the distance between the dots) minus the volume of the two dots, which are not accessible to the molecules (Fig. 2.22).

Figure 2.22: Schematic of the volume available for translational motion of the DFX molecule upon bivalent binding (purple area).

The final volume accessible to each molecule for a translational motion ($V_{f\text{-}trans}$) is thus equal to:

$$V_{f-trans} = \left(\pi r^2 \times h\right) - \frac{4}{3}\pi r^3 = 1583.36 \times 10^{-18} mm^3$$

where r = 3 nm is the nanodot radius, h = 60 nm is the spacing between the two nanodots.

From these values:

$\Delta S_{trans\text{-}bi}$ = - 96.12 $JK^{-1}mol^{-1}$

The loss in rotational entropy of the rod upon binding to two dot ($\Delta S_{rot\text{-}bi}$) is given by the ratio of the volume spanned by free rotation in solution (a sphere) and by the volume spanned when constrained by the bivalent binding; this corresponds to two cones with base radius r = 3 nm (equal to the radius of the nanodots) and height h = 30 nm (which is half the distance between the dots), minus the volume of the two dots, which are not accessible to the molecules (Fig. 2.23).

$$\Delta S_{rot-bi} = R \cdot \ln\left(\frac{V_{f-bi-rot}}{V_{i-bi-rot}}\right) = R \cdot \ln\left(\frac{2\left(\frac{1}{3}\pi r^2 h - \frac{2}{3}\pi r^3\right)}{\frac{4}{3}\pi h^3}\right) = -45.9 \frac{J}{mol \cdot K}$$

The initial volume corresponds to the sphere spanned when rotating free in solution (rotation around the center of mass).

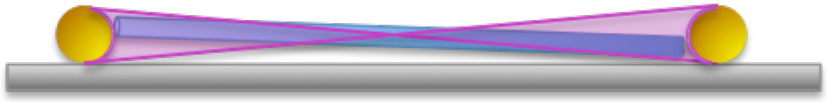

Figure 2.23: Schematic of the volume available for rotational motion of the DFX molecule upon bivalent binding (purple area).

Again $\Delta S_{DNA\text{-}bi}$ is calculated from the value given by the IDT software, taking into account that in this case we are looking at the hybridization of two separate pairs of complementary strands of ssDNA in which two strands are constrained on a surface and the two complementary strands are attached to a rigid rod in solution. We need thus to adjust the value given by the IDT software for the hybridization of two pairs of strands ($2\Delta S_{IDTsoftware}$) adding (in absolute value) $2R \cdot \ln(2)$ = - 11.34 $JK^{-1}mol^{-1}$ which accounts for the strands being constrained on the surface, and adding the value:

$$R \cdot \ln\left(\frac{0.166 \times 10^{-9}}{4/3\,\pi\left(67^3 - 60^3\right) \times 10^{-18}}\right) = 51.1 \frac{J}{mol \cdot K}$$

accounting for the complementary strands being attached to the rigid rod.

$$\Delta S_{DNA-bi} = 2\Delta S_{IDTsoftware} - 2R \cdot \ln(2) + R \cdot \ln\left(\frac{0.166 \times 10^{-9}}{4/3\,\pi(67^3 - 60^3) \times 10^{-18}}\right)$$

(The entropy of hydration has been ignored in all cases; the entropic changes in hydration/dehydration that accompany the biological interactions occurring in the case under examination would simply add a constant value to each entropy term discussed).

The values of $\Delta H°_{DNA}$ and $\Delta S°_{DNA}$ depend on the length of the thymine strands on the nanodots, so they are calculated separately for each case.

8T

$\Delta H_{mono} = \Delta H_{T8\text{-}A20} = -214.2\ kJ \cdot mol^{-1}$

$\Delta S_{mono} = (\Delta S_{trans\text{-}mono} + \Delta S_{rot\text{-}mono})_{rod} + \Delta S_{DNA\text{-}mono} = -692.82\ J \cdot K^{-1}\ mol^{-1}$

$\Delta S_{trans\text{-}mono(rod)} = -58.1\ J \cdot K^{-1}\ mol^{-1}$

$\Delta S_{rot\text{-}mono(rod)} = -5.76\ J \cdot K^{-1}\ mol^{-1}$

$\Delta S_{DNA\text{-}mono} = DS_{IDTsoftware} - Rln(2) = -623.2 - 5.76 = -628.96\ J \cdot K^{-1}\ mol^{-1}$

$\Delta G_{mono} = (\Delta H_{mono} - T\Delta S_{mono}) = -7.64\ kJ \cdot mol^{-1}$

$\Delta S_{bi} = (\Delta S_{trans\text{-}bi} + \Delta S_{rot\text{-}bi})_{rod} + \Delta S_{DNA\text{-}bi} = -1337.24\ J \cdot K^{-1}\ mol^{-1}$

$\Delta S_{trans\text{-}bi} = -96.12\ J \cdot K^{-1}\ mol^{-1}$

$\Delta S_{rot\text{-}bi} = -45.9\ J \cdot K^{-1}\ mol^{-1}$

$$\Delta S_{DNA-bi} = 2\Delta S_{IDTsoftware} - 2R \cdot \ln(2) + R \cdot \ln\left(\frac{0.166 \times 10^{-9}}{\frac{4}{3}\pi(67^3 - 60^3) \times 10^{-18}}\right) = 2 \cdot (-617.49) -$$

$11.34 + 51.1 = 1195.22\ J \cdot K^{-1}\ mol^{-1}$

$\Delta G_{bi} = (2\Delta H_{mono} - T\Delta S_{bi}) = -72.05\ kJ \cdot mol^{-1}$

$k_{d(mono)} = 4.6 \cdot 10^{-2}\ M$

$k_{d(bi)} = 2.4 \cdot 10^{-13}\ M$

19T

$\Delta H_{mono} = \Delta H_{T19\text{-}A20} = -577.8\ kJ \cdot mol^{-1}$

$\Delta S_{mono} = (\Delta S_{trans\text{-}mono} + \Delta S_{rot\text{-}mono})_{rod} + \Delta S_{DNA\text{-}mono} = -1739.62\ J \cdot K^{-1}\ mol^{-1}$

$\Delta S_{trans\text{-}mono(rod)} = -58.1\ J \cdot K^{-1}\ mol^{-1}$

$\Delta S_{rot\text{-}mono(rod)} = -5.76\ J \cdot K^{-1}\ mol^{-1}$

$\Delta S_{DNA\text{-}mono} = \Delta S_{IDTsoftware} - R\ln(2) = -1670 - 5.76 = -1675.76\ J \cdot K^{-1}\ mol^{-1}$

$\Delta G_{mono} = (\Delta H_{mono} - T\Delta S_{mono}) = -59.13\ kJ \cdot mol^{-1}$

$\Delta S_{bi} = (\Delta S_{trans\text{-}bi} + \Delta S_{rot\text{-}bi})_{rod} + \Delta S_{DNA\text{-}bi} = -3442.26\ J \cdot K^{-1}\ mol^{-1}$

$\Delta S_{trans\text{-}bi} = -96.12\ J \cdot K^{-1}\ mol^{-1}$

$\Delta S_{rot\text{-}bi} = -45.9\ J \cdot K^{-1}\ mol^{-1}$

$$\Delta S_{DNA-bi} = 2\Delta S_{IDTsoftware} - 2R \cdot \ln(2) + R \cdot \ln\left(\frac{0.166 \times 10^{-9}}{4/3\,\pi(67^3 - 60^3) \times 10^{-18}}\right) = 2 \cdot (-1670) -$$

$11.34 + 51.1 = -3300.24\ J \cdot K^{-1}\ mol^{-1}$

$\Delta G_{bi} = (2\Delta H_{mono} - T\Delta S_{bi}) = -129.29\ kJ \cdot mol^{-1}$

$k_{d(mono)} = 4.4 \cdot 10^{-11}\ M$

$k_{d(bi)} = 2.2 \cdot 10^{-23}\ M$

30T

$\Delta H_{mono} = \Delta H_{T30\text{-}A20} = -597\ kJ \cdot mol^{-1}$

$\Delta S_{mono} = (\Delta S_{trans\text{-}mono} + \Delta S_{rot\text{-}mono})_{rod} + \Delta S_{DNA\text{-}mono} = -1786.32\ J \cdot K^{-1}\ mol^{-1}$

$\Delta S_{trans\text{-}mono(rod)} = -58.1\ J \cdot K^{-1}\ mol^{-1}$

$\Delta S_{rot\text{-}mono(rod)} = -5.76\ J \cdot K^{-1}\ mol^{-1}$

$\Delta S_{DNA\text{-}mono} = DS_{IDTsoftware} - Rln(2) = -1716.7 - 5.76 = -1722.46\ J \cdot K^{-1}\ mol^{-11}$

$\Delta G_{mono} = (\Delta H_{mono} - T\Delta S_{mono}) = -64.4\ kJ \cdot mol^{-1}$

$\Delta S_{bi} = (\Delta S_{trans\text{-}bi} + \Delta S_{rot\text{-}bi})_{rod} + \Delta S_{DNA\text{-}bi} = -3535.66\ J \cdot K^{-1}\ mol^{-1}$

$\Delta S_{trans\text{-}bi} = -96.12\ J \cdot K^{-1}\ mol^{-1}$

$\Delta S_{rot\text{-}bi} = -45.9\ J \cdot K^{-1}\ mol^{-1}$

$$\Delta S_{DNA-bi} = 2\Delta S_{IDTsoftware} - 2R \cdot \ln(2) + R \cdot \ln\left(\frac{0.166 \times 10^{-9}}{4/3\,\pi(67^3 - 60^3) \times 10^{-18}}\right) = 2 \cdot (-1716.7) -$$

$11.34 + 51.1 = -3393.64\ J \cdot K^{-1}\ mol^{-1}$

$\Delta G_{bi} = (2\Delta H_{mono} - T\Delta S_{bi}) = -139.84\ kJ \cdot mol^{-1}$

$k_{d(mono)} = 5.2 \cdot 10^{-12}\ M$

$k_{d(bi)} = 3.2 \cdot 10^{-25}\ M$

The results of the model indicate that in all cases the bivalent association is significantly stronger – by several orders of magnitude - than the monovalent association. This finding is in line with the experimentally observed high yield of bivalent binding of DFX on dot pairs for all three lengths of ssDNA linkers on the dots (8T, 19T, or 30T), as seen in Fig. 2.17. For the 19T and 30T cases the values of k_d range from ~10^{-11} M and ~10^{-12} M for monovalent binding, to ~10^{-23} M and ~10^{-25} M for bivalent attachment, respectively. These values are representative of a strong (but still reversible) monovalent binding, and a highly stable bivalent attachment, in line with the high percentage of monovalent binding and the close to perfect yield of bivalent attachment observed. For 8T the calculated k_d for monovalent binding was found to be ~10^{-2} M, while we determined a k_d of ~10^{-13} M for the bivalent binding. The bivalent k_d value for 8T approaches the one for the well-known avidin–biotin binding system, for which k_d ~ 10^{-15} M, and is considered to be essentially irreversible [151]. This again explains the close to perfect yield of bivalent binding of DFX also in the case of 8T. On the other hand, our findings suggest a lower affinity for the monovalent attachment of the DFX rod on nanodots functionalized with a 8T monolayer, with a calculated value for k_d ~ 10^{-2} M. Such a low monovalent affinity can indeed favor a higher degree of rearrangement of the DFX on one dot dimer (allowing some degree of detachment of monovalently bound structures). This is generally consistent with the experimental observation that the single attachment per dot is lower for 8 bp than for 19 bp, the latter exhibiting a higher affinity for monovalent attachment. We note that the experimentally observed rate of monovalent attachment (~48%) for the 8T linker

is rather higher than the calculated k_d value would suggest. We note that the model does not account for the presence of multiple strands on the nanodots, which would increase the probability of binding relative to the case of a single strand used in our model. This is supported by the observed additional increase in monovalent binding for the 30T case, where the nanodots are larger than for the 8T and 19T cases, as noted above. In addition, physisorption of DFX molecules on the silicon substrate surface once monovalently bound to a nanodot would tend to inhibit rearrangement.

2.6 Assembly of 2D DNA nanostructures: DNA origami

2.6.1 DNA origami

DNA origami is a type of DNA nanostructure formed from a long single-stranded M13mp18 genomic (M13) DNA, which is folded into predefined forms with the help of short staple strands [17]. By selecting the sequence of the staple strands, a wide variety of shapes are obtainable, creating nano-objects in two or three dimensions. DNA origami can be synthesized with attachment groups (such as biotin or single-stranded DNA hooks) at defined locations, which can bind a variety of nanoobjects, ranging from peptides and proteins to metallic nanoparticles, quantum dots and carbon nanotubes [31, 34]. DNA origami typically carry about 200 independently addressable binding sites at a

resolution of 6 nm.

The versatility and precision of DNA origami functionalization make them attractive as a scaffold for the organization of nanomaterials on surfaces. However, because the origami are synthesized in solution, simply allowing them to adsorb on surfaces in an uncontrolled fashion results in random arrangements. In order to use DNA origami to build new novel functional nanodevices, it is necessary to develop techniques to control their deposition on desired locations on a substrate. One approach toward achieving this goal is based upon the same concept used for the DFX. Here, two-dimensional DNA origami triangles are synthesized functionalized with sticky-ends on the corners (Fig. 2.24). The choice of triangular shape is dictated by the greater rigidity of this structure compared with other 2D origami shapes (e.g. rectangles).

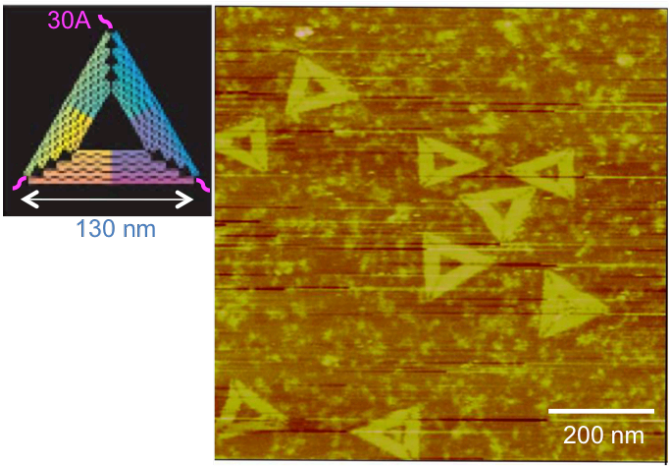

Figure 2.24: (Left) Schematic of DNA origami triangle with 30 adenines sticky-ends on the corners. (Right) Liquid AFM image of triangular DNA origami physisorbed on a mica surface. The apparent longer side (greater than 130 nm) is due to tip broadening.

Nanodots are patterned in clusters with arrangement matching the shape of the DNA origami and they are functionalized with ssDNA complementary to the sticky-ends on the origami corners. According to this scheme, when incubating the DNA origami solution on the functionalized nanodots, the DNA origami would selectively bind to the nanodots through DNA hybridization (Fig. 2.25). Inspired by the mechanisms of polyvalent binding, the presence of multiple binding sites should enable precise control over the binding position on the substrate and over the orientation of each single DNA origami.

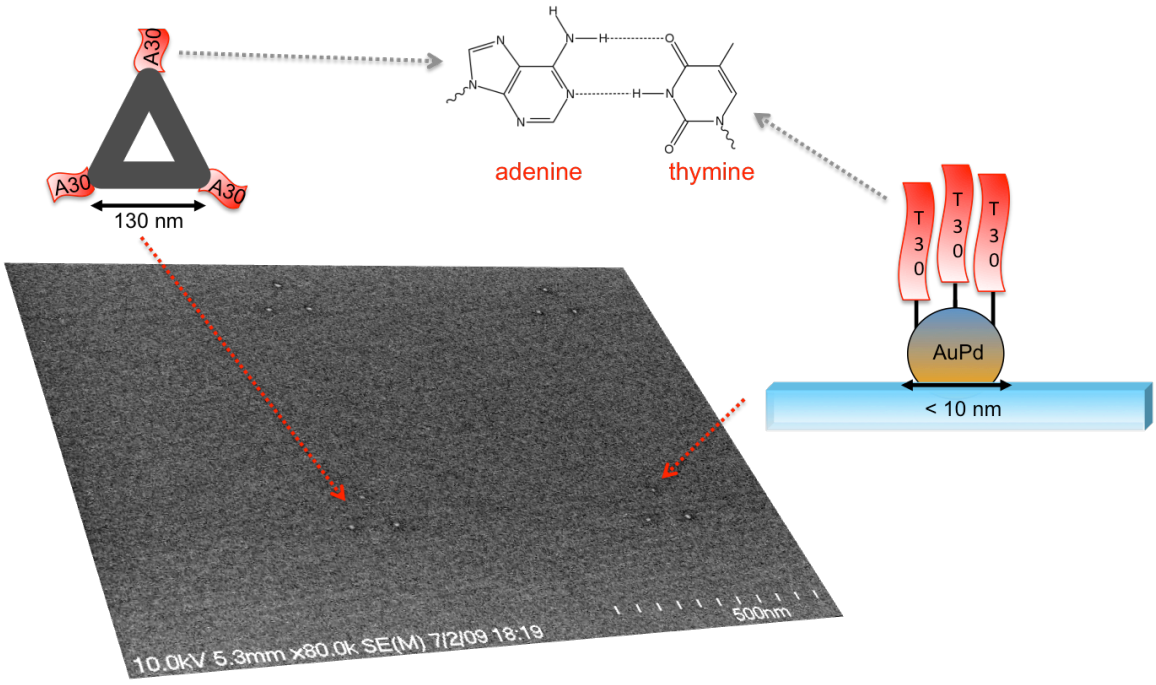

Figure 2.25: SEM image of patterned AuPd nanodots arranged in triangular clusters. Nanodots are functionalized with a SEM of thiolated ssDNA (30 thymines); DNA origami have 30 adenines sticky-ends on the corners. DNA origami bind to the nanodots through DNA hybridization.

Triangular DNA origami with corners functionalized with poly-adenines (30A) were received from Jennifer Cha's laboratory at UCSD. The origami are assembled according to a published procedure[17] in a standard thermal cycler (Applied Biosystems Geneamp PCR System 9700). ssDNA staples are obtained from Integrated DNA Technologies (Coralville, IA), and single-stranded M13mp18 phage DNA (M13) is obtained from New England Biosciences. All chemicals are obtained from Sigma Aldrich, unless otherwise stated. In each 50 μL PCR tube, 5 μL 10X TAE buffer (400 mM Tris acetate, 10 mM EDTA, 20 mM Na^+) with 125 mM $MgCl_2$ (to make 12.5 mM $MgCl_2$ in the 1X solution) is mixed with 5 μL of ~ 10 nM single-stranded circular M13 DNA, enough staple solution to make 100 nM of each staple in 50 μL final volume, and enough distilled H_2O to make 50 μL total solution per tube. The program used to anneal the DNA in the thermal cycler is as follows: 1) heat to 90 ºC and hold for 5 minutes, 2) cool at the slowest ramp rate to 20 ºC, 3) repeat steps one and two, and 4) cool to 4 ºC and hold until sample retrieval. Step three is not necessary for high-quality origami formation; it is present due to programming restrictions of the thermal cycler. Four staples at each corner are modified by extending 30 adenine nucleotides on the 3' end (see [108] for details about the DNA strands). These A30-modified DNA staples are introduced into the DNA scaffolds in place of the original staples. After thermal cycling, excess staples are removed by filtering the origami solution through a Nanosep 30 kDa molecular weight cutoff (MWCO) centrifuge filter (Pall) using a benchtop microcentrifuge (Sorvall Biofuge Fresco) at 4000 rpm at 4 ºC. In a single filter, 50 μl of origami solution is

washed two times with 450 µl of 10X TAE (400 mM tris acetate, 10 mM EDTA) and 125 mM $MgCl_2$, spinning down to ~ 50 µl of sample each time. Care must be taken not to centrifuge the filter to dryness, as the origami will stick to the filter, resulting in significant loss of sample. The solution is brought to a volume of 50 µl, an origami concentration of ~ 1.4 nM, and stored at 4 ºC until use.

The purity of the origami solution is checked by gel electrophoresis. 2-4µl of original DNA origami solution and 2-4 µl of purified origami solution are loaded in 1% agarose gel (1 g of agarose in 100 ml 1X TBE buffer) pre-staining with Ethidium Bromide (10 µl of 50 mg/ml EtBr solution per 100 ml agarose solution). From the gel it can be observed that after two filtrations there is still some ssDNA present in the solution (Fig. 2.26b). Further purification results in loss of the origami (Fig. 2.26c). The residual ssDNA is composed of a mixture of strands with different sequences and, as long as the concentration of poly-adenines is not too high, they are not expected to saturate the poly-thymines on the nanodots. Indeed, in order to get high yield of origami binding to poly-thymines functionalized nanodots, it is necessary to remove enough of free poly-adenines from the origami solution. An excess of free poly-adenines can saturate all the poly-thymines on the nanodots and thus prevent the origami from binding. Due to the loss of origami after three filtrations, two filtration steps are used for the assembly.

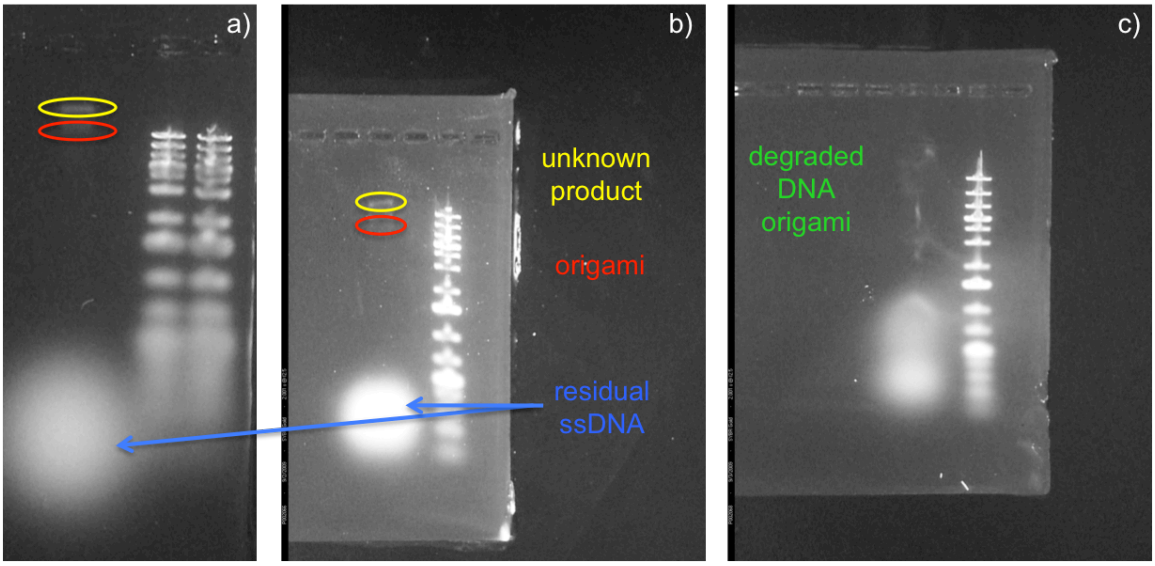

Figure 2.26: Gel electrophoresis of the DNA origami solution unpurified (a), after two purification cycles (b) and after three purification cycles (c). Two purification cycles are not sufficient to remove all the extra ssDNA (b) but a third filtration results in loss of the origami (c). The band labeled as "unknown material" is probably excessively conjugated M13.

2.6.2 DNA origami assembly on nanodot-clusters

Substrates are patterned with clusters of nanodots arranged to form an equilateral triangle (Fig. 2.24). The inter-dot distance is varied from 90 nm to 120 nm in different arrays in order to see if there is a preferred spacing that maximizes origami binding (the triangular DNA origami have nominally 130 nm side, but the poly-adenine sticky ends are designed to be 120 nm apart, also the origami are observed to shrink upon drying). The nanodots are functionalized with 30 thymines (30 T) either through direct thiolation or the biotin/streptavidin scheme. Alternatively, hybridization of 30T to DNA origami triangles is done in solution, with the aim of functionalizing the origami corners

with alternate functional groups (biotin or thiol) that would then drive the direct attachment to the nanodots. In this second case a further purification step is needed to remove any excess of 30T-(biotin or thiol). This purification is done following the previously described procedure. 6 µl of the purified origami solution are dropped on the pattern area and incubated in a sealed humidified container. Different incubation conditions are attempted with the purpose of maximizing the desired binding configuration (all three origami corners attached to the three nanodots constituting one triangular cluster) as summarized in Table 2.1.

NANODOT FUNCTIONALIZATION	SUBSTRATE PASSIVATION	ORIGAMI BUFFER	ORIGAMI FUNCTIONALIZATION	INCUBATION TEMPERATURE	INCUBATION TIME
Direct thiolation	None	TAE Mg^{2+}	No	RT	3 to 6 hours
Direct thiolation	HMDS	TAE Mg^{2+}	No	RT	3 hours*
Direct thiolation	PEG	TAE Mg^{2+}	No	RT	3 to18 hours (overnight)**
Direct thiolation	None	TAE Mg^{2+} NaCl	No	RT	2 hours***
Direct thiolation	None	TAE Mg^{2+}	No	40 ºC	2 hours****
None	None	TAE Mg^{2+}	Hybridization to thiol-30T	RT	18 hours (overnight)
Biotin/streptavidin/ biotin-30T	PEG	TAE Mg^{2+}	No	RT	18 hours (overnight)
Biotin/streptavidin	PEG	TAE Mg^{2+}	Hybridization to biotin-30T	RT	18 hours (overnight)

Table 2.1: Different conditions for binding of DNA origami triangles to nanodots clusters.

TAE Mg^{2+} = 10X TAE (400 mM tris acetate, 10 mM EDTA) and 125 mM $MgCl_2$.

TAE Mg^{2+} NaCl = Buffer with high concentration of ions. 10X TAE (400 mM tris acetate, 10 mM EDTA) and 125 mM $MgCl_2$ plus 2 µl of a saturated NaCl solution.

* Longer incubation time results in degradation of the HMDS layer.

** PEG doesn't get degraded for long incubation in buffered solutions.

*** The incubation time was reduced to 2 hours in order to minimize possible salt precipitation on the origami.

**** Incubation time was reduced in order to avoid evaporation of the solution and consequent drying or excessive salt concentration.

The HMDS passivation, done prior the thiolation step, consists in the formation of a monolayer of hexamethyldisilazane (HMDS, Alfa Aesar) deposited by exposing the cleaned, with oxygen plasma, patterned wafers (preheated at 185 °C on a hot plate) to HMDS vapor for 10 minutes in a glass chamber.

Directly after incubation, samples are imaged using an AFM liquid imaging cell (Veeco IV). 20 µl of 1X TAE buffer with 125 mM $MgCl_2$ are added to the AFM tip (Veeco SNL-10) prior to approaching the sample. In order to image the samples by AFM under dry conditions (Park System XE-100, tips: Mikro Mash NSC16 /AIBS), a solvent exchange is performed prior to drying. This is necessary in order to reduce precipitation of salts from the buffer. Each buffered sample is dipped for 10 seconds in 4 ml of a mixture of anhydrous ethanol (50%) and DI water (50%). It is then transferred to a well containing 4 ml of a 90% anhydrous ethanol 10% DI water solution, where it is allowed to sit for 50 minutes. The samples are finally dipped in pure ethanol and then air dried.

2.6.3 Results and discussion

The different incubation strategies listed above yield different binding outcomes. Anytime the substrates are passivated with a hydrophobic coating (PEG or HMDS) no origami binding is observed, neither to the nanodots nor random physisorption on the SiO_2 surface. This is the case irrespective of the linking chemistry (i.e., biotin/streptavidin or through DNA hybridization). When the origami binding is by mean of the biotin/streptavidin interaction, the dots are functionalized with streptavidins and biotin functionalized ssDNA is hybridized to the sticky-ends on the origami corners in solution, so that the biotin groups are located at the end of dsDNA protruding from the origami corners. When the origami binding is done through DNA hybridization, the dots are functionalized with ssDNA attached to streptavidins through a biotin group or attached directly to the nanodots through a thiol group. While the surface passivation eliminates non specific binding, no binding to the nanodots is observe either, probably due to the repulsion between the charged origami surface and the hydrophobically passivated substrate surface.

The best results are obtained for nanodots functionalized with ssDNA (30T) through direct thiolation and hybridization to DNA origami either at RT or at 40 ºC. In these cases the desired binding configuration is obtained, meaning all corners of the origami attached to a nanodot, resulting in the correct positioning of the origami on the nanodots cluster, although the yield is quite low (less than 10%) (Fig. 2.27).

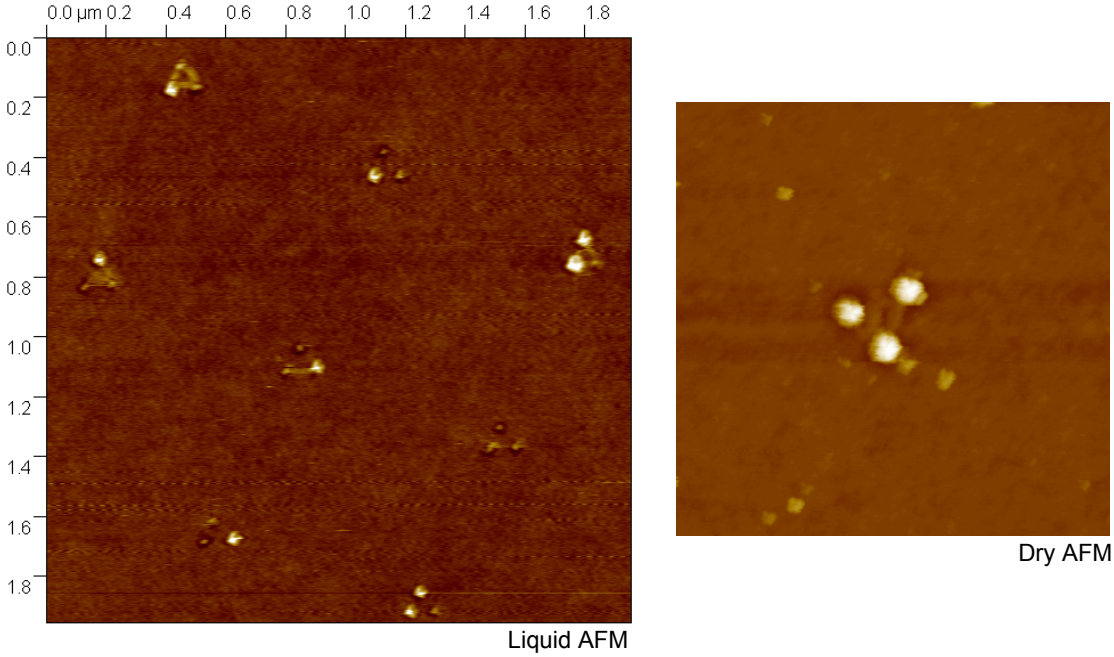

Figure 2.27: Triangular DNA origami attached to clusters of nanodots arranged in trimers with 110 nm inter-dot spacing. The nanodots are functionalized with ssDNA (30T) through direct thiolation; the origami bind to the nanodots through DNA hybridization. (Left) AFM image in liquid conditions. (Right) Dry AFM image. The sample is dried through a solvent exchange in DI water/ethanol mixtures.

The most commonly observed binding configuration is monovalent or bivalent binding, where one corner of the origami is attached to one or two nanodots and the origami is laying on one side of the cluster (Fig. 2.28). Of course this kind of binding doesn't achieve the positional and rotational precision of the complete binding to the nanodots clusters.

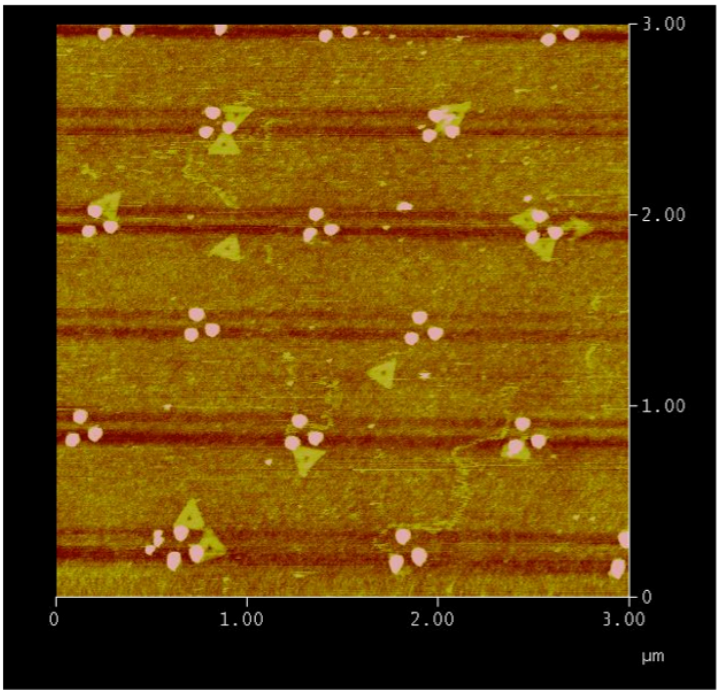

Figure 2.28: Liquid AFM of triangular DNA origami attached to clusters of nanodots arranged in trimers with 110 nm inter-dot spacing. The nanodots are functionalized with ssDNA (30T) through direct thiolation; the origami bind to the nanodots through DNA hybridization. The image displays origami attached monovalently (one corner attached to none nanodot) and bivalently (two corners attached to two nanodots in one cluster). Random physisorption to the substrate is also visible.

The reason for the prevalence of this partial binding probably resides in the strong interaction between the charged origami surface (the origami are in a solution with high concentration of monovalent and divalent ions to allow for DNA hybridization and to maintain the origami structure itself) and the hydrophilic silicon oxide that constitutes the surface of the samples. (The silicon oxide is hydrophilic because of the treatment with aged piranha and uv-ozone that is necessary to obtain a proper functionalization of the dots with

thiolated molecules). Occasionally salt accumulation is observed on origami after drying (Fig. 2.29). The problem is observed mostly for samples with incubation in buffer with high NaCl concentration (this approach is attempted to increase the hybridization yield). The salt does not completely remove with the DI water/ethanol wash, and washing with pure DI water (dipping the sample in a 5 ml volume for 5 seconds) results in complete removal of the origami (previously attached to the nanodots, as observed with liquid AFM or with regular AFM, after drying).

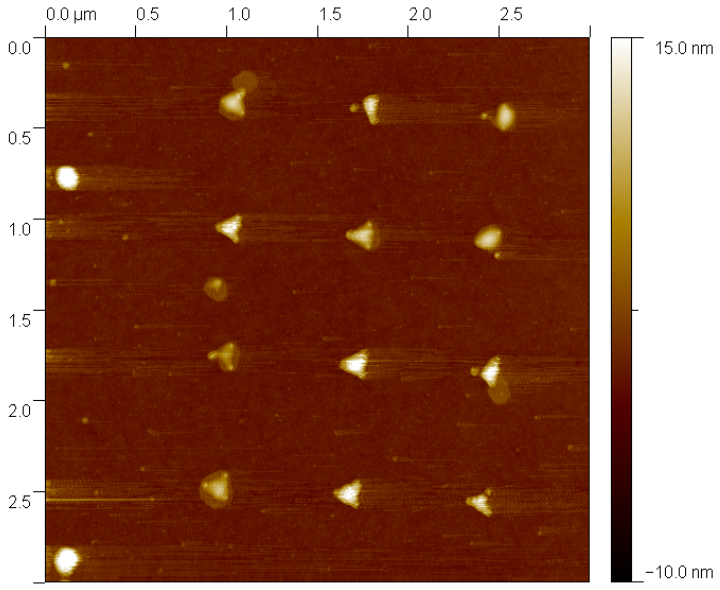

Figure 2.29: Dry AFM image of triangular DNA origami attached to clusters of nanodots arranged in trimers with 110 nm side. The nanodots are functionalized with ssDNA (30T) through direct thiolation; the origami are in TAE buffer with high NaCl concentration and they bind to the nanodots through DNA hybridization. The drying process results in salt accumulation on top of the origami.

As mentioned above, PEG passivation results in no binding at all, probably because of excessive repulsion. Passivation with a monolayer of hexamethyldisilazane (HMDS) results in the same absence of binding. As in the other binding schemes, in the case of the HMDS passivation the proper functioning of DNA hybridization to the dots is verified by functionalizing the dots with ssDNA through direct thiolation, hybridizing the complementary ssDNA functionalized with a fluorophore and verifying the binding with fluorescence microscopy (Fig. 2.9). Fluorescence imaging reveal that, as expected, ssDNA properly hybridizes to the functionalized nanodots, confirming that the repulsion exists only when a two dimensional nanostructure is involved, i.e. when there is a strong surface interaction.

2.7 Assembly of DNA-wrapped SWCNT segments

Carbon nanotube (CNT) segments dispersed in a water solution by ssDNA wrapping, with uniform length distribution and electronic properties, are attached to patterned nanodots properly functionalized to interact with functional groups at the ends of the CNT segments.

2.7.1 DNA-wrapped SWCNT segments

The starting material consists of short single wall carbon nanotube (SWCNT) segments wrapped in single stranded DNA [DNA sequence: (GT)20] and

dissolved in DI water (concentration ~40 μg/ml), obtained from M. Zheng at NIST. As previously demonstrated by Dr. Zheng and coworkers, DNA wrapping promotes efficient solvation of SWCNT in water [88]. The resulting solution is highly stable and it can be purified into separate batches of SWCNT segments with uniform length [89] and chirality [90]. This is done by size-exclusion chromatography (SEC) and ion exchange chromatography (IEX) respectively.

The SWCNT segment length distribution is quantified by tapping mode AFM and software analysis (ImageJ, Fig. 2.30). The average length and standard deviation of the CNT segments in the starting solution are found to be 148 ± 93 nm. (Comparable size distributions are reported by Zheng et. al. [88]). Using this value, the molar concentration of CNT segments is estimated to be about 70 nM.

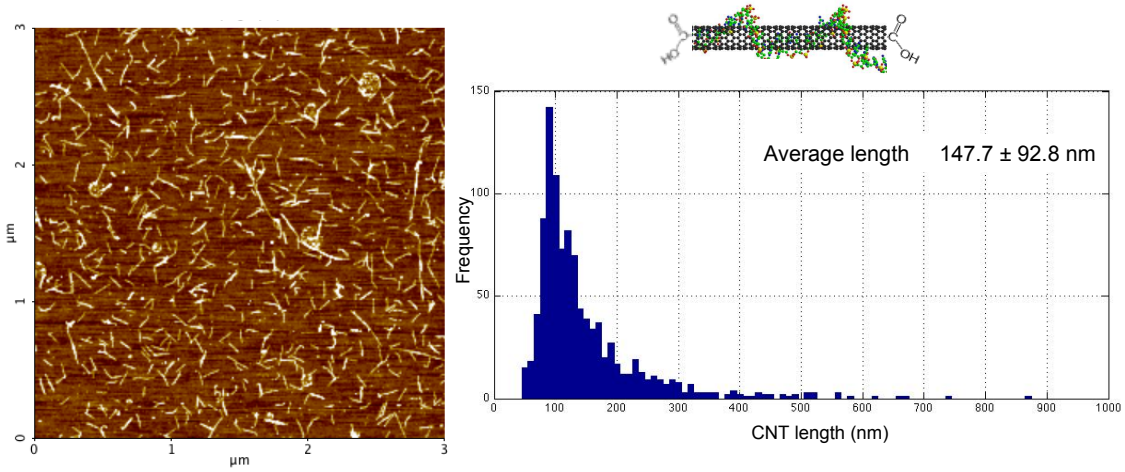

Figure 2.30: (Left) Tapping mode AFM image of DNA wrapped CNT segments deposited on SiO_2. (Right) Histogram of the length distribution of the CNT segments obtained with ImageJ. (Top) Schematics of a DNA wrapped CNT segment.

The structure of the DNA-wrapping is studied with high resolution AFM imaging (Fig. 2.31). Looking at the longitudinal profile of one CNT segment, periodic features, about 7 Å tall and with average distance ~25 nm, are observed. This is likely the ssDNA wrapping on the CNT.

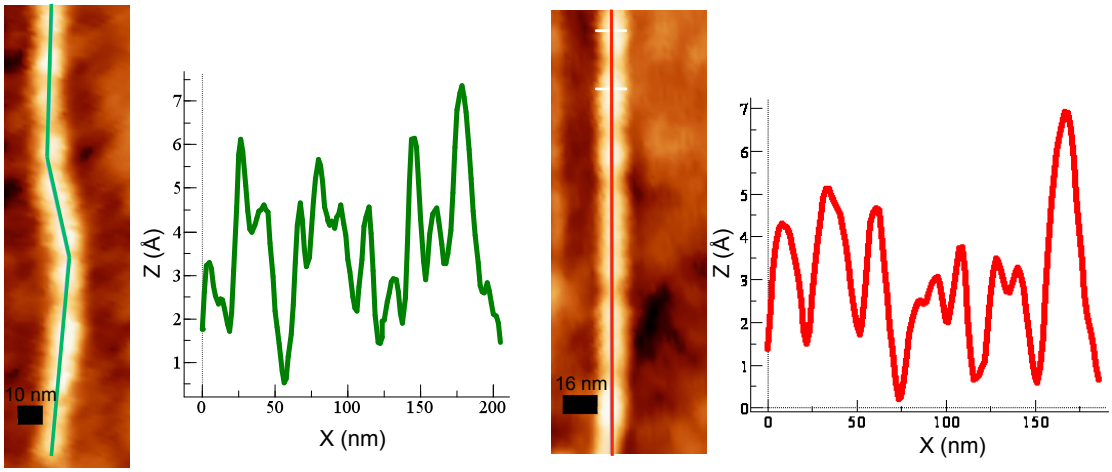

Figure 2.31: AFM images and relative profiles along the longitudinal direction of two DNA-wrapped CNT segments. The average height of the periodic features is ~7 Å, the average distance is ~25 nm. (Figure courtesy of G. Livshits and D. Porath, Hebrew University.)

The process to cut and solubilize SWCNT in DI water by ssDNA wrapping is believed to produce SWCNT segments with oxidized ends presenting carboxyl groups [152, 153]. We could verify that this is the case by reacting the carboxyl groups with amine groups to form a covalent amide bond (Fig. 2.32).

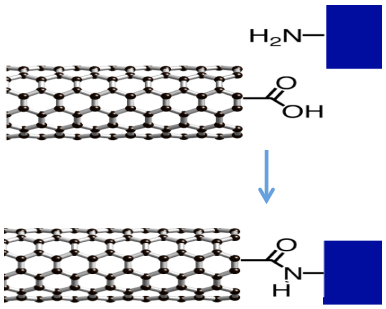

Figure 2.32: Schematic of reaction between the carboxyl groups on the ends of the CNT segments and amine molecules resulting in a covalent amide bond.

In a control experiment, the DNA-wrapped SWCNT solution, activated with EDC and sulfo-NHS in MES buffer, as described in section 2.7.3, is incubated on two samples with patterned Au features. One sample has the Au functionalized with amine groups, the other one is not functionalized. The final binding yield of SWCNT to the Au features is distinctly different, as seen in Fig. 2.33.

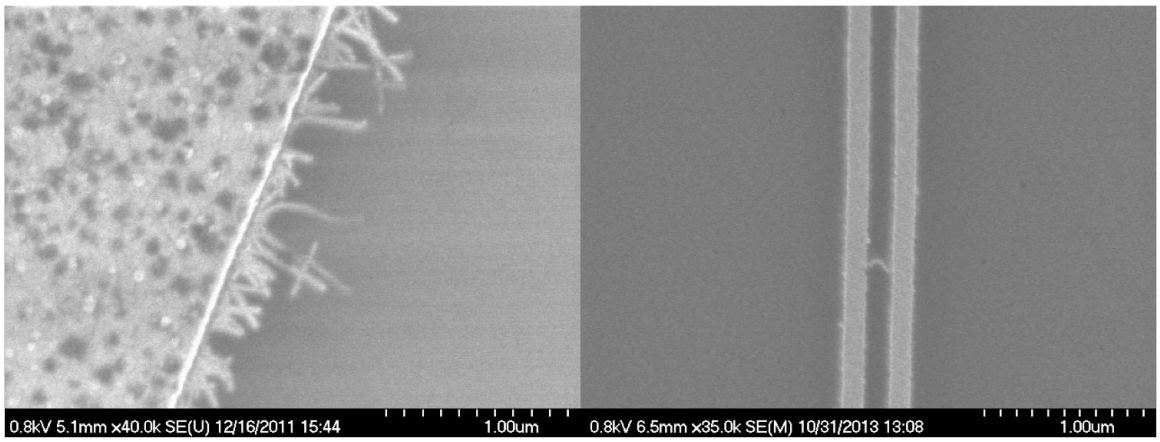

Figure 2.33: SEM images of DNA-wrapped CNT segments attached to Au features functionalized with amine molecules (left) or not functionalized with amine molecules (right).

Having confirmed that the SWCNT segments can be bound by their ends to amine-functionalized moieties, this reaction is employed to attach SWCNT segments to amine functionalized nanodots or ssDNA.

2.7.2 DNA-wrapped SWCNT segments assembly on nanodots

Nanodots are patterned in pairs or lines with spacing varying around the average length of the SWCNT segments (arrays with spacing 70 nm, 100 nm, 150 nm and 200 nm are fabricated).

Two binding strategies are developed:

- Covalent linkage between SWCNT segments and amine functionalized nanodots;
- Functionalization of SWCNT segments with ssDNA (ssDNA is functionalized with and amine group and thus reacts with the carboxyl groups at the SWCNT ends) and attachment to ssDNA functionalized nanodots through DNA hybridization.

Samples are characterized by tapping mode AFM revealing high binding yield for both approaches.

2.7.3 Covalent binding

The DNA-wrapped-CNT solution is mixed 1:1 to a solution consisting of 0.2 M MES buffer, 4 mM EDC and 10 mM sulfo-NHS. This solution is left to activate for 30 minutes at room temperature, during which the EDC and sulfo-NHS form an intermediate compound with the carboxyl groups on the CNT ends.

Substrates with nanodots arrays are functionalized with amine groups, as described in 2.3.2. The amine functionalized substrates are incubated with the SWCNT activated solution. During incubation the intermediate compound on the SWCNT ends reacts with the amine groups on the nanodots, resulting in a covalent bond. 8 μl of DNA-wrapped-CNT activated solution are deposited on each sample and let react overnight in a sealed 6 well plate with Kim wipe wet with DI water (to prevent the solution from evaporating).

The samples are then washed by dipping in DI water for 10 s and then in ethanol for 10 s. In both cases the amount of solution per sample is 10 ml. They are finally either gently blown dry with compressed nitrogen or air, or allowed to dry in air. Samples are imaged by tapping mode AFM with a Nanoscope IV microscope (Digital Instruments) with ultra-sharp 16 series (NSC 16, MikroMasch).

As visualized by AFM, this binding scheme results in 95% binding yield, i.e. 95% of the dots have at least one SWCNT segment attached, and 100% binding at the SWCNT ends, confirming that the binding occurs through an amine-carboxyl linkage (Fig. 2.34).

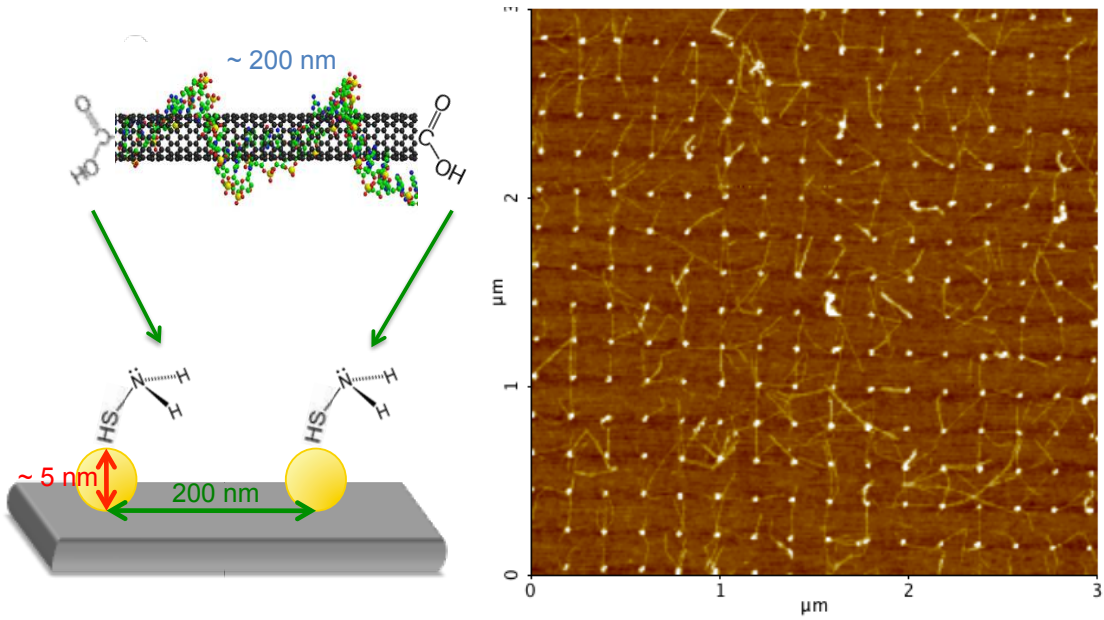

Figure 2.34: (Left) Schematic of DNA-wrapped CNT attachment to amine functionalized nanodots through a covalent bond. (Right) Tapping mode AFM image of DNA-wrapped CNT attachment to a grid of amine functionalized nanodots through a covalent bond. In this image, 95% of the dots have at least one SWCNT segment attached, and 100% of the binding is at the SWCNT ends, confirming that the binding happens through amine-carboxyl linkage. Bivalent binding is limited to a 20% yield.

When samples are blown dry, arrays of aligned SWCNT segments, parallel to the drying direction, are obtained, presumably as a result of capillary force drying (Fig. 2.35).

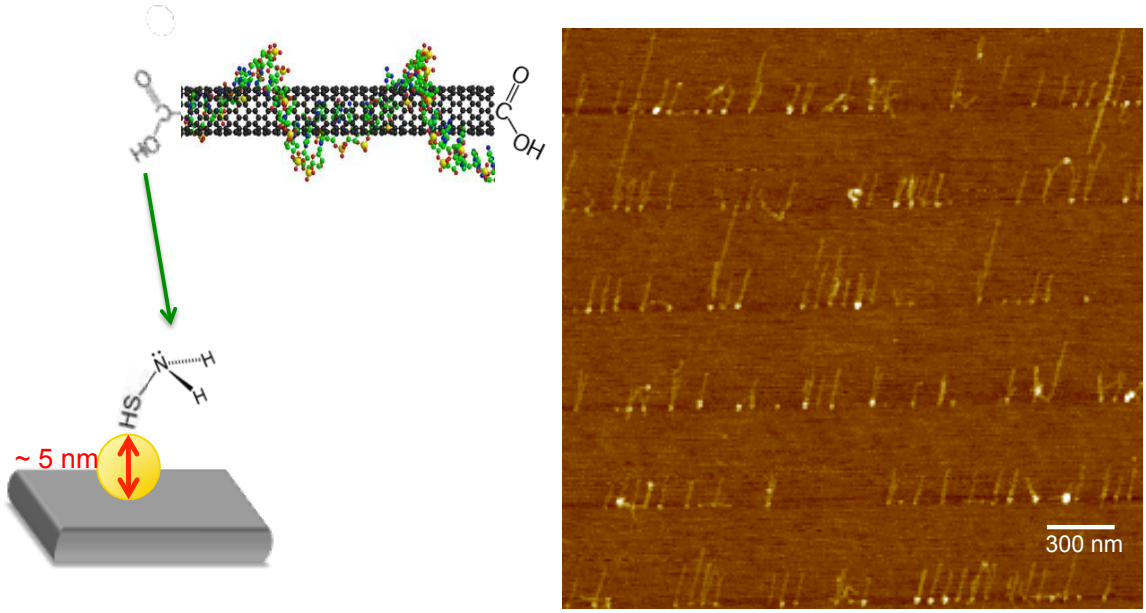

Figure 2.35: (Left) Schematic of DNA-wrapped CNT attachment to amine functionalized nanodots through a covalent bond. (Right) Tapping mode AFM image of DNA-wrapped CNT attachment to lines of amine functionalized nanodots (70 nm apart) through a covalent bond. In this image 95% of the dots have at least one SWCNT segment attached, and 100% of the binding is at the SWCNT ends, confirming that the binding happens through amine-carboxyl linkage. The CNT segments are aligned to one direction by capillary force drying.

In accordance to the thermodynamic model developed for the DFX, SWCNT assembly through covalent linkage (which is a high energy linkage) results in high yield unidirectional monovalent binding, but the bivalent binding is limited to a 20% yield (Fig. 2.32). In order to increase the yield of bivalent binding, a different approach is developed, in which the binding of the SWCNT segments takes place through DNA hybridization. In this case, the strength of the interaction can be modulated by changing the length of the complementary DNA strands.

2.7.4 Binding through DNA hybridization

In this approach, ssDNA is attached to the SWCNT ends and the nanodots are functionalized with the complementary ssDNA.

The starting DNA-wrapped SWCNT solution is activated by mixing it, 1:1 by volume, with a solution consisting of 0.2 M MES buffer (pH 6), 4 mM EDC and 10 mM sulfo-NHS. The SWCNTs sit in this solution for 30 minutes at room temperature, during which the EDC and sulfo-NHS form an intermediate compound with the carboxyl groups on the CNT ends. Following activation, a DPBS solution of amine-functionalized DNA is added. This DNA strand consists in a 10 base pair double stranded portion, with an amine group on the 3' side, and a single stranded poly-adenine portion on the opposite side (5' – 10 A or 30 A – CGT C/3AmMO/- 3' hybridized to 5' – GAC G – 3'). The complementary strands, forming the double stranded portion, are hybridized prior to attachment to the SWCNT by mixing an equal molar content in DPBS to get a concentration of 10 μM. The solution is heated to 65 °C, kept at that temperature for one hour and then slowly cooled down to room temperature. The dsDNA portion serves as a short spacer, separating the ssDNA sticky-end from the SWCNT, in order to prevent unwanted interactions with the body of the tube and thus increasing the chances of hybridization with the nanodots on the substrate, which are functionalized with complementary ssDNA. The amine-DNA concentration is 167 nM, making it sufficiently likely that both ends of all SWCNT segments would be attached to at least one strand. The mixture of activated SWCNT segments and amine-functionalized DNA is left to react

overnight at room temperature. Any unreacted DNA strands are removed by centrifugation in Millipore Amicon 100K tubes (the residual concentration of dsDNA after purification is estimated to be less than 0.5 nM). During purification the buffer is exchanged to DPBS 1X.

Substrates with nanodots arrays are functionalized with ssDNA (poly-thymines of different length) as described in 2.3.2. The functionalized substrates are incubated with 10 μl of the purified ssDNA end-functionalized SWCNT solution in 1X DPBS with ~ 15 mM $MgCl_2$ to improve hybridization. Samples are incubated overnight in a sealed 6 well plate with Kim wipe wet with DI water (to prevent the solution from evaporating).

After the reaction, each sample is dipped for 10 s in 10 ml of a mixture of ethanol (50%) and DI water (50%). The sample is then transferred to a well containing 10 ml of a 80% ethanol and 20% DI water solution, where it is allowed to sit for 50 min. It is finally dipped in pure ethanol and then dried in air. Samples are imaged by tapping mode AFM with a Nanoscope IV microscope (Digital Instruments) with ultra-sharp 16 series (NSC 16, MikroMasch).

As visualized by AFM, this binding scheme results in 80% binding yield, i.e. 80% of the dots have at least one SWCNT segment attached, and 100% binding at the SWCNT ends (Fig. 2.35). It has been thus verified that there is no interaction between the ssDNA wrapping around the tubes and the ssDNA on the nanodots. Consistent with the thermodynamic model developed for the

DFX, SWCNT assembly through DNA hybridization results in a much higher yield of bivalent binding, compared to the attachment based on covalent bonds.

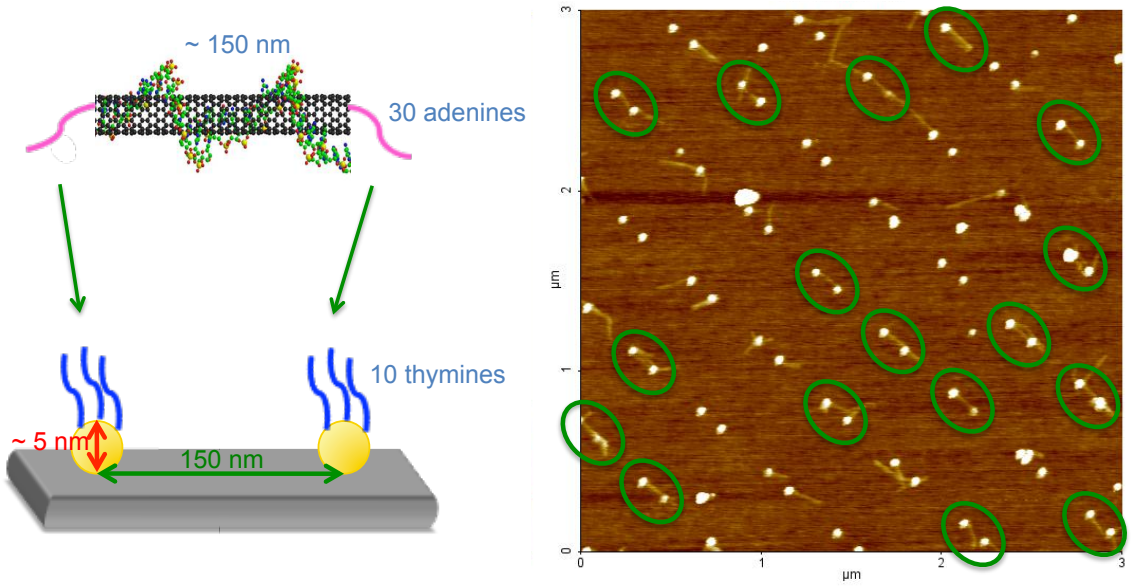

Figure 2.36: (Left) Schematic of DNA-wrapped CNT with ends functionalized with ssDNA (30A) attachment to ssDNA (10T) functionalized nanodots through DNA hybridization. (Right) Tapping mode AFM image of DNA-wrapped CNT attachment to pairs of 10T functionalized nanodots through DNA hybridization. In this image 80% of the dots have at least one SWCNT segment attached, and 100% of the binding is at the SWCNT ends. The yield of bivalent binding is 60% while the yield of monovalent binding is 45%.

Substrates are functionalized with poly-thymines of different length: 3T, 10T, 19T and 30T. Also, SWCNT are functionalized with poly-adenines of different length: 10A and 30A. The best result, i.e. the highest yield of bivalent binding, is obtained for 30 A functionalized SWCNT hybridizing to 10T. In this case the AFM images reveal a yield of bivalent binding as high as 60%, which surpassed the monovalent binding yield that was found to be now only 45% (Fig. 2.35). CNT segments functionalized with 10A do not give high binding yield.

2.8 Discussion

The polyvalent binding inspired approach for directed assembly of nanostructures, from solution to ordered arrays on a surface, described in this chapter demonstrates the capability of controlling nanostructure deposition with sub-10 nm resolution.

The key variables governing the binding interaction are:

- The nanodots size
- The type of nanodots functionalization
- The type of nanostructures binding to the nanodots
- The chemistry of binding
- The interaction with the surface surrounding the nanodots

The small dimension of the patterned nanodots results in the binding of a limited number of nanostructures. More specifically, the average number of nanostructures binding to each nanodot depends on the nanodots size and on the chemistry of binding. For binding of 1D nanostructures (DFX or DNA-wrapped CNT segments) through direct thiolation and DNA hybridization it is observed that, for nanodots bigger than 10 nm, multiple nanostructure binding to one nanodot is the most probable event. When the diameter of the dots is about 5 nm the average number of 1D nanostructures binding to a single nanodot is about one. The DFX nanostructure has slightly higher binding yield than DNA-wrapped CNT segments. This is probably due to some repulsion to the CNT portions that are not completely covered in DNA. When comparing the

binding of DNA-wrapped CNT through a covalent amide bond or through DNA hybridization, the first binding chemistry results in a higher and more controllable binding yield: for nanodots with diameter about 5 nm binding of one CNT segment to one nanodot is consistently observed. Possible reasons for this difference are the specific binding kinetics, and the fact that the DNA hybridization approach involves an extra reaction and purification steps (to bind the ssDNA to the CNT ends), which inevitably results in a decrease of CNT population available for binding to the nanodots. More details about the binding yield of amine functionalized DNA to SWCNT segments are found in chapter 4.

The biotin/streptavidin approach involves the formation of a mix SAM of biotin and PEG, so that the number of biotin molecules available for streptavidin binding is lower that what would be sterically allowed; the streptavidin size further reduces the final number of sites for binding. Indeed in this case single DNA molecules binding is observed for nanodots larger than 10 nm.

The lowest binding yield is observed for DNA origami, in which, even for nanodots 10 nm or bigger, less than one origami binds to each nanodot, on average. This might be due to the lower concentration of the starting solution, which reduces the binding probability. It is indeed observed, for both DFX and DNA-wrapped CNT, that the concentration of the starting solution has a significant impact on the final binding yield. When the concentration is too low almost no binding is observed. On the other hand, if the concentration is too high the average number of nanostructures binding to one nanodot increases, and non-specific binding (random physisorption to the surface) is observed as

well. While for DFX and DNA-wrapped CNT it is possible to adjust the dot size, solution concentration and strength of the binding interaction to study the occurrence of bivalent binding, in the case of DNA origami the interaction between the origami and surface of the sample is found to dominate over the interaction between the molecules on the origami corners and the functionalized nanodots, consequently overcoming the polyvalent interaction.

The difference in behavior between the DFX nanostructure and DNA-wrapped CNT segments or DNA origami can be understood in term of the thermodynamics of binding, when looking at the same binding interaction, i.e. DNA hybridization. There are two main differences between DNA-wrapped CNTs and the DFX:

- The ends of the DFX molecules possess the 20A sticky ends with higher certainty than the CNTs. The reason is that the DFX nanostructure is directly synthesized with the sticky ends, so as long as the nanostructure is properly formed, the sticky ends are in place. In the case of DNA-wrapped CNT segments, the ssDNA is added through a second reaction and, while it's been demonstrated that the reaction is successful, the yield is not precisely known (although experiments detailed in chapter 4 suggest that the binding yield is quite high).
- While the "body" of the DFX is fully made of DNA, in the case of DNA-wrapped CNT there is an alternation of DNA and CNT areas (the wrapping was found to have ~25 nm periodicity; being ssDNA about 1 nm in size, the CNT happens to be more exposed than covered). The DFX

thus possesses of a fully hydrophilic surface, while the DNA-wrapped CNTs show an alternation of hydrophilic and hydrophobic areas. This difference in surface chemistry probably results in different interactions with the samples surface. The DFX is found to deposit with higher density as the surface hydrophilicity increases. No deposition is observed on hydrophobically coated surfaces (PEG of HMDS). (The same is true for DNA origami). On the other hand, DNA-wrapped CNT segments are found to barely deposit on highly hydrophilic surfaces (mica in high ion concentration conditions or SiO_2 treated with a high power oxygen plasma) or on highly hydrophobic conditions (PEG or HMDS coatings of excellent quality; when the coatings are imperfect, for example because of short coating times, CNT physisorption is observed). The thermodynamic model developed for the DFX did not account for the interaction between the nanostructure and the surface. To first approximation this is perfectly reasonable because, when comparing binding through DNA hybridization of strands with different length, the surface interaction is the same and it would just add a constant to all the calculations. When looking at the difference between the DFX and the CNT though, the surface interaction becomes more critical. For the hydrophilic SiO_2 surface adopted in the experiments involving nanodots functionalization by direct thiolation and binding through DNA hybridization, the DFX interaction is presumably less repulsive than the CNT interaction. This is indeed reflected in the slightly lower yield of binding observed for DNA-wrapped CNT segments.

The effect of the surface can be accounted for by adding an extra enthalpic term to the free energy of binding ($\Delta G°$). In the case of the DFX this term will be negative, because the surface is hydrophilic and the reaction is thus attractive. For the DNA-wrapped CNT segments it will be less negative or maybe even slightly positive, while for DNA origami it will be negative, grater in absolute value than for the DFX and proportional to the origami area. A precise estimation of the surface charges (on the sample surface and on the nanostructures) is needed for a quantitative calculation of this extra enthalpy term. There are many factors influencing this charge distribution: the sample surface state after all the processing (initial aged piranha and oxygen plasma, immersion in various buffer, DI water and ethanol solution, and air exposure) the density of hydrophilic/hydrophobic groups on the nanostructures surface and how the ions in the buffer solution mediate the interaction between the sample surface and the nanostructures.

The strong interactions that these nanostructures display with the surface are further explored and exploited in Chapter 3.

A further strength of the approach described in this chapter is that the patterning technique adopted to fabricate the nanodots is relatively simple, low cost, and high throughput, because based on nanoimprint lithography. All the steps of the process (nanodot patterning, nanodot functionalization and nanostructures assembly) are parallel. They thus allow the production of large arrays of nanostructures (up to centimeters) with nanometer resolution and

complete flexibility over the patterning layout (down to about 20 nm) economically in both money and time.

Chapter 3

Directed assembly on patterned high surface energy regions

3.1 Introduction

The techniques described in this chapter consist of patterning regions with high surface energy on a background of low surface energy, formed by passivating the surface with a low energy coating. These regions are designed to match the size and shape of nanostructures in solution and thereby precisely drive the selective binding of the nanostructures. Patterning is done using nanoimprint lithography or e-beam lithography. The nanostructures studied in this work are DNA origami and DNA-wrapped SWCNT segments.

Lithographically directed assembly of SWCNT allows high yield fabrication of CNT field effect transistors (FETs) by precise aligned patterning of electrodes.

3.2 Directed assembly of DNA origami

A nanoimprint lithography-based process is developed to create chemically patterned templates, rendering them capable of selectively binding DNA origami [154]. This method is based on the work of Kershner et al. [155], in which electron beam lithography is used to pattern hydrophilic areas that matched the size and shape of DNA origami triangles.

In this work, Hexamethyldisilazane (HMDS) is used as a passivating layer on silicon dioxide (SiO_2) substrates, which prevents DNA attachment. Hydrophilic areas, patterned by nanoimprint lithography designed to match the size and shape of the origami, are formed by selective removal of the HMDS by mean of an oxygen plasma etch (Fig 3.1). DNA origami of different shapes are bound to these regions in a buffer solution with a high concentration of magnesium ions (Mg^{2+}) which makes the origami highly reactive with the hydrophilic SiO_2 areas.

The use of nanoimprint lithography (NIL), a low cost, high throughput patterning technique, enables high precision positioning and orientation of DNA nanostructures on a surface over large areas.

3.2.1 Fabrication of hydrophilic areas

Samples are produced by a process consisting of two steps. In the first step, NIL molds are fabricated by electron beam lithography using the high resolution negative tone resist hydrogen silsesquioxane (HSQ). In the second step, the

molds are replicated by thermal NIL. A scheme of the fabrication process is shown in Fig. 3.1.

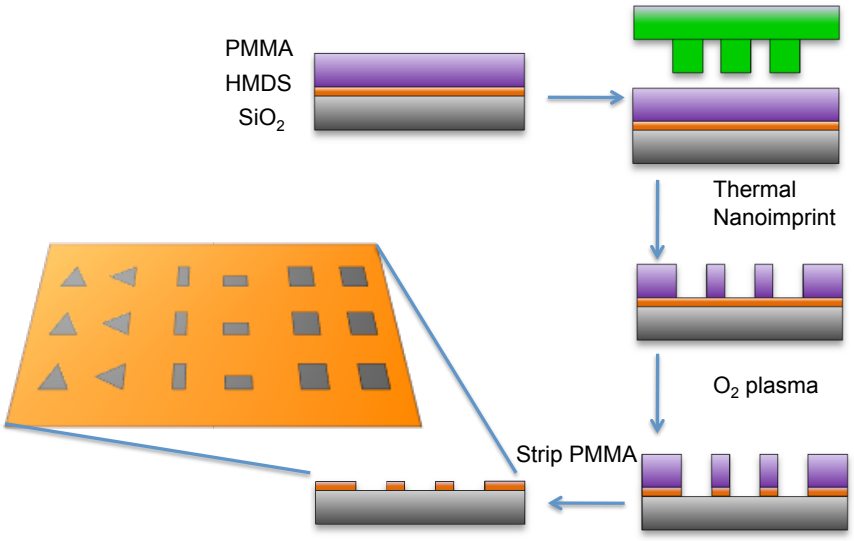

Figure 3.1: Scheme of the samples preparation process. Arrays of hydrophilic features with different shape and orientation are patterned by nanoimprint lithography on HMDS passivated substrates.

A. Mold fabrication

Hydrogen silsesquioxane (Dow Corning XR-1541 e-beam resist in MIBK) is spin cast on silicon wafers, to yield a 100 nm-thick layer. No post-apply bake is used in order to minimize cross-linking. E-beam patterning is done using a scanning electron microscope (FEI XL 30 Sirion) equipped with a Nabity NPGS pattern generator. Geometric shapes (primarily squares, rectangles, and triangles) with sizes in the 100 nm range, matching the dimensions of specific DNA origami

motifs, are written. The HSQ is developed for 6 min in Microposit MF CD-26W developer at room temperature, followed by a DI water and isopropyl alcohol rinse. The molds are then exposed to an oxygen plasma for 1 minute (Diener Plasma Etch System) and coated with a fluorosilane anti-adhesion layer deposited in a vapor phase coater (Nanonex Ultra-100). The NIL molds are imaged with a scanning electron microscope (Hitachi 4700) before deposition of the anti-adhesion coating (Fig. 3.2). The feature height is measured by AFM.

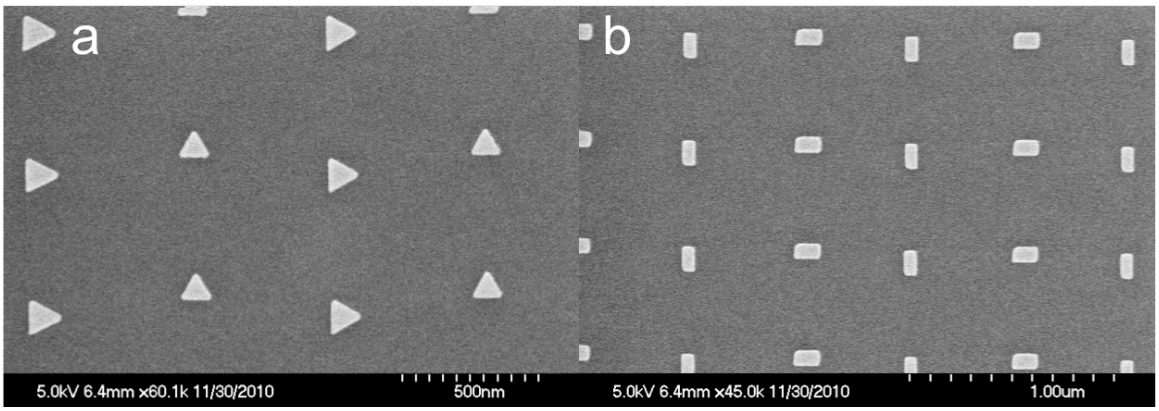

Figure 3.2: SEM image of the HSQ features on the molds. Different shapes - triangles (a) and rectangles (b) are patterned on the same mold. The features height is about 100 nm. The apparent difference between shapes with different orientations is possibly due to beam blanking asymmetry during the e-beam write.

B. Substrate fabrication

The substrates are silicon wafers with a 300-nm-thick thermal oxide. The wafers are initially cleaned by rinsing with acetone and isopropyl alcohol,

followed by exposure to an oxygen plasma for 1 minute (Diener Plasma Etch System). A monolayer of hexamethyldisilazane (HMDS, Alfa Aesar) is deposited by exposing the cleaned wafers (preheated at 185 °C on a hot plate) to HMDS vapor for 10 minutes in a glass chamber. Directly after HMDS deposition the wafers are coated with 100 nm of polymethylmethacrylate (PMMA, 950 K, 2% in anisole, Micro Resist Technology) and soft-baked for 5 minutes at 185 °C. Although the molds are treated with an anti-adhesion layer to facilitate separation from the imprinted resist, an additional step is taken to further reduce the PMMA surface energy. This is necessary because the adhesion between the PMMA and the HMDS is fairly poor, and thus the PMMA may delaminate from the substrate during the mold separation step. Therefore, the PMMA coated samples are exposed to a fluorocarbon-based plasma treatment, rendering them highly hydrophobic[156, 157]. PMMA surface fluorination is done in an Oxford Plasma Lab 80 Plus etch system using C_4F_8 gas as source material. Thermal NIL is then performed in a Nanonex BX-200 system, at 200 °C and 500 psi for 5 minutes. The residual layer of PMMA and the HMDS are removed from the imprinted features by exposing the sample to an oxygen plasma for 30 seconds (Diener Plasma Etch System). The remaining PMMA is then stripped by sonication (Branson 3510) in a N-methylpyrrolidone (NMP, Sigma Aldrich) bath for 30 minutes followed by acetone and ethanol rinses. (Sonication in acetone shows incomplete PMMA removal, confirming results of previous studies[107]).

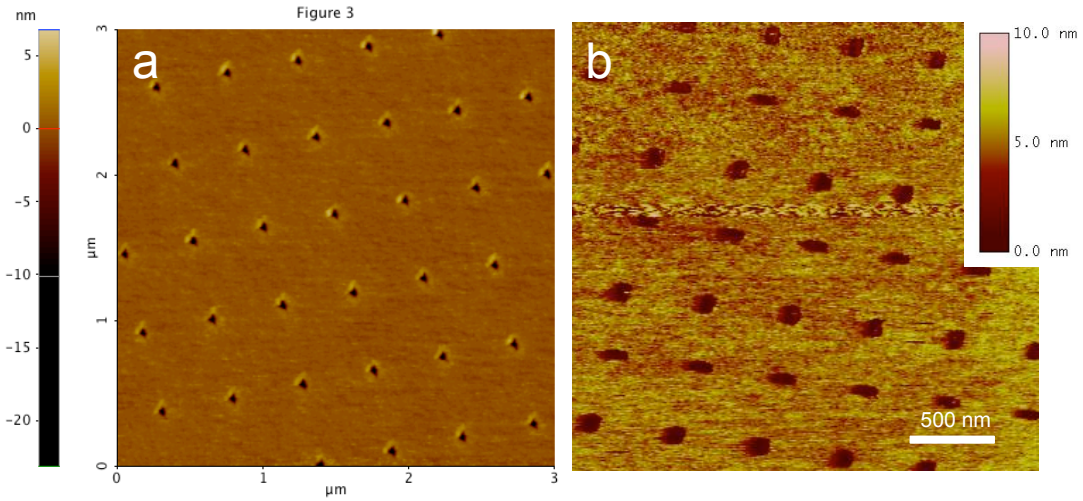

Figure 3.3: (a) Topography AFM image in dry conditions of imprinted 950 K PMMA after 30 s oxygen plasma. The measured features depth is smaller than expected (it is shown to be 25 nm instead of the expected 100 nm), but this is the result of the AFM tip size being bigger than the size of the features, making it unable to reach the bottom of the imprinted features. (b) Topography AFM image under liquid conditions of the HMDS template. The thickness of the HMDS layer is probably increased by imaging in liquid.

3.2.2 Origami synthesis

DNA origami is formed using the recipe first described by Rothemund [158]. M13 viral DNA and all the staple strands are mixed together at a 1:10 ratio, in a 1X TAE buffer solution containing 40 mM Tris-HCl, 20 mM acetic acid, 2.5 mM EDTA, and 12.5 mM magnesium acetate. The solution pH is 8.0. The final concentration of M13mp18 DNA genome in the solution was 10 nM. The solution is cooled from 90 °C to 16 °C over 1.5 hours. The DNA origami solution is then purified to remove the excess DNA helper strands using 100 kDa MWCO centrifuge filters (MicroconYM-100, Millipore, Billerica, MA). In a single filter

vial, 50–100 μl of origami solution is washed three times with ~ 450 μl of 1X TAE buffer with 125 mM Mg^{2+}, spinning down to ~ 50 μl each time. The origami solution is stored at 4 °C until use.

3.2.3 DNA origami binding and imaging

About 10 μl of DNA origami solution is deposited on the substrate patterned area. Samples are incubated in a humidified chamber for 3 hours and imaged directly after incubation using an AFM liquid imaging cell (Veeco IV). 20 μl of 1X TAE buffer with 125 mM $MgCl_2$ are added to the AFM tip (Veeco SNL-10) prior to approaching the sample. In order to image the samples by AFM under dry conditions (Park System XE-100, tips: Mikro Mash NSC16/AIBS), a solvent exchange is performed prior to drying [108]. This is necessary in order to reduce precipitation of magnesium salts from the buffer. Each buffered sample is dipped for 10 seconds in 4 ml of a mixture of ethanol (50%) and DI water (50%). It is then transferred to a well containing 4 ml of a 90% ethanol 10% DI water solution, where it is allowed to sit for 50 minutes. The samples are then air dried.

3.2.4 Results and discussion

A robust NIL process has the following requirements. (1) The aspect ratio of the features on the mold should not be too high to prevent detaching or braking

during the imprint process. (2) The resist layer should not be much thicker than the mold feature height. This is necessary to limit the thickness of the post-imprint residual layer. A thin residual layer is desirable to avoid distortions of the features shape during the oxygen plasma descum. (3) A low viscosity resist is desirable in order to facilitate flow during the imprint. For thermal NIL, a low molecular weight resist also aids in its removal after patterning. This is particularly critical for the process used in this work, as the substrate must be free of any resist residue in order for the selective origami binding to be successful. The use of low molecular weight PMMA (M_W = 15 and 35 K) is attempted for the imprint process, but good adhesion to the HMDS-coated substrate is difficult to achieve due to the hydrophobicity of the HMDS. It is only with higher molecular weights (M_W = 495 and 950 K) that a repeatable coating is achieved, although if the time of incubation in the HMDS vapor is longer than 10 minutes and/or if the spinning speed and acceleration are higher than 3000 rpm and 500 rpm/s a repeatable, uniform PMMA layer formation cannot be obtained. Operating within these parameters yields uniform PMMA layers with thicknesses of 60 nm (495 K) and 100 nm (950 K). The thickness is measured with a Filmetrics F20 thin-film analyzer after the soft bake. 950 K PMMA is chosen because, on average, the spinning process is more reliable. Even with this higher M_W PMMA, no residual PMMA is found on the substrates after sonication in NMP. Although the 950 K PMMA yields uniform resist films, some resist adhering to the mold following separation after the imprint is occasionally observed. This is attributed to the hydrophobicity of the HMDS, which likely results in the unusual situation in which the adhesive

force between the mold and the resist exceeds that of the resist to the substrate. The quick treatment of the PMMA with a fluorocarbon plasma helps to overcome this issue [156, 157]. Figure 3.3 shows AFM images of substrates after imprinting and after removal of the residual resist layer by O_2 RIE and resist strip sonicating in NMP. Following this, a drop of buffer solution (about 10 μl) containing the DNA origami structures is placed on the samples patterned area. Figures 3.4 and 3.5 show topography and phase AFM images taken under liquid conditions of samples after incubation with DNA origami. The AFM imaging under liquid conditions is performed while maintaining a 125 mM concentration of Mg ions in the buffer solution, enabling a strong interaction of the origami with the SiO_2 and preventing their removal during imaging. The origami can be seen to adhere to the pattern areas with very high fidelity, with an origami raft located at every position in each array. Orientation control appears to be quite high as well, although the quality of the liquid AFM scans prevents a true quantitative assessment.

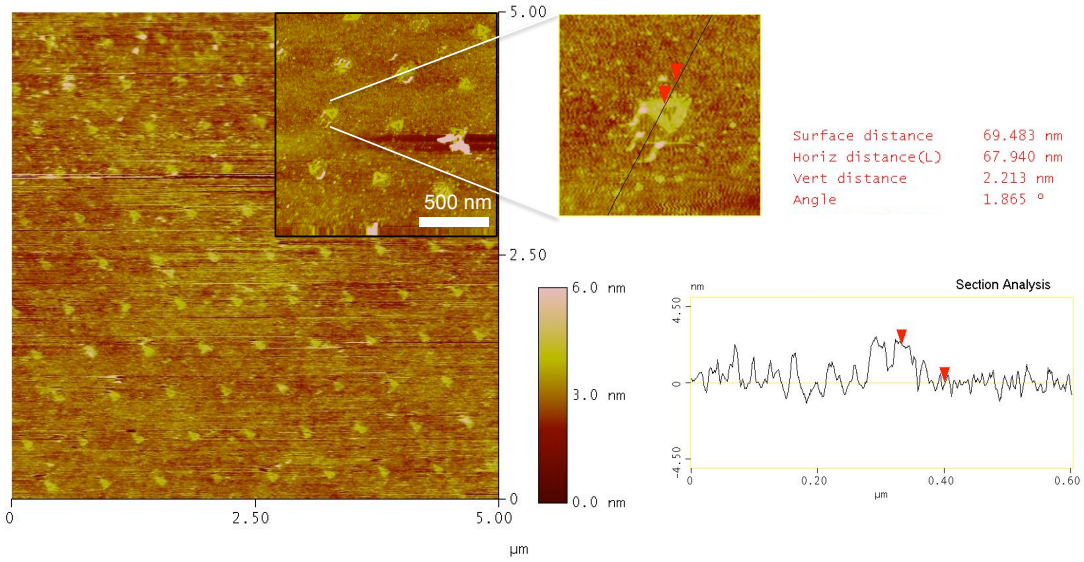

Figure 3.4: Topography AFM image under liquid conditions of the HMDS template with attached triangular DNA origami. All binding sites are occupied and no nonspecific binding is observed. The height profile across a DNA origami triangle corresponds to the thickness of a single DNA duplex (~2 nm).

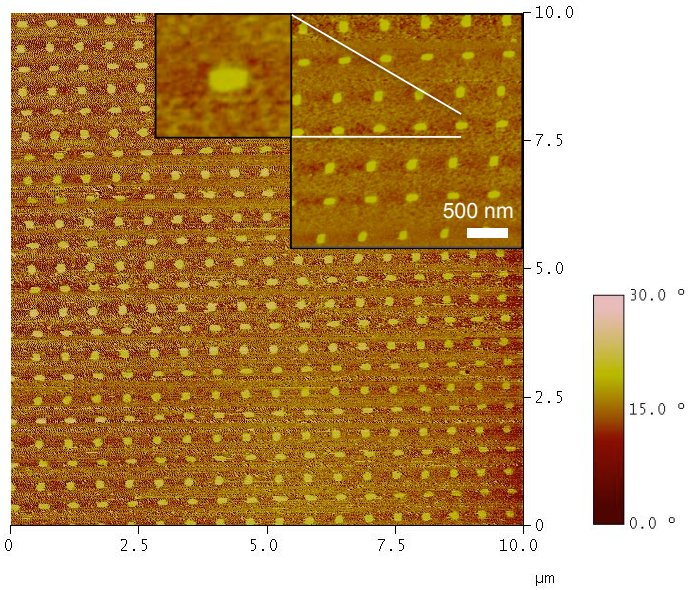

Figure 3.5: Phase AFM image under liquid conditions of the HMDS template with attached rectangular DNA origami. The signal indicates the contrast between the DNA origami soft surface and the substrate hard surface.

A solvent exchange process (described above) is used to dry the samples for viewing in a conventional AFM, however, the concentrated salt solution results in the presence of precipitates on the surface, which are not completely removed in the drying process (Fig. 3.6). In addition, it is observed that increasing the incubation time beyond 3 hours causes a progressive deterioration of the HMDS layer, which produces an increase of the number of nonspecific binding events.

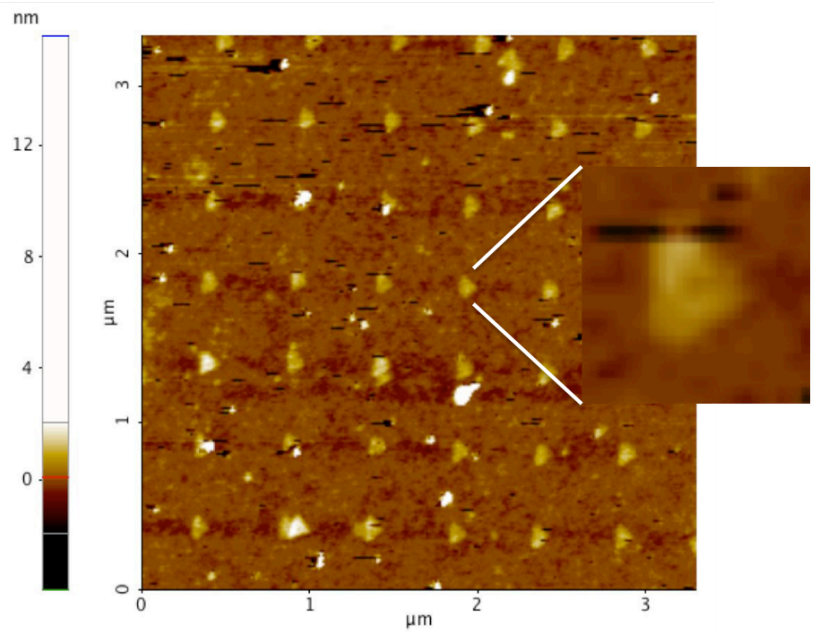

Figure 3.6: AFM image under dry conditions of the HMDS template with attached triangular DNA origami. Some defects are visible due to the presence of salt precipitates.

This nanoimprint lithography-based process can be extended to the attachment of smaller functional nanomaterials, such as nanoparticles, quantum dots, carbon nanotubes or semiconducting nanowires, on the origami scaffolds,

enabling the formation of dense, ordered arrays of functional nano-objects and thus enabling the construction of working devices and their connection into circuits. Following the work by Hung et al., we attempted to apply our NIL-based surface assembly process to origami with attached nanoparticles and quantum dots [33] but we were unable to achieve a clean and ordered assembly.

3.3 Directed assembly of DNA-wrapped SWCNT segments

In this section, the process described above to control the placement of DNA origami by patterning the surface energy of the substrate, is adapted to the organization of DNA wrapped SWCNT on a surfaces. The SiO_2 surface is now not passivated with HMDS, as above, but a polyethylene-glycol (PEG) monolayer is used instead, which effectively prevents DNA-wrapped SWCNT physisorption. E-beam lithography is used to pattern thin lines (10 nm wide) in PMMA. The patterned resist works as a mask to selectively remove the PEG with an oxygen plasma, resulting in the formation of hydrophilic thin lines (Fig. 3.7). DNA-wrapped SWCNT segments are dissolved in a buffer solution with high concentration of magnesium ions, which makes them highly hydrophilic and results in their selective binding to the patterned lines.

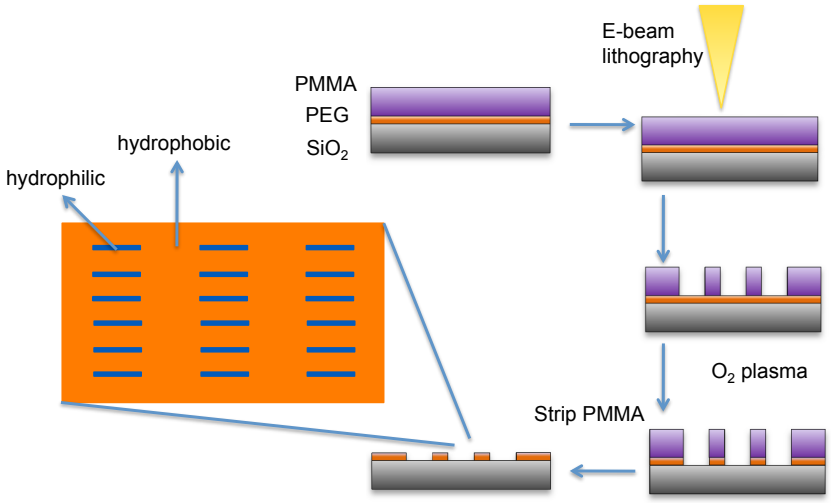

Figure 3.7: Scheme of the patterning of hydrophilic lines on PEG passivated substrates by e-beam lithography and reactive ion etching (RIE).

The lithographically-directed deposition of SWCNT segments on a surface allows high-resolution aligned patterning of electrodes, facilitating (in principle) the high yield fabrication of nanoscaled SWCNT FETs. E-beam lithography is preferred over NIL in this case because of the overlay requirements in aligning the SWCNTs and the electrodes and because of the patterning flexibility.

The choice of PEG is dictated by the good passivation against DNA-wrapped CNT physisorption and because it allows the simultaneous passivation of SiO_2 and of Au features, enabling the deposition of the SWCNT segments underneath or on top of patterned electrodes.

3.3.1 Fabrication of hydrophilic areas

Samples with silicon oxide surfaces and, in some cases pre-patterned Au electrodes, are passivated with a layer of polyethylene glycol (PEG).

Substrates are first cleaned in an aged (1.5 h old) piranha solution (3:1 H_2SO_4 : H_2O_2) followed by a de-ionized (DI) water rinse, an ethanol rinse and blown dry with an inert gas (Ar or N_2). The dry samples are put in an UV–ozone cleaner for 5 min at 18 W, then immediately incubated in a solution of PEG-silane (2-[methoxy(polyethyleneoxy)propyl]trimethoxysilane, M_w = 460-590, Gelest) in anhydrous toluene (300 μl of PEG-silane in 30 ml of toluene), with 100 μM PEG-thiol ($HS–(CH_2)_{11}–(C_2H_6O_2)_3–OH$, Prochemia) if the substrates had pre-patterned electrodes (PEG-silane passivates the SiO_2 surface while PEG-thiol passivates Au features). Acetic acid (30 μl for 30ml of toluene-PEG solution) is added as a catalyst to the solution directly before immersing the samples. Samples are incubated for 48 hours to one week to allow a uniform PEG layer to form so that it then successfully prevents nonspecific binding of DNA-wrapped SWCNTs. Better passivation is observed on samples passivated for one week.

After passivation samples are rinsed with acetone and ethanol and blown dry with Ar. They are coated with 60 nm of PMMA (495 K, 2% in anisole, Microchem) and soft-baked for at least 30 minutes at 170 °C before being patterned by e-beam (Nanobeam nB4 electron beam lithography system). The pattern consists of lines 200 nm long and 10 nm, 20 nm, 30 nm and 40 nm

thick (Fig. 3.8). The width is varied in order to find the conditions to maximize single SWCNT binding yield; 10 nm-wide lines yield the best results.

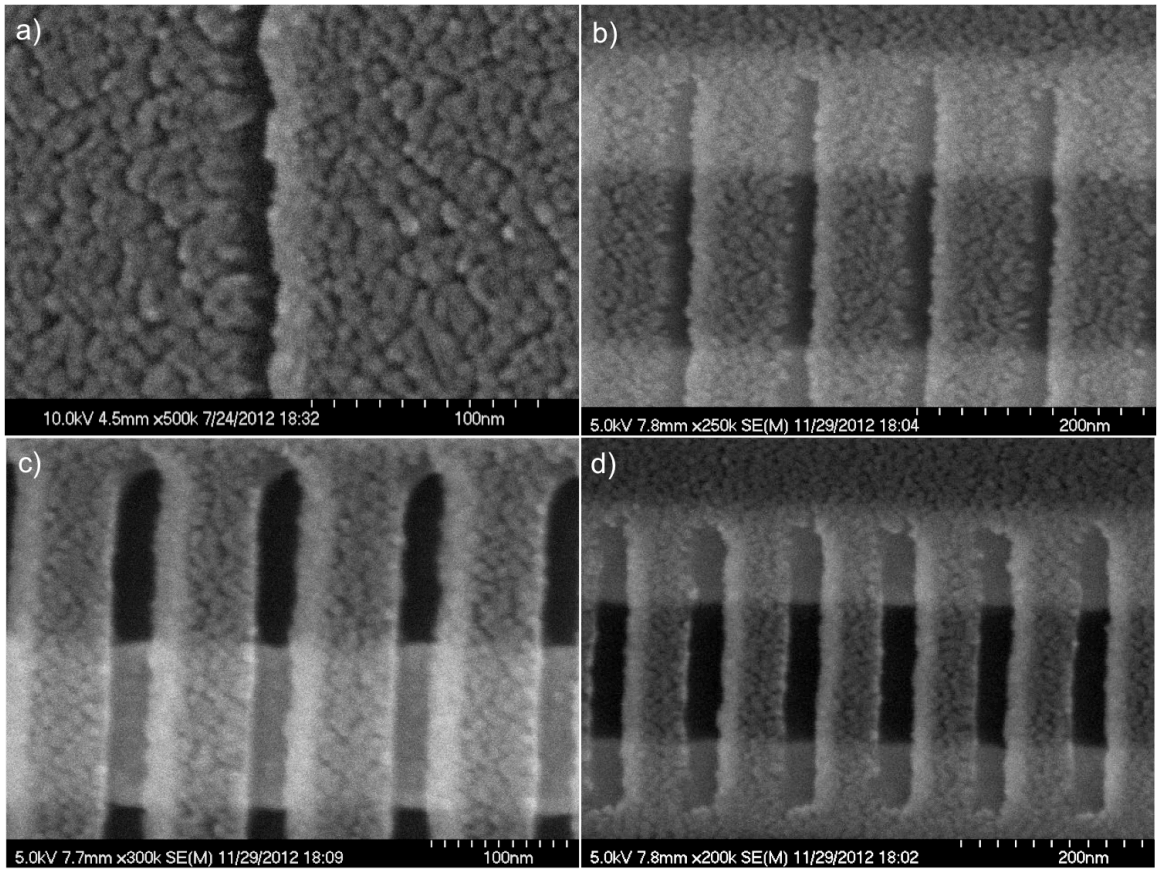

Figure 3.8: SEM images of patterned lines on PMMA. The width of the lines is (a) 10 nm, (b) 20 nm, (c) 30 nm and (d) 40 nm. A 10 nm thick Ti layer was e-beam evaporated at a 30° angle for imaging purposes. Au electrodes are visible underneath.

Development is done for 45 seconds in a 3:1 mixture of isopropyl alcohol (IPA) and MIBK kept at 4 °C with ultrasonic agitation (Branson 3510) and then for an additional 15 seconds in IPA at 4 °C with ultrasonication. Samples are blown

dry with nitrogen and the PEG is removed from the exposed lines by mean of a 24 seconds long oxygen plasma (Diener Plasma Etch System). The remaining PMMA is then stripped by sonication (Branson 3510) in a N-methylpyrrolidone (NMP, Sigma Aldrich) bath for 30 minutes followed by acetone and ethanol rinses.

3.3.2 DNA-wrapped SWCNT binding and imaging

Three solutions of SWCNT segments wrapped in ssDNA and dissolved in DI water are used for the assembly. All solutions are obtained from M. Zheng at NIST. One solution consists of mixed chirality SWCNT (concentration ~40 μg/ml, calculated from the E11 optical transition). Another other one is (6,5) enriched [90], thus prevalently made of semiconducting SWCNT (concentration ~6 μg/ml, calculated from the E11 optical transition). The third solution is made of a mixture of (5,5) and (6,6) metallic SWCNT[159] (concentration ~29 μg/ml, calculated from the E11 optical transition). In this last case the nanotubes are separated in a water-polymer two phases system, so that the final solution of metallic SWCNTs contains ~20 wt% of polyacrylamide and ~ 2 wt% of polyethylene glycol. The SWCNT solutions had undergone some length purification via size exclusion chromatography (SEC) [89]. The segments length distribution is quantified by tapping mode AFM and image analysis using ImageJ software (Fig. 2.30). Knowing the average length of the CNT segments allows the estimation of the molar concentration (70 nM for the unsorted

solution, 10 nM for the (6,5) enriched solution, 48 nM for the metallic SWCNTs solution).

Immediately after PMMA removal, a 40 μl solution of SWCNTs, optimized to promote binding to the hydrophilic lines, is dropped on top of the patterned samples. This solution is made of DNA-wrapped SWCNT segments in DI water (approx 1.2 nM total concentration) with 0.1X TAE buffer, 0.25 DPBS, and with 12.5 mM $MgCl_2$. Samples are incubated in a humidified chamber for 3 hours

In order to image the samples by AFM under dry conditions (Park System XE-100, tips: Mikro Mash NSC16/AIBS), a solvent exchange is performed prior to drying. This is necessary in order to reduce precipitation of salts from the buffer. Each buffered sample is dipped for 10 seconds in 10 ml of a mixture of ethanol (50%) and DI water (50%). It is then transferred to a well containing 10 ml of a 90% ethanol 10% DI water solution, where it is allowed to sit for 50 minutes. The samples are then air dried.

3.3.3 DNA-wrapped SWCNT results and discussion

The best binding yield (one nanotube on one line) is observed for 10 nm wide lines (Fig. 3.8-a). In this case SWCNT segments are found to bind to the patterned lines, in some cases [160] with almost 100% yield (Fig. 3.9). When the lines are patterned as close as 100 nm, some tubes are found to bind diagonally across a few lines (Fig. 3.9-a). This problem is not observed when lines are

patterned far enough apart (500 nm in Fig. 3.9-b). In Fig. 3.9 the SWCNT segments are assembled on top of Au electrodes, but the same results are found for SWCNT segments assembled on SiO_2 and then contacted to electrodes deposited on top. (Details of the electrodes patterning are given in the following section, 3.4.1). The lateral shift in the position of the nanotube segments respect to the electrodes is due to small registration errors in the e-beam patterning.

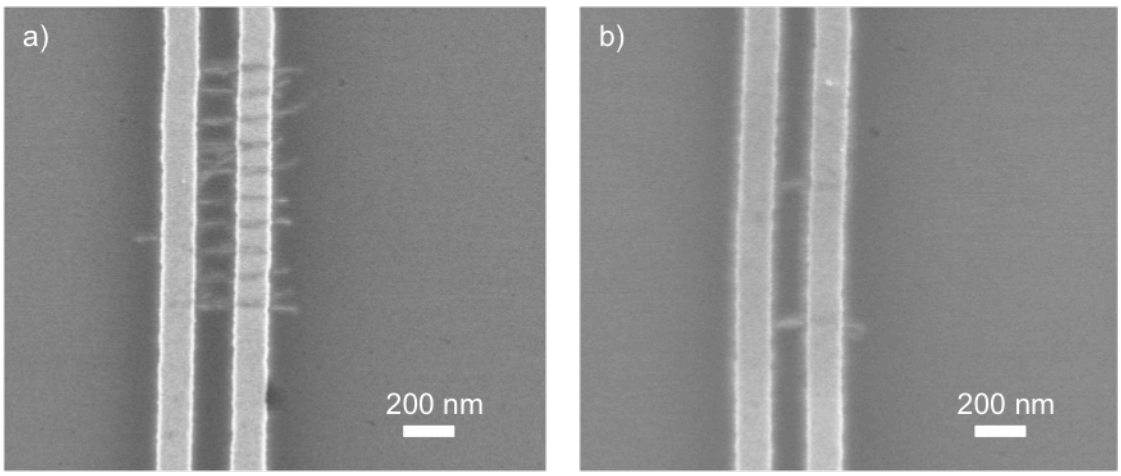

Figure 3.9: SEM images of DNA-wrapped SWCNT segments assembled from solution (mixed chirality solution) onto substrates with pre-patterned Au electrodes. The SiO_2 surface and the Au electrodes are passivated with a PEG layer. The PEG is selectively removed by e-beam patterning of 10 nm wide lines in PMMA and RIE. When lines are patterned as close as 100 nm (a) some tubes are observed to cross over the lines, but when lines are patterned farther apart (500 nm in (b)) no nanotube crossing is observed. The lateral shift in the position of the nanotube segments respect to the electrodes is due to a registration error in the e-beam patterning.

The nanotubes in Fig. 3.9 are deposited from the unsorted solution (mix chirality) but the same binding behavior is observed for the semiconducting (6,5) enriched solution (Figures 3.10-b and 3.11). This is not the case for the solution of metallic SWCNT. Indeed, while the mixed chirality and semiconducting enriched solutions show good selectivity for the hydrophilic areas and lack of binding to the PEG passivated areas, the solution of metallic tubes does not produce selective SWCNT binding to the patterned hydrophilic lines. Moreover, metallic SWCNT are observed to randomly physisorb to the PEG (Figures 3.10a and 3.12). The reason for this behavior is likely found in the two extra polymers in this solution (~20 wt% of polyacrylamide and ~ 2 wt% of polyethylene glycol, not present in the other two solutions) that are necessary for the purification technique used in this case[159].

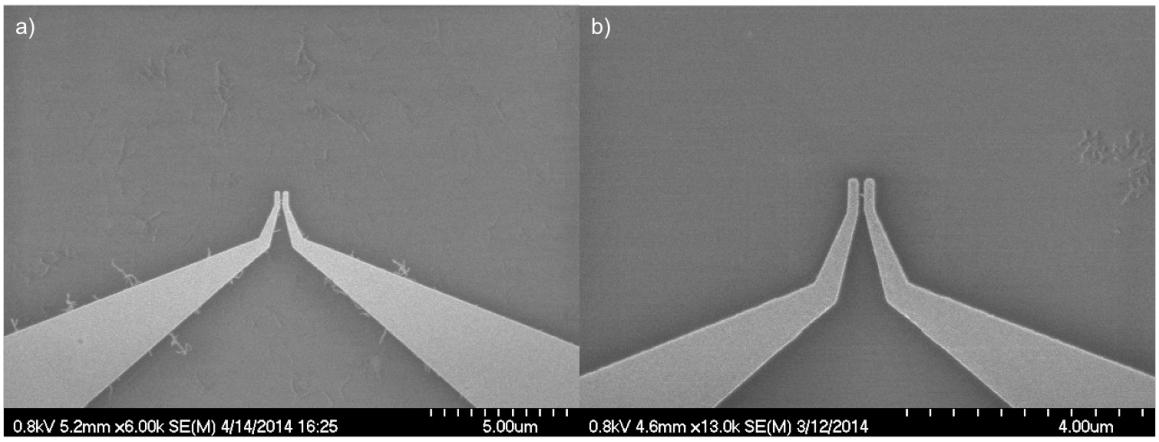

Figure 3.10: SEM images of samples passivated with PEG and patterned with hydrophilic regions (via selective PEG removal). The hydrophilic regions are: one 10 nm wide, 150 nm long line placed between the electrodes, and one square (1 μm side) placed next to the electrodes and used as a control feature.
(a) Assembly of metallic SWCNTs. The binding is not selective and the nanotubes physisorb to the PEG and do not deposit on the hydrophilic regions.
(b) Assembly of semiconducting SWCNTs. In this case the binding is selective and the nanotubes selectively deposit on the line between the electrodes and on the squared feature on the side. No non-specific binding is observed.

Figure 3.11 clearly shows the different conduct of the two solutions. The two SEM images show samples passivated with PEG and patterned with two hydrophilic regions: one 10 nm wide, 150 nm long line placed between the electrodes, and one square (1 μm side) placed next to the electrodes and used as a control feature. The image on the left (a) shows the result of the assembly of metallic SWCNTs. Clearly, the binding is not selective and the nanotubes physisorb to the PEG and do not deposit on the hydrophilic regions. The image on the right (b) shows the result of the assembly of semiconducting SWCNTs. In this case the binding is selective and the nanotubes selectively deposit on the line between the electrodes and on the squared feature on the side. No non-specific binding is observed.

3.4 DNA-wrapped SWCNT electronic devices

This section describes the contacting of solution deposited DNA-wrapped SWCNT with metal electrodes to form three terminal electronic devices, and the transport data obtained from them. As explained in the previous section, two approaches are developed for SWCNT assembly: one on top of pre-patterned electrodes, and one in which SWCNTs are deposited first and then the electrodes are patterned on top. Details of the fabrication of electrodes for both processes are given in the next section (3.4.1).

3.4.1 Patterning of electrodes

Electrodes are patterned by e-beam lithography using a bilayer resist. The bottom layer is made of EL copolymer (Microchem) about 100 nm thick; the top layer is made of PMMA (495K, 2% in anisole, Microchem) about 50 nm thick. If electrodes are patterned before PEG passivation and SWCNT assembly, prior resist spinning, substrates are rinsed with acetone and IPA and exposed to an oxygen plasma for one minute (Diener Plasma Etch System). If electrodes are patterned after PEG passivation and SWCNT assembly, hence on top of the SWCNT segments, prior resist spinning substrates do not receive any treatment (other than the washing and drying process done after the SWCNT assembly). In both cases, the first resist layer is soft-baked for one hour at 155 °C before spinning the second layer; the second resist layer is soft-baked for one hour at

170 °C before being patterned by e-beam (Nanobeam nB4 electron beam lithography system). Development is done in a 1:3 DI water : IPA solution, at room temperature, for one minute. For samples without PEG and SWCNT, a short oxygen plasma (15 s, Diener Plasma Etch System) is performed after development, follow by the e-beam evaporation (Angstrom EvoVac Deposition System) of 1 nm of Ti followed by 50 nm of Au. Lift-off is done overnight in remover PG (Microchem). For samples with PEG passivation and assembled SWCNT segments, a stack of 0.8 nm of Ti, 15 nm of Pd, 35 nm of Au, is deposited directly after development by e-beam evaporation (Angstrom EvoVac Deposition System). In this case lift-off is done overnight in acetone, since NMP based solvents have been found to highly dope SWCNTs. In both cases the substrates used are highly doped Si with 300 nm of thermally grown Si oxide.

3.4.2 Results and discussion

While capable of yielding successful directed deposition of SWCNTs onto or underneath electrodes, the assembly technique described in the previous section does not produce SWCNT devices that conduct electrical current. There are two plausible reasons for this:

- Reduced transport across the SWCNT
- High contact resistance

Both problems are attributable to the same causes: the presence of the DNA wrapping around the SWCNT and possible salt residue (from the buffer solution needed for the assembly).

In order to minimize salt deposition on the SWCNTs, the washing process done after the assembly is changed to: 10 seconds dip in DI water, 20 seconds dip in 10 ml of a mixture of ethanol (50%) and DI water (50%), 50 minutes immersion in 10 ml of an 80% ethanol 20% DI water solution. Samples are then air dried and dipped for 10 seconds in "DNA away" (Molecular BioProducts). They are then rinsed in DI water and finally placed in boiling DI water for 10 minutes and then left overnight to cool down. Finally, samples are dipped in HCl for 10 seconds and rinsed in DI water. If the SWCNT are deposited first, electrodes are patterned following the HCl treatment.

Even after all these cleaning procedures no current is detected in the devices (the correct positioning of the SWCNT segments was checked by SEM after the electrical probing). It is only after annealing at 350 °C for 4 hours in forming gas (Ar and H) that the devices are found to conduct electrical current (Fig. 3.10). When semiconducting SWCNT are assembled, the devices display typical p-type SWCNT FET behavior (the highly doped Si substrate with 300 nm of thermally grown oxide are used as back gate and gate oxide). Noticeably, the annealing step is not sufficient by itself: devices that are not treated with the cleaning procedure described above do not conduct any current.

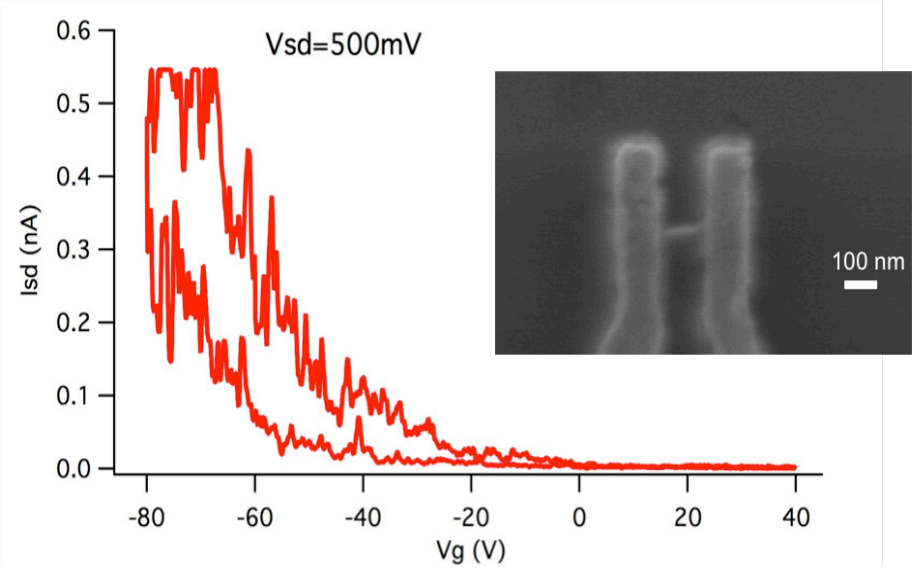

Figure 3.11: Source-drain current (I_{sd}) versus gate voltage (V_g) at 500 mV source-drain bias for the device depicted in the inset SEM image. The device is directed assembled from a (6,5) enriched DNA-wrapped SWCNT solution (as explained in 3.3) and electrodes are patterned on top. Current is detected only performing several cleaning procedures prior electrodes deposition (see main text) and annealing in forming gas at 350 °C for 4 hours post electrodes deposition.

Figure 3.11 shows the source-drain current (I_{sd}) versus gate voltage (V_g) at 500 mV source-drain bias for a device assembled from the (6,5) enriched DNA-wrapped SWCNT solution. The SWCNTs are deposited first and electrodes are patterned on top. All the cleaning procedures described above are applied, together with the post electrodes deposition annealing step. The device was tested before annealing and no current was detected.

When tubes are deposited on top of the electrodes, due to the weaker tube-electrode coupling, in order to get a measurable current through the device a stronger cleaning procedure is required: the time of immersion in HCl is

increased from 10 seconds to 1 hour. This treatment results in devices that conduct electrical current, as shown in Fig. 3.12. Noticeably, no current is measured from samples cleaned with the short HCl immersion (again the correct positioning of the SWCNT segments was checked by SEM after the electrical probing).

The SEM image in Figure 3.12 does not show a perfect outcome of the directed assembly process: non-specific binding to the PEG passivated substrate is visible. The reason for this is that the sample displayed in Fig. 3.12 is made from the metallic SWCNT solution, which contains polyacrylamide and polyethylene glycol. As explained in the previous section, the presence of these two polymers prevents the correct functioning of the directed assembly process.

As an attempt to remove the extra polymers from the metallic SWCNT solution, the solution is centrifuged in Millipore Amicon 100K tubes. Starting with 20 μl of SWCNT solution, 400 μl of DI water are added and the resulting solution is spun down to a 50 μl volume. This procedure is repeated twice. This process does not accomplish a complete removal of the polyacrylamide and polyethylene glycol since the assembly process executed with this solution results in the same behavior observed for the uncentrifuged metallic SWCNT solution. A possible way to obtain a greater removal of the extra polymers is to precipitate the SWCNTs and then redispersed them in DI water. The risk of this procedure is to lose most of the SWCNT material and/or to promote aggregation.

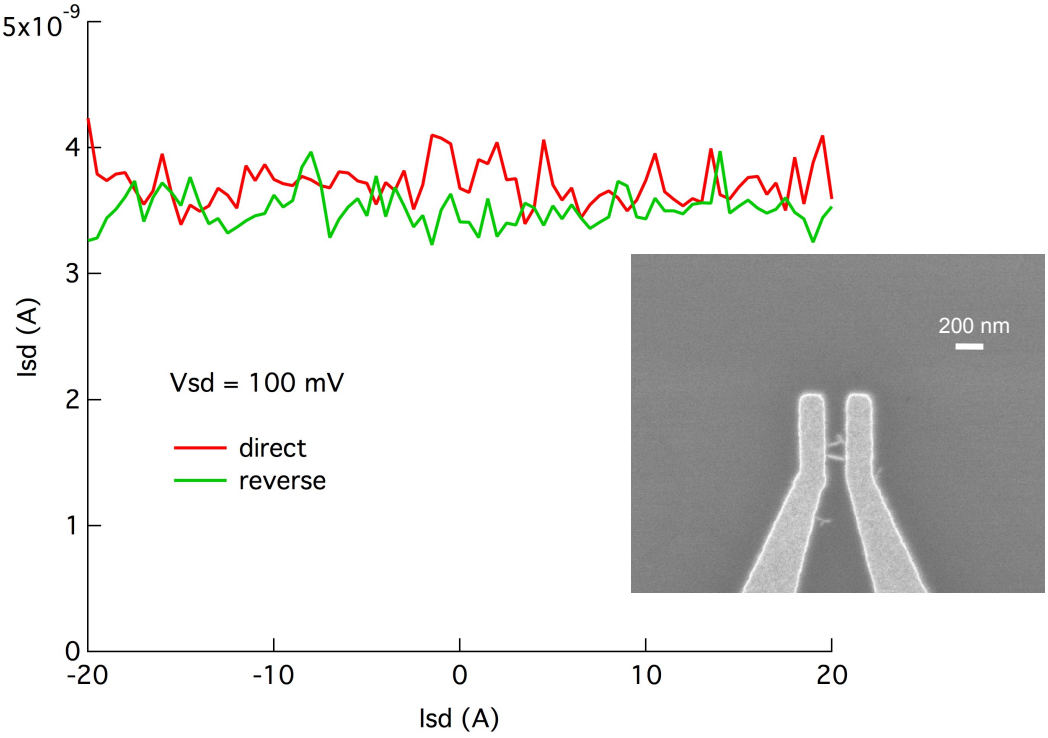

Figure 3.12: Source-drain current (I_{sd}) versus gate voltage (V_g) at 100 mV source-drain bias for the device depicted in the inset SEM image. The device is directed assembled from a metallic DNA-wrapped SWCNT solution and the SWCNTs are deposited on top of the electrodes (as explained in 3.3). The solution contains polyacrylamide and polyethylene glycol that prevent the successful outcome of the directed assembly process (non-specific binding is observed). Current is detected only performing several cleaning procedures including 1 hours immersion in HCl (see main text) and annealing in forming gas at 350 °C for 4 hours.

As shown in figures 3.11 and 3.12, albeit demonstrating the desired functionality, devices obtained from the presented directed assembly technique do not achieve excellent performance. Devices made of metallic SWCNT do not carry high current (1 nA to 10 nA are typically observed values) whereas devices made of semiconducting SWCNT do not demonstrate a high current ratio (10^3 is typically observed). Possible ways to improve upon this result are:

- Longer immersion in HCl.
- Higher temperature annealing in forming gas or hydrogen. (Previous reports on FETs made with DNA-wrapped SWCNT [161, 162] include a high temperature (800 °C) anneal of the SWCNT in hydrogen prior electrode deposition. These devices show good electrical properties, comparable with other devices made by solution assembly [163].)
- Annealing in air at 200 °C for 30 minutes followed by a temperature increased to 400 °C with a hydrogen flow of 300 sccm (standard cubic centimeter per minute). Once the elevated temperature is reached, argon is set to flow for 3 minutes through a water bubbler kept at room temperature with a flow rate of 100 sccm. This cleaning procedure is reported in [164] where sorted DNA-wrapped SWCNT are used as seeds for the growth of SWCNT with uniform chirality. FETs built with such tubes demonstrate on currents of a few μA.

Chapter 4

Nanostructures-molecules hybrids

4.1 Introduction

This chapter describes various techniques to link functional nanostructures with molecules in a controlled fashion. Section 4.2 describes the linking of DNA-wrapped SWCNT segments, in a water solution, to molecules with different morphologies (linear or branched) yielding CNT-molecules hybrid objects reflecting the molecules morphology. Section 4.3 describes the linking of DNA-wrapped SWCNT segments to dsDNA for the purpose of creating a robust, nano-sized electrical contact between the SWCNTs and the DNA. The resulting hybrid structures are electrically probed by contact AFM (section 4.6). The same section discusses difficulties encountered when trying to apply the techniques described in the previous chapter (sections 3.3 and 3.4) to the electrical probing of the dsDNA in the hybrid dsDNA-SWCNT structure. Section 4.4 describes the connection of DNA-wrapped CNT segments and Au nanoparticles by means of a dsDNA linker. Section 4.5 describes the same kind of linkage but between Au nanoparticles and semiconducting nanorods with Au capped ends.

4.2 Controlled formation of carbon nanotube junctions via linker-induced assembly

This sub-chapter presents a simple bottom-up approach for the controlled formation of end-to-end single-walled carbon nanotube (SWCNT) junctions via directed chemical reactions [165]. Chemical reactions are programmed to occur specifically at the ends of well-defined segments of SWCNT to form junctions of end-to-end-linked tubes. Linkers with different shapes yield SWCNT with higher order structures that go beyond simple linear arrays to ones that are multi-terminal and circular. These unusual structures are formed from a self-assembly process in aqueous solution that is controlled by the geometry and the chemical nature of the linker.

4.2.1 Materials and methods

The CNTs used in this section are the same as those described in 2.7. The starting CNT solution consists of short single wall carbon nanotube (SWCNT) segments wrapped in single stranded DNA [DNA sequence: (GT)20] and dissolved in DI water (concentration ~40 μg/ml, calculated from the E11 optical transition) obtained from M. Zheng at NIST. As previously demonstrated by Dr. Zheng and coworkers, DNA wrapping promotes efficient solvation of SWCNT in water [88]. The resulting solution is highly stable and it can be purified into separate batches of SWCNT segments with uniform length and chirality via size-

exclusion chromatography (SEC) [89] and ion exchange chromatography (IEX) [90] respectively.

The length distribution of the SWCNT segments is quantified by tapping mode AFM and software analysis (ImageJ, Fig. 4.1). The average length and standard deviation of the CNT segments in the starting solution are found to be (147.7 ± 92.8) nm. Using this value, the molar concentration of CNT segments is estimated to be about 70 nM.

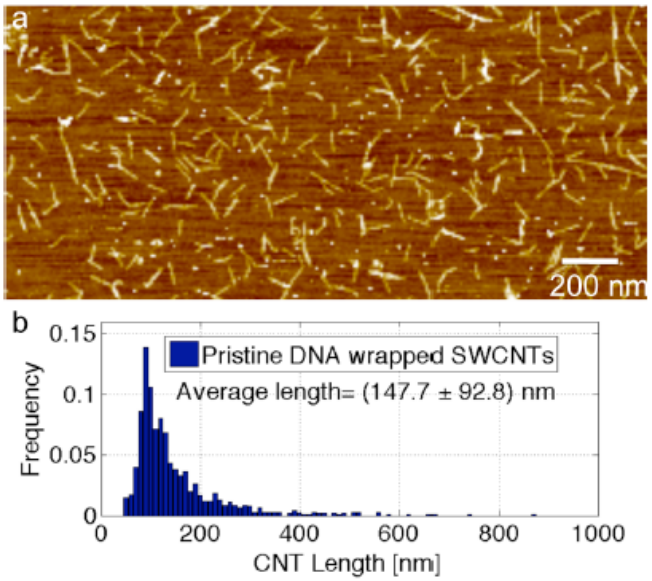

Figure 4.1: (a) AFM topographical image of pristine DNA-wrapped SWCNT. (b) Normalized histogram showing the length distribution of the pristine DNA-wrapped SWCNT. The average length of (147.7 ± 92.8) nm is determined from ca. 1,000 objects.

Ultrasonication in DI water produces SWCNT segments with oxidized ends presenting carboxyl groups [152, 153]. Carboxyl groups react with amine groups resulting in a covalent amide bond. This reaction is employed to attach SWCNT segments to amine-functionalized molecules (Fig. 4.2).

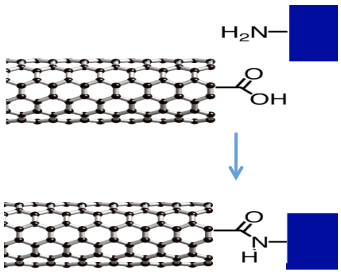

Figure 4.2: Schematic of reaction between the carboxyl groups on the ends of the CNT segments and amine molecules resulting in a covalent amide bond.

Figure 4.3 depicts the three different amine-functionalized molecules used as linkers (labeled A, B and C). Varying the type of linker allows to create either linear (A) or multi-terminal (B,C) SWCNT junctions, where the geometry of the junction is dictated by the chemical and geometrical nature of the molecular linker. The three different molecular linkers employed: A) Hexamethylenediamine, B) Polypropylenimine tetramine dendrimer, and C) PAMAM dendrimer ethylenediamine core, are purchased form Sigma Aldrich.

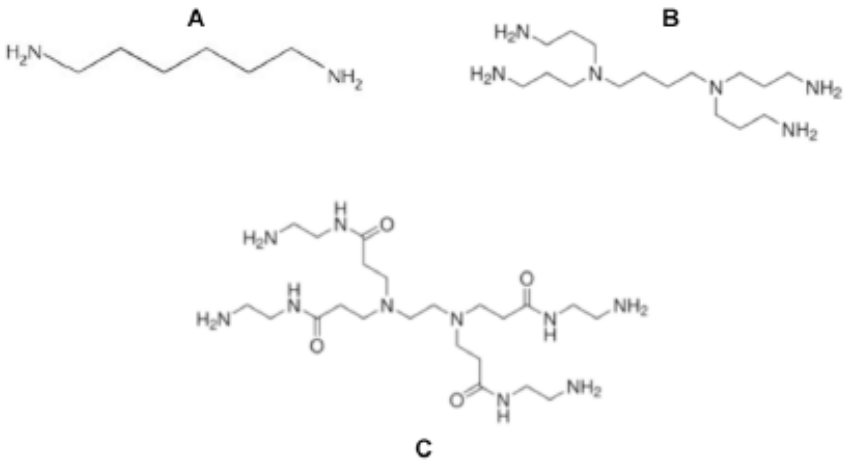

Figure 4.3: The three different molecules employed as linkers: (A) hexamethylenediamine; (B) polypropylenimine tetramine dendrimer; (C) poly(amidoamine) (PAMAM) dendrimer with an ethylenediamine core.

SWCNT carboxylic acid end-groups are activated in buffer solutions containing standard amide coupling and activating agents (sulfo-NHS and EDC). BupH MES buffered saline pack 0.1 M [2-(N-morpholino)ethanesulfonic acid]) is purchased form Thermoscientific, as well as the sulfo-NHS coupling reagent (N-hydroxysulfosuccinimide). The carbodiimide (EDC) activating agent (N-3dimethylaminopropyl-N-ethylcarbodiimide hydrochloride) is purchased form Fluka. This chemistry covalently connects the amine-functionalized molecules to the end of the nanotubes, via an amidation reaction.

Pristine DNA-wrapped SWCNT solutions in DI water are mixed in a volume ratio of 1:1 with a solution of 4 mM EDC and 10 mM sulfo-NHS in 0.2 M MES buffer. The solution so prepared is left activating for 30 minutes and is then diluted 1:1 (by volume) with a ThermoScientific BupH™ Phosphate Buffered Saline

(pH=7.2) (TPBS) solution. The amine functionalized molecular linker is then added at a concentration of 10nM and left reacting for. The solution is filtered (Amicon filters 10KD, Millipore), centrifuging it twice at 6000 rpm for 3 minutes each time. Finally, the solution is mixed in a 1 to 1 volume ratio with an activated (30 minutes in MES buffer with sulfo-NHS and EDC) pristine DNA-wrapped SWCNT solution to increase the coupling yield, and it is left to react overnight. After incubation (4 hours in a moist environment) samples are washed with an ethanol-DI water mixtures: immersion in a 50 % DI water 50 % ethanol solution for 10 s and then in a 10 % DI water 90 % ethanol solution for 50 min. In both cases the amount of solution per sample is 10 ml. The samples are finally dried in air. For AFM imaging, solutions are cast on silicon wafers with 300 nm-thick layer of thermally grown silicon dioxide. Low concentration films are cast on the substrate, in order to minimize aggregation and clearly see the resulting structures. AFM imaging is performed with an XE-100 Advanced Scanning Probe Microscope (PSIA) in non-contact mode imaging; Mikromasch NSC16, (spring constant 40 N/m), n-type silicon (phosphorus doped) tips are utilized. The images are analyzed using XEI software, version 1.7.6. Length distributions are calculated using ImageJ 1.40g software, via the “Analyze Particles” tool. Histograms are generated by Matlab version 7.11.1.866. For TEM imaging (done using a JEOL JEM-100CX), solutions are cast on amorphous carbon TEM grids (Ted Pella). After drying they are washed with 20 μl of DI water and fully dried in air or vacuum.

4.2.2 Results and discussion

Figure 4.4 shows AFM and TEM images of linear SWCNT junctions typically obtained employing molecule A (Fig. 4.3) as a linker. The average length of the SWCNT segments is found to increase from (147.7 ± 92.8) nm for the pristine DNA-wrapped SWCNT starting material to (418.2 ± 370.1) nm when reacted with molecule A in solution. This significant increase in average length of the nanostructures visualized on the substrate indicates the formation of linear SWCNT junctions.

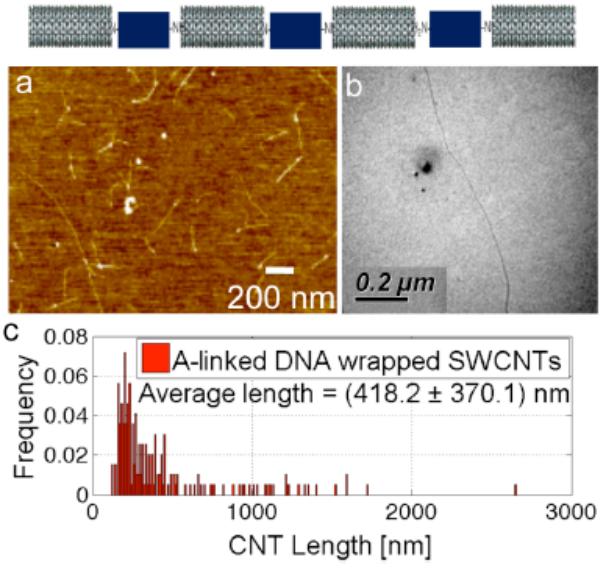

Figure 4.4: (Top) Schematic of linear end-to-end SWCNT junctions. (a) AFM topographical image and (b) TEM image of linear end-to-end SWCNT junctions formed using molecular linker A. (c) Normalized histogram showing the length distribution of A-linked structures. The average length of (418.2 ± 370.1) nm is determined from ca. 200 objects.

In order to create multi-terminal SWCNT junctions a branched molecule (molecule B in Fig. 4.3) is employed to interconnected SWCNT segments via the same reaction (i.e. amidation) described above. Figure 4.5 show various multi-terminal SWCNT junctions formed employing linker B. These Y-junctions predominantly exhibit the same height of the pristine SWCNT (i.e. around 1.2 nm) confirming that the junctions are the result of nanotube interconnections, rather than bundling. The average length of these structures is (522.5 ± 351.4) nm. Notably, junctions of this kind may be an interesting route toward the creation of three terminal nanodevices (e.g. field effect transistors).

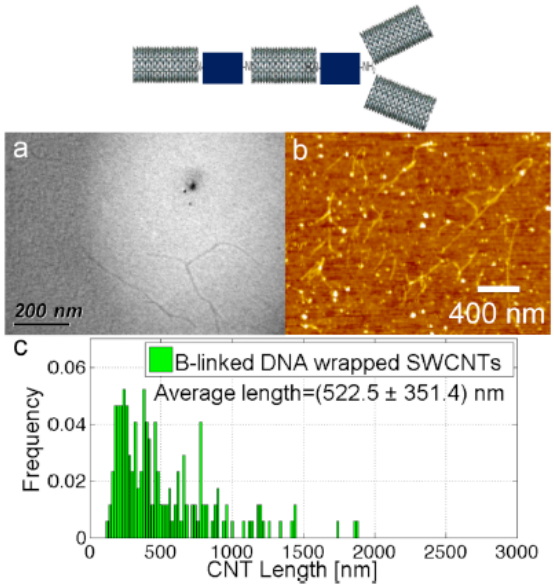

Figure 4.5: (Top) Schematic of a Y-shaped end-to-end SWCNT junction. (a) TEM image and (b) AFM topographical image of multi-branched end-to-end SWCNT junctions formed using molecular linker B. (c) Normalized histogram showing the length distribution of B-linked SWCNT. The average length of (522.5 ± 351.4) nm is determined from ca. 200 objects.

When molecule C is used as a molecular bridge in SWCNT junction formation, the longer branched chains are expected to minimize steric hindrance effects upon attachment of two or more SWCNT segments. Furthermore the amide functional groups can induce hydrogen-bond formation among different molecules/linkers, and therefore add an extra non-covalent stabilizing effect. Figure 4.6 shows a TEM image of the typical multi-terminal junctions observed employing linker C. The average length of such junctions 1s determined to be (524.1 ± 366.9) nm, as shown in the histogram in Fig. 4.6.

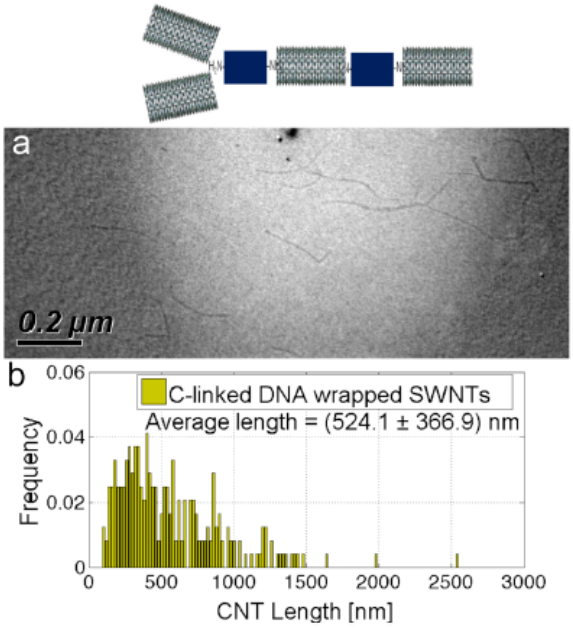

Figure 4.6: (top) Schematic of a Y-shaped end-to-end SWCNT junction. (a) TEM image of multi-branched end-to-end SWCNT junctions formed using molecular linker C. (b) Normalized histogram showing the length distribution of C-linked SWCNT. The average length of (524.1 ± 366.9) nm is determined from ca. 200 objects.

Employing molecular bridge C side-to-side interactions among multiple SWCNT segments are observed together with ring shaped assemblies (Fig. 4.7). Parallel nanotube arrays, can be useful for high-performance electronics applications [116]. Moreover, ring-like structures can be potentially valuable as quantum interferometers for the production of tunable nanoscale electronic switching devices [166, 167].

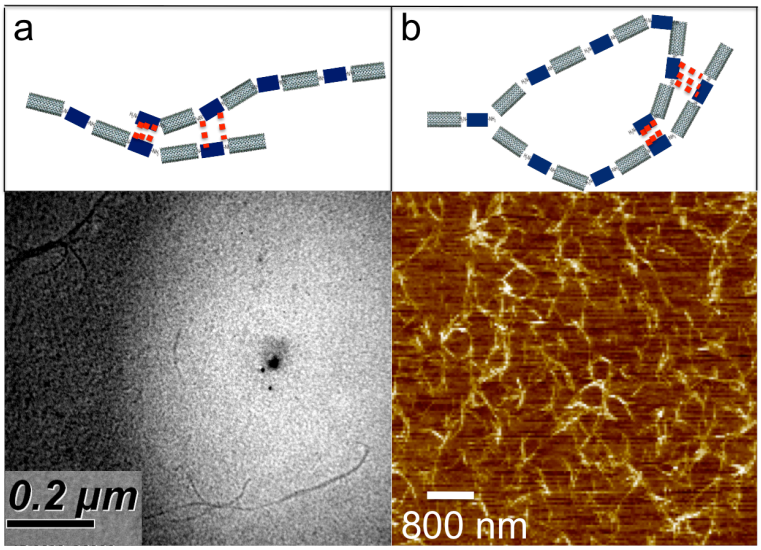

Figure 4.7: SWCNT assemblies employing molecule C as the linker. (a) Schematic and TEM image of parallel SWCNT architectures and (shown as red dashes) the possible van der Waals and hydrogen bond interactions, among C linkers, involved in their formation. (b) Schematic and AFM topographical image of circular SWCNT assemblies. The average diameter of the ring-like structures is found to be (408.1 ± 100.2) nm.

The SWCNT assemblies observed employing molecular bridge C (Fig. 4.7) are likely to be stabilized by an interplay between van der Waals interactions and hydrogen bond formation among linkers bridging the nanotubes. When

trifluoroacetic acid (TFA) is added to SWCNT solutions to disrupt the hydrogen bond formation among C-type linkers, no linear or circular side-to-side assemblies are observed.

In order to further confirm that the end-to-end linkage of SWCNT segments is due to amidation, the reaction with the three molecular linkers is carried out without the activating agents EDC and sulfo-NHS. In this case, the average length of the objects obtained after the reaction is comparable to the average length of SWCNT segments in the starting solution (Fig. 4.8). After reaction with linker A the average length is found to be (206.5 ± 69.8) nm; after reaction with linker B the average length is found to be (208.2 ± 84.2) nm; after reaction with linker C the average length is found to be (211.2 ± 83.0) nm; the average length of the starting SWCNT solution is (177.5 ± 39.4) nm. A low yield of successful amidation, as well as some supramoelcular interactions, is expected to take place even without the activating agents, explaining the slightly higher average length after the reactions.

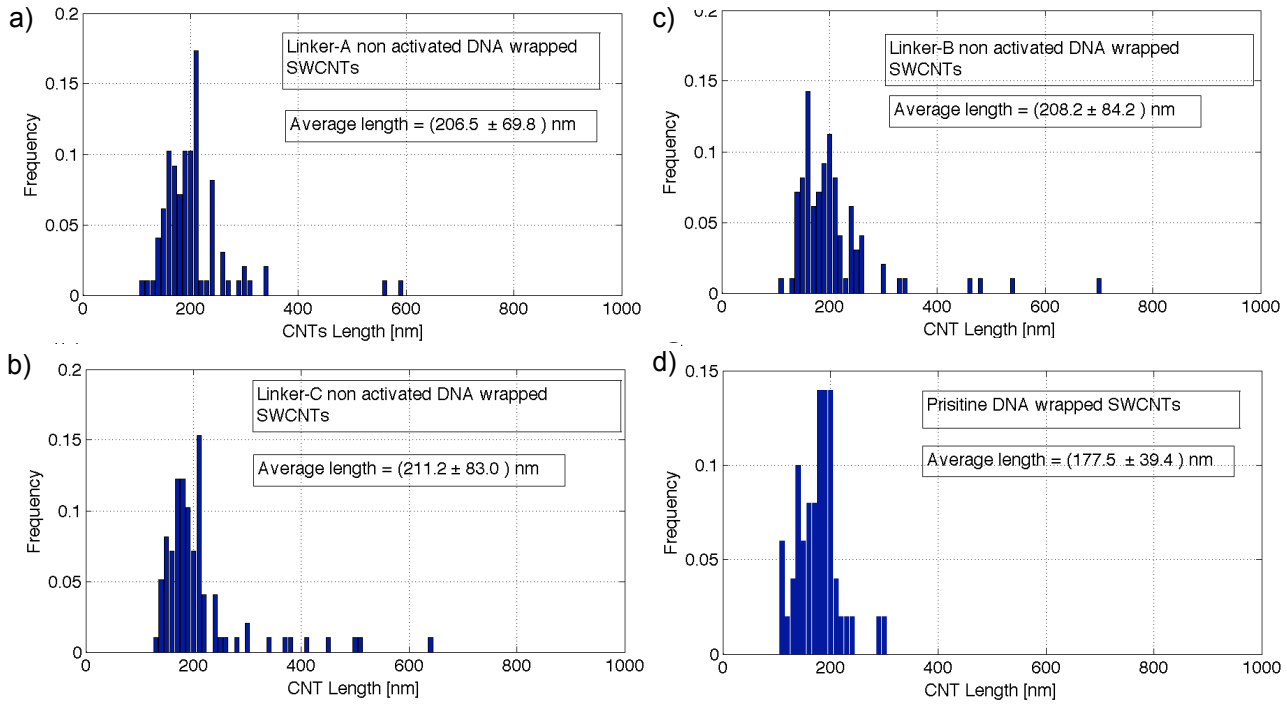

Figure 4.8: (a), (b) and (c) Normalized histograms of the length distribution of DNA-wrapped SWCNT after addition of molecular linkers A, B and C without the amide coupling and activating agents (sulfo-NHS and EDC). (d) Normalized histogram of the length distribution of the DNA-wrapped SWCNT solution employed in this control experiment. In all cases the lengths are determined from ca 100 objects.

This approach is of general applicability for the fabrication of solution-processable CNT-based nanodevices. Three terminal connections to molecules can be used, for example, for the development of individually gated molecular logic devices. The strategy presented here can also be utilized to selectively dope carbon nanotube networks, employing functional groups that can act as electron donors/acceptors.

4.3 Carbon nanotube junctions with double stranded DNA

The experiment described in this section closely resembles the one of the previous section, differing from it primarily in the kind of molecule employed as a linker. In this case DNA-wrapped SWCNT segments are linked through amine functionalized dsDNA (26 base pairs mixed sequence with amine functionalized ends: 5'-CATTAATGCTATGCAGAAAATCTTAG/Amino/-3' hybridized to 5'-CTAAGATTTTCTGCATAGCATTAATG/Amino/-3'). The choice of this DNA sequence is dictated by its previous employment in DNA conductivity experiments by our collaborators in the Porath lab[168].

This work is motivated by the original work of Guo et al. [169, 170], which demonstrated the efficacy of SWNT electrodes for the study of charge transport through individual molecules. SWCNTs are nearly ideal for this purpose. They are outstanding one-dimensional conductors, they can be linked to organic molecules through straightforward carbon-carbon chemistries, and they are essentially the same size (diameter) as individual molecules, virtually ensuring that only a single molecule is being probed in each experiment. This platform was first applied to the study of charge transport in DNA by the Nuckolls group at Columbia, where they demonstrated efficient transport through well-matched dsDNA strands connected to SWCNTs via an amine linkage, supporting the contention that dsDNA contacted in this way maintains its native conformation [51]. The single-molecule devices in that and the previous work were fabricated by a process in which a nanoscale gap in a SWCNT is formed by "cutting" the

SWCNT through a lithographically defined stencil using an oxygen plasma. This approach has been quite successful, in terms of demonstrating electron transport in DNA and other molecules, however, it is extremely inefficient; only ~3% or fewer of the cut nanotubes resulted in reconnection with the DNA. The primary reason for this is thought to be the difficulty in precisely matching the size of the opening to the length of the dsDNA molecule. The approach described in this section overcomes this difficulty by performing the connection between the DNA molecule and the SWCNT electrodes in solution by chemical means. Once these hybrid structures are formed, they can be placed on a surface for electrical measurement, using either a shadow mask electrode in conjunction with a conductive AFM tip (a technique developed by the Porath lab) or using pre-patterned electrodes on the surface. The extended length of the SWCNT-dsDNA hybrids renders them far easier to contact than individual DNA molecules. Details of electrical measurements are in section 4.6.

SWCNT-dsDNA hybrid complexes (Fig. 4.9) are created by reacting an aqueous solution of SWCNT segments with amine functionalized dsDNA (amine-26bp: 26 base pairs mixed sequence with amine functionalized ends). Two reaction schemes are developed, one consisting of a single reaction step, the other consisting of two steps. The second scheme results in a higher yield of the desired SWCNT-dsDNA-SWCNT structure (Fig. 4.9). A third reaction scheme is developed as well, consisting on SWCNT-dsDNA hybrid structure formation through complementary ssDNA hybridization. The yield of this reaction is much lower than the one of other two.

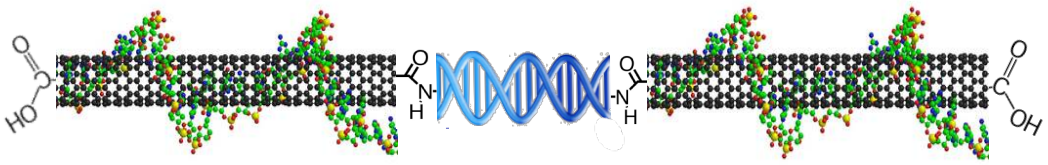

Figure 4.9: Schematic of end-connected SWCNT-dsDNA hybrid structure.

4.3.1 DNA-wrapped SWCNT starting solution

The starting material consisted of short SWCNT segments wrapped in single stranded DNA [DNA sequence: (GT)20] and dissolved in deionized water (concentration ~40 μg/ml), obtained from M. Zheng at NIST. The solution is the result of a purification procedure based on size-exclusion chromatography (SEC) which sorts the CNT segments into fractions of uniform length [89]. The SWCNT segment length distribution is quantified by tapping mode AFM imaging and software analysis (ImageJ, Fig. 4.10). AFM samples are obtained by depositing 10 μl of CNT solution diluted 1:20 in deionized water, on a silicon dioxide substrate treated with oxygen plasma. The solution is dried in air and the samples are then washed by dipping them for 10 seconds in a solution of 50% DI water, 50% ethanol, then immersing them in a solution of 10% DI water, 90% ethanol for 50 minutes and finally letting them dry in air. The average length of the CNT segments in the starting solution is measured to be (147.7 ± 92.8) nm. Using this average length the molar concentration of CNT segments is estimated to be about 70 nM.

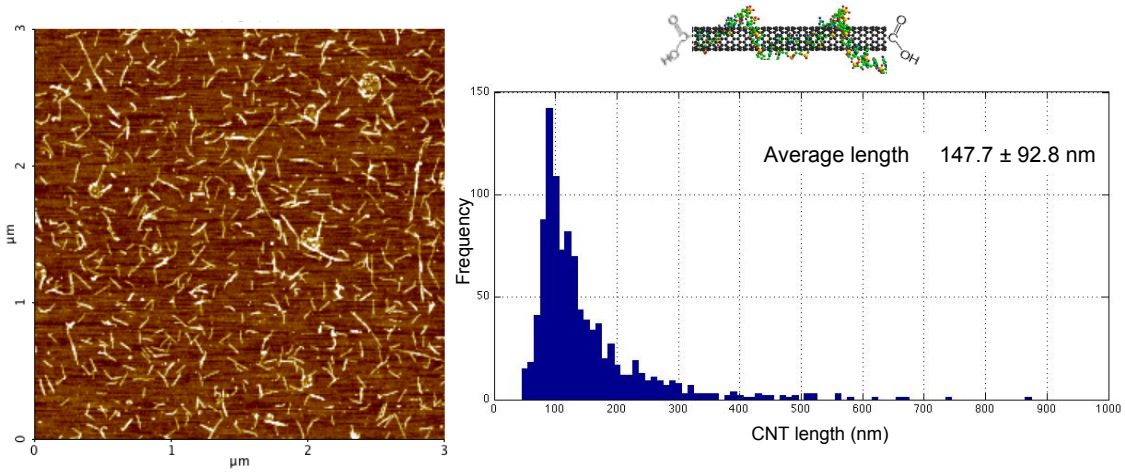

Figure 4.10: (Left) Tapping mode AFM image of DNA-wrapped SWCNT segments deposited on SiO_2. (Right) Histogram of the SWCNT segments length distribution. The histogram is built by measuring 1,024 segments with software ImageJ, from different images of different substrates on which the same solution is deposited. The average length is found to be (147.7 ± 92.8) nm. (Top) Schematics of a DNA-wrapped SWCNT segment.

4.3.2 One step reaction with dsDNA

The two complementary strands (5'-CATTAATGCTATGCAGAAAATCTTAG/Amino /-3' and 5'-CTAAGATTTTCTGCATAGCATTAATG/Amino/-3') are hybridized by mixing 1:1 1 µM solutions in 1X DPBS buffer, increasing the temperature to 65 °C, holding it for 1 hour and then cooling it down slowly to room temperature. In the first scheme, a one step reaction, the starting SWCNT solution is activated by mixing it, 1:1 by volume, with a solution consisting of 0.2 M MES buffer (pH 6), 4 mM EDC and 10 mM sulfo-NHS. The SWCNTs sit in this solution for 30 minutes at room temperature, during which the EDC and sulfo-NHS form an intermediate compound with the carboxyl groups on the CNT

ends. Following activation, 2 μl of 0.5 μM amine-26bp is added. The intermediate compound reacts with the amine groups on the DNA strands resulting in a covalent bond between the dsDNA and the SWCNT segments. This method for DNA attachment to acid-oxidized carbon nanotubes ends was previously reported by Weizmann et al. [171]. The concentration of amine-26bp during the reaction is 5 nM, corresponding to about one seventh of the nanotube concentration. This concentration ratio increases the probability that each DNA strand reacts with two nanotube segments, one on each side, yielding the desired SWCNT-dsDNA hybrid structure. The mixture is left to react overnight at room temperature. Any unreacted DNA strands are removed by centrifugation in Millipore Amicon 100K tubes. During purification the buffer is exchanged to DPBS 1X.

A histogram showing the length distribution of the resulting SWCNT-dsDNA hybrid structures (Fig. 4.11) is obtained by tapping mode AFM imaging and software analysis as explained above for the starting SWCNT solution. The average length and standard deviation of the CNT-dsDNA synthesized by this one step reaction are (325 ± 283) nm, suggesting that the desired SWCNT-dsDNS-SWCNT complex is indeed attained.

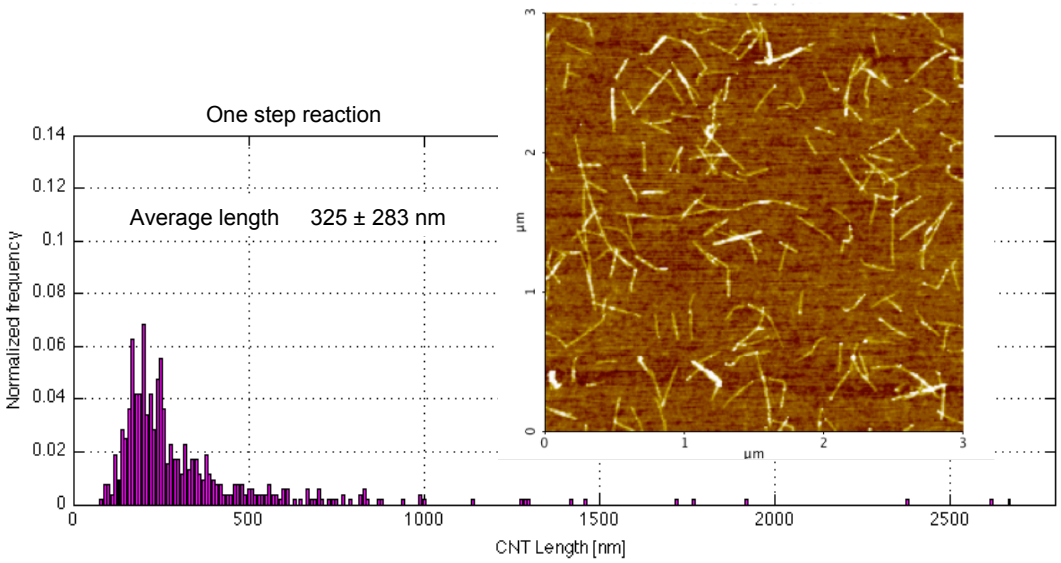

Figure 4.11: Histogram of the length distribution of the CNT-dsDNA hybrid structures obtained with the one step reaction. The histogram is built by measuring the SWCNT length with ImageJ software. 525 nanotube segments are measured, from different AFM images of different substrates on which the same solution is deposited. The average length and standard deviation are found to be (325 ± 283) nm. (Inset) Tapping mode AFM image of the SWCNT-dsDNA solution generated by the one step reaction.

4.3.3 Two steps reaction with dsDNA

A second, two steps reaction is also investigated. In this scheme, 20 µl of the starting SWCNT solution is mixed, 1:1 by volume, with a solution consisting of 0.2 M MES buffer, 4 mM EDC and 10 mM sulfo-NHS. This solution is let to activate for 30 minutes at room temperature before adding 20 µl of 0.5 µM amine-functionalized dsDNA (amine-26bp). The resulting concentration of amine-26bp is 167 nM, making it sufficiently likely that both ends of all SWCNT segments are saturated. The mixture is left to react overnight at room

temperature. Any unreacted DNA strands are removed by centrifugation in Millipore Amicon 100K tubes (the residual concentration of dsDNA after purification is estimated to be less than 0.5 nM). During purification the buffer is exchanged to DPBS 1X. 20 μl of the starting SWCNT solution is mixed, 1:1 by volume, to a solution consisting of 0.2 M MES buffer, 4 mM EDC and 10 mM sulfo-NHS. This solution is left to activate for 30 minutes at room temperature before adding it to the same volume of the purified SWCNT-dsDNA. This second reaction produces the attachment of the activated SWCNT segments to the ones previously bound to the dsDNA.

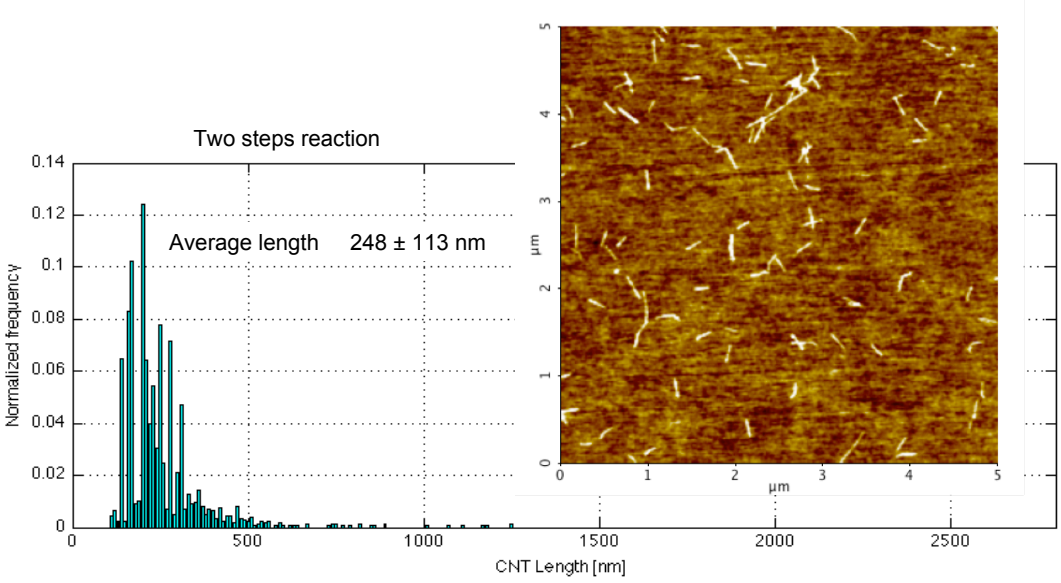

Figure 4.12: Histogram of the length distribution of the SWCNT-dsDNA hybrid structures obtained with the two steps reaction. The histogram is built by measuring the SWCNT length with ImageJ software. 1833 nanotube segments are measured, from different AFM images of different substrates on which the same solution is deposited. The average length and standard deviation are found to be (248 ± 113) nm. (Inset) Tapping mode AFM image of the SWCNT-dsDNA solution generated by the two steps reaction.

The size distribution of the resulting CNT-dsDNA hybrid structures is shown in Fig. 4.12. The average length and standard deviation of the CNT-dsDNA synthesized by this two steps reaction are (248 ±113) nm. The difference between the one-step and the two-step reactions is discussed below.

4.3.4 Junction formation through DNA hybridization

An alternative approach is attempted to create SWCNT-dsDNA-SWCNT hybrid structures: two separate batches of the same DNA-wrapped SWCNT segments are first end-functionalized, in solution, with the two complementary amine-functionalized ssDNA forming the DNA duplex used in the experiments previously described (5'-CATTAATGCTATGCAGAAAATCTTAG/Amino/-3' and 5'-CTAAGATTTTCTGCATAGCATTAATG/Amino/-3'). Again 20 μl of the starting SWCNT solution is mixed, 1:1 by volume, with a solution consisting of 0.2 M MES buffer, 4 mM EDC and 10 mM sulfo-NHS. This solution is left to activate for 30 min at room temperature before adding 20 μl of 0.5 μM amine-functionalized ssDNA (amine-26ss). Two solutions of the two strands are made separately. The resulting concentration of amine-26ss is 167 nM, making it sufficiently likely that both ends of all SWCNT segments are saturated. The mixture is left to react overnight at room temperature. Excess ssDNA is removed from both solutions by centrifugation in Millipore Amicon 100K tubes (the residual concentration of dsDNA after purification is estimated to be less than 0.5 nM). During purification the buffer is exchanged to DPBS 1X. The two

purified solutions of complementary ssDNA functionalized DNA-wrapped SWCNT are mixed and left to hybridize overnight at room temperature. The length distribution of the SWCNT-dsDNA hybrid structures is quantified by tapping mode AFM imaging and software analysis (ImageJ). AFM images clearly revealed that the yield of this reaction is much lower than the two previously described (Fig. 4.13). Indeed in this case the average length distribution and standard deviation are (179 ± 104) nm, comparable to the ones of the starting SWCNT solution of (147.7 ± 92.8) nm.

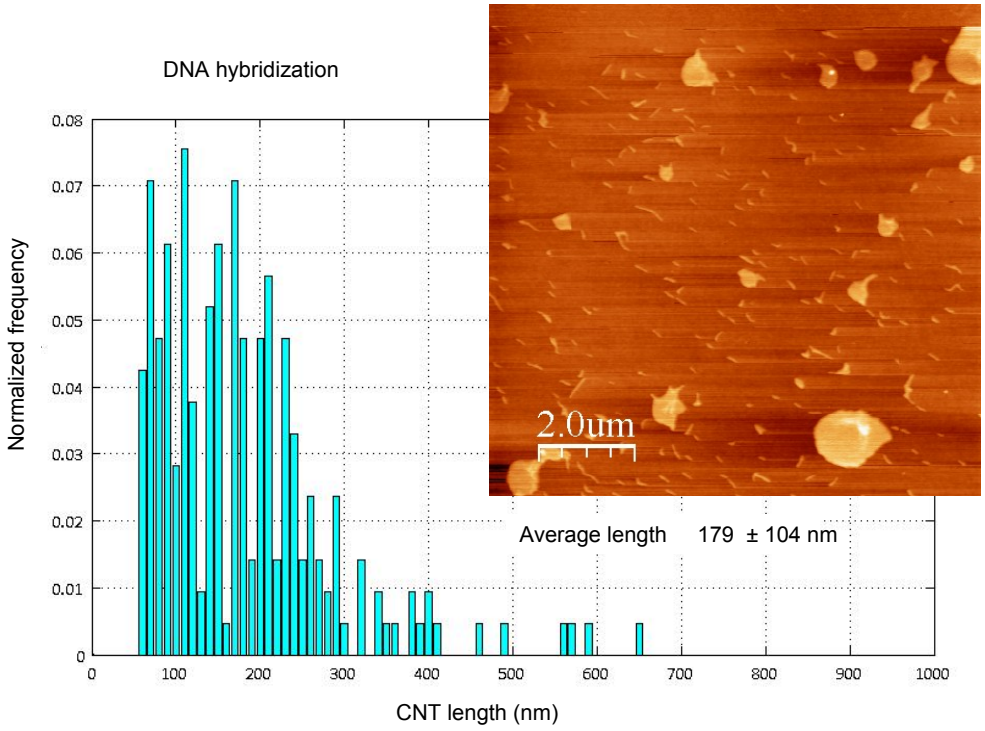

Figure 4.13: Histogram of the SWCNT-dsDNA hybrid structure obtained from hybridization of complementary ssDNA functionalized SWCNT segments. The histogram is built by measuring the SWCNT length with ImageJ software. 212 nanotube segments are measured. The average length and standard deviation are (179 ± 104) nm. (Inset) Tapping mode AFM image of the SWCNT-dsDNA solution generated by the two steps reaction.

4.3.5 Discussion

Both the one step and two steps synthesis schemes result in the formation of SWCNT-dsDNA hybrid structures, as demonstrated by the increase in the average length, shown in the two distributions. However, the two steps reaction produces a significantly narrower length distribution (the standard deviation is 283 nm for the one step reaction; it is 113 nm for the two steps reaction), which likely reflects a higher yield of the desired SWCNT-dsDNA hybrid structure. This is reasonable, since in the one step scheme, a percentage of the SWCNT segments could be expected to be saturated with dsDNA on both ends, rendering them unable to link any further. The two-step scheme remedies this by introducing a new, unreacted population of activated SWCNTs that can bind with the saturated nanotubes.

On the other hand, the reaction based on hybridization of complementary ssDNA end-functionalized SWCNT doesn't result in a high yield of linked SWCNT-dsDNA-SWCNT structures. Two possible ways of improving the outcome of this reaction would be increasing the concentration of hybridizing complementary ssDNA end-functionalized SWCNT segments or to add magnesium ions to the solution. None of these was attempted because the two reactions directly attaching dsDNA seemed more worth pursuing.

Figure 4.14 shows a small area AFM scan of a dilute solution of SWCNT-dsDNA hybrids deposited on mica. Several different conformations can be observed, including both straight and kinked structures, which correspond to what would

be expected for the SWCNT-dsDNA hybrids. Presumably, the kink could indicate the location of the dsDNA within the structure.

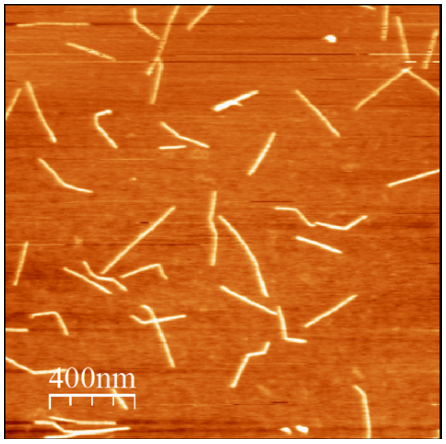

Figure 4.14: Tapping mode AFM image of the SWCNT-dsDNA solution generated by the two steps reaction and deposited on mica.

4.4 dsDNA linkage of SWCNT ends to Au nanoparticles

In this section SWCNT segments are attached to gold nanoparticles (Au NPs) through a DNA duplex. This process is developed as an alternate way to connect dsDNA to two conductive nanostructures having comparable size to the dsDNA molecule and the ability to work as electrodes. It is intended to be used with the conductive AFM technique detailed in section 4.6 where the SWCNT is contacted to a metal electrode evaporated through a shadow mask, and the nanoparticle is contacted to a conductive AFM tip [168]. In this context the nanoparticle is preferable to a SWCNT segment because it is easily recognizable with AFM. It therefore allows unambiguous identification of dsDNA in between a

SWCNT and a NP. As shown in section 4.6, when dsDNA is connecting two SWCNTs topological AFM does not have the resolution necessary to discern the dsDNA from the SWCNT.

DNA-wrapped SWCNT segments are functionalized at the ends with ssDNA (through amine-carboxyl reaction) and subsequently connected, through DNA hybridization, to Au NPs coated with the complementary ssDNA. All these reactions are done in solution. The DNA-wrapped SWCNT DI water solution is mixed, 1:1 by volume, with a solution consisting of 0.2 M MES buffer, 4 mM EDC and 10 mM sulfo-NHS. This solution is let to activate for 30 min at room temperature before adding 26 basis long 3' amine-functionalized ssDNA (amine-26ss: 5'-CATTAATGCTATG CAGAAAATCTTAG/Amino/-3'). The resulting concentration of amine-26ss is 167 nM, making it sufficiently likely that both ends of all SWCNT segments are saturated. The mixture is left to react overnight at room temperature. Excess ssDNA is removed from both solutions by centrifugation in Millipore Amicon 100K tubes (the residual concentration of dsDNA after purification is estimated to be less than 0.5 nM). During purification the buffer is exchanged to DPBS 1X. Gold nanoparticles (Au NPs) 10 nm in diameter are functionalized, through thiol linkage, with the 26bp complementary strand with a thiol group on the 5' side (thiol-26ss-comp: 5'-CTAAGATTTTCTGCATAGCATTAATG/3ThioMC3-D/-3'). The concentration of Au NPs in solution is about 0.5 μM. The Au NPs solution is mixed with the purified amine-26ss end-functionalized SWCNT solution in a 1:9 volume ration. They are left to react at room temperature for different amounts of time, from 18 to

48 hours, and then imaged with a TEM. For TEM imaging 4 μl of the reacted solution are deposited on an amorphous carbon TEM grids (Ted Pella) dried in a vacuum dessicator, washed with 20 μl of DI water and then dried again in a vacuum dessicator before imaging.

Figure 4.15 shows TEM images of the SWCNT-dsDNA-AuNPs structures after 24, 48 and 120 hours reaction time. It appears that a longer reaction time does not increase the yield of Au NPs attachment to the SWCNT ends but it rather promotes interactions with the SWCNT sidewalls. A high yield of NPs hybri-dization with the SWCNT ends is not achieved. 24 hours incubation results in the best ratio of end-functionalization versus sidewall interaction (Fig. 4.16).

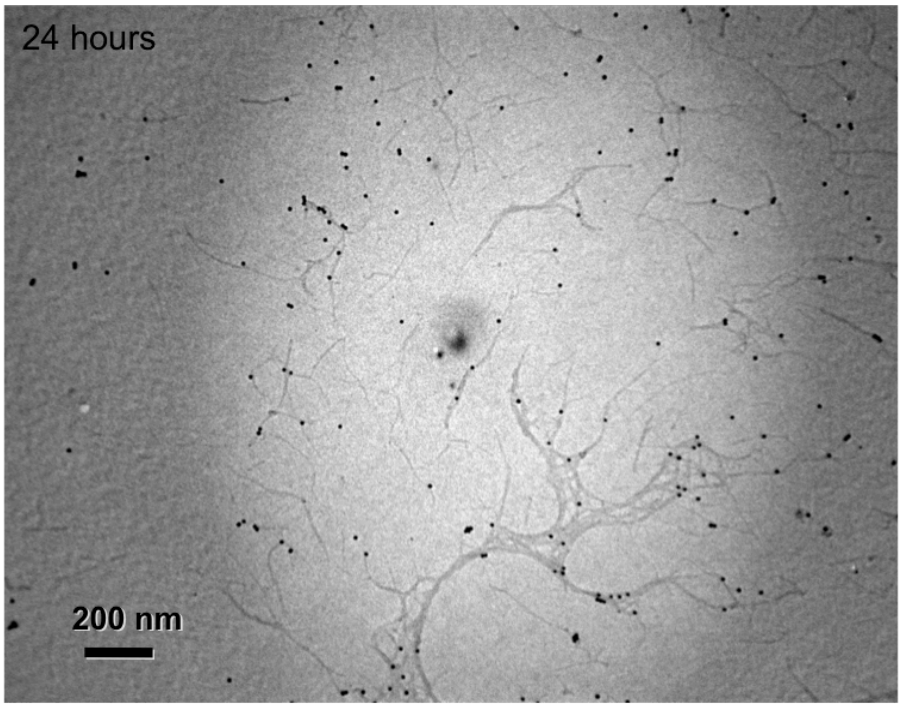

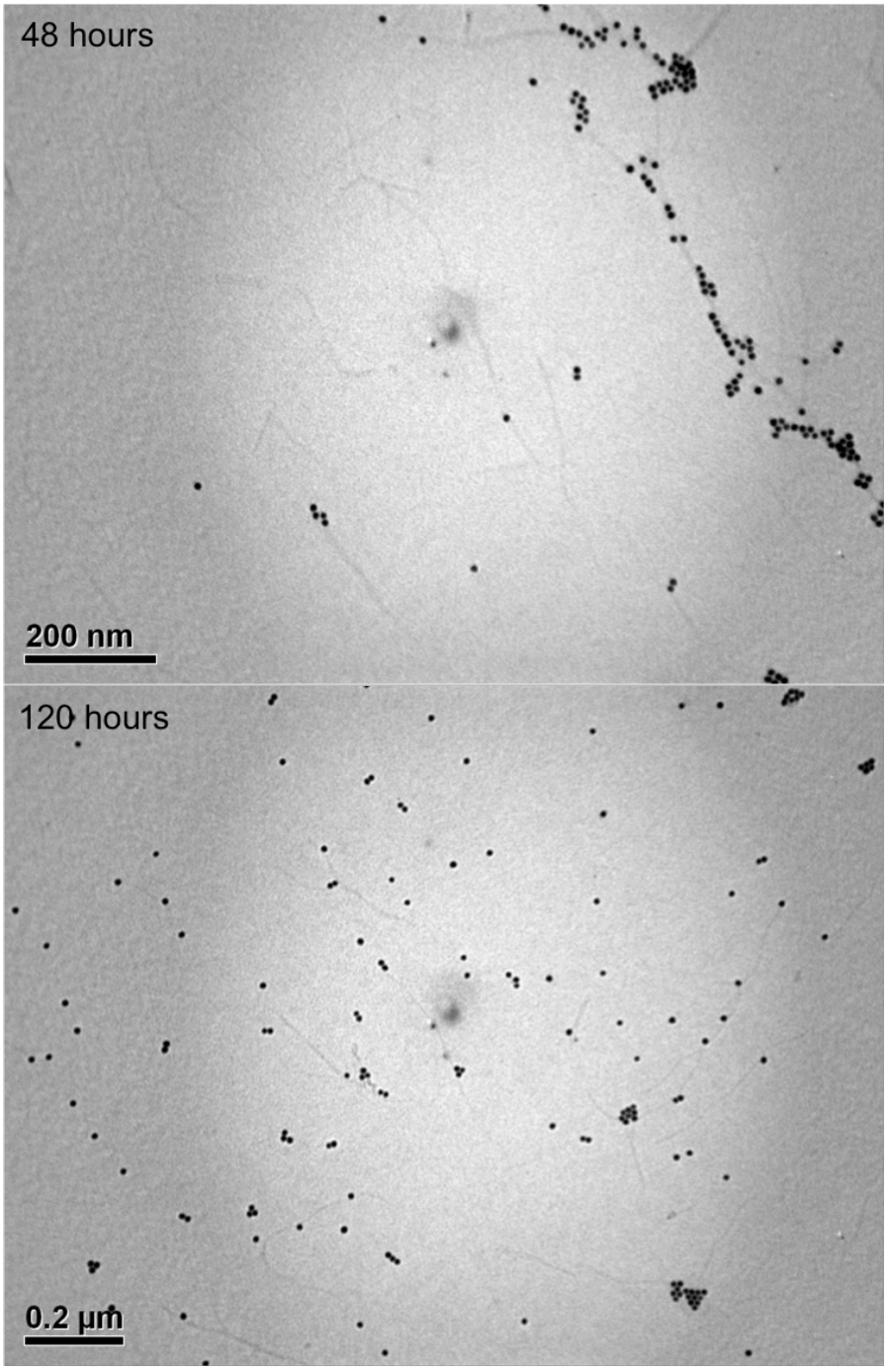

Figure 4.15: TEM images of DNA-wrapped SWCNT segments functionalized at the ends with ssDNA complementary to the one coating Au NPs 10 nm in diameter. The two ssDNA functionalized nanostructures are allowed to react for (Previous page) 24 hours, (Top) 48 hours or (Bottom) 120 hours. Longer reaction time doesn't increase the end attachment but it rather increses the interaction with the nanotubes sidewalls.

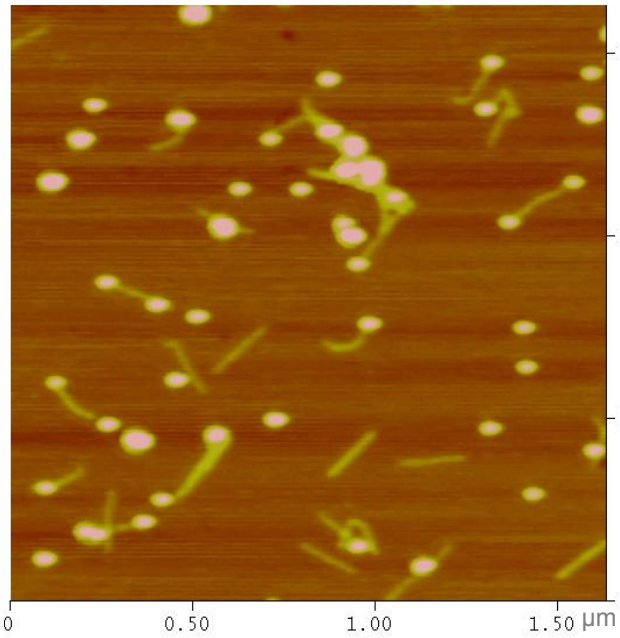

Figure 4.16: AFM image of DNA-wrapped SWCNT segments functionalized at the ends with ssDNA complementary to the one coating Au NPs 10 nm in diameter. The two ssDNA functionalized nanostructures are allowed to react for 24 hours.

As a control experiment, the ssDNA functionalized Au NPs are incubated with the DNA-wrapped SWCNT segments with no end-functionalization. Figure 4.17 shows a TEM image of the objects obtained after 24 hours incubation. In this case the interaction between the SWCNT ends and the Au NPs is almost absent. For single SWCNT segments the NPs attachment to the sidewalls is comparable with the previous case while it looks higher in the presence of SWCNT bundles.

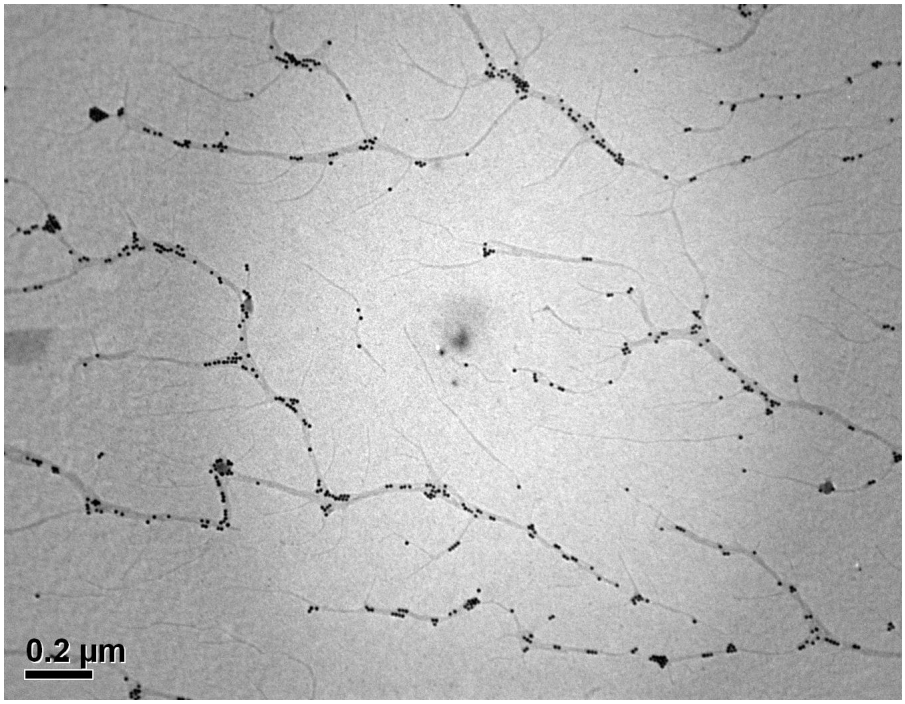

Figure 4.17: TEM images of DNA-wrapped SWCNT segments without ssDNA end functionalization mixed with ssDNA coated Au NPs 10 nm in diameter. The two ssDNA functionalized nanostructures are allowed to react for 24 hours prior imaging.

4.5 Directed assembly of semiconducting nanorods with Au capped ends

In this section another one dimensional nanomaterial is selectively functionalized in solution with the purpose of obtaining chemically active nanostructures that can assemble on pre-patterned substrates using the techniques illustrated in chapter 2. Semiconducting nanorods with metal

capped ends are functionalized with ssDNA sticky-ends. The functionalization yield and the availability of the ssDNA for further manipulations is tested by hybridizing the nanorods to Au NPs coated with the complementary ssDNA or to substrates patterned with Au features functionalized with the complementary ssDNA.

The semiconducting nanorods are made of cadmium sulfide (CdS), they have an average length 60 nm and they are capped with Au at the extremities. They were received from Taleb Mokari's lab [172] in a chloroform solution with tetradecylphosponic acid and dodecylamine (organic) ligands (Fig. 4.18). The oleylamine is displaced in a biphasic ligand exchange reaction to give water soluble particles capped with 11-mercaptoundecanoic acid (MUA).

Once in DI water, two strategies are applied to functionalize the nanorods with ssDNA:

- Ligand exchange with thiol-ssDNA
- Amidation of the carboxyl MUA terminations with amine-ssDNA

It is worth noting that the first approach, the one relying on a thiol exchange, should preferentially functionalize the tips of the nanorods, because of the different affinity that thiol groups have with Au and with CdS [173]. On the other hand, the second approach, relying on the amidation of the ligands terminations, produces a uniform functionalization of the nanorods.

Functionalization with dsDNA with a ssDNA sticky-end is attempted as well, with both approaches. The dsDNA portion confers higher rigidity to the strand,

increasing the chances of hybridization with the complementary ssDNA.

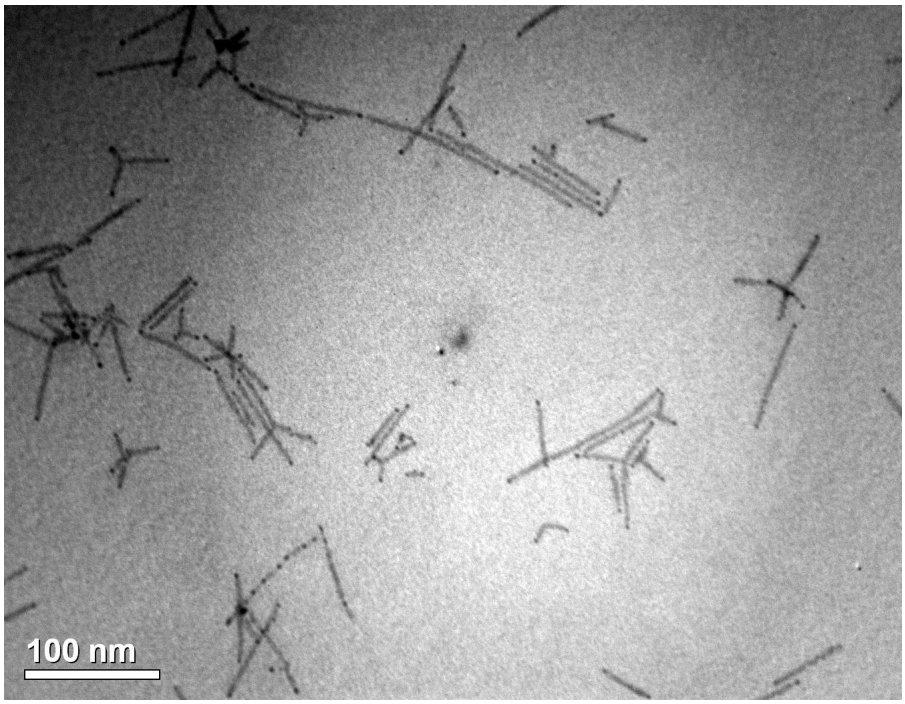

Figure 4.18: TEM image of CdS nanorods with nominal length 60 nm and ends capped with Au, deposited from a chloroform solution.

4.5.1 Experimental methods

The oleylamine-capped CdS nanorods in chloroform are mixed (1:1 volume ratio) to a water solution of ~50 mM tetrabutylammonium hydroxide (TAH) and of ~10 mM 11-mecaptoundecanoic acid (MUA). (Both chemicals are purchased from Sigma-Aldrich). This solution is stirred overnight to allow the nanorods to transfer from the chloroform to the water, as indicated by the change to a red color. The water-soluble nanorods are then decanted and allowed to continue the exchange process for up to 120 hours. Excess ligand is removed through

successive centrifugal filtrations in DI water using Amicon Ultra-15 Centrifugal filter tubes with 10,000 MWCO cellulose membrane.

In order to functionalize the nanorods with ssDNA through a thiol-exchange reaction, thiol-functionalized ssDNA (10 adenines with a thiol modification on the 3' side) or dsDNA (15 base pair double strand with a thiol modification on the 3' side and 8 adenines on the 5' side) is added to the purified nanorods DI water solution that is previously mixed, 1:1 by volume, to DPBS, to give a final DNA concentration of ~9 μM. The reaction is allowed to run overnight, and then the excess ligands are removed, as described above, with DPBS instead of DI water.

As an alternate method to DNA-functionalize the nanorods, the carboxyl terminations of the MUA ligands are activated for 30 minutes in a 0.1 M MES buffer with 2 mM EDC and 5 mM sulfo-NHS followed by the addition of amine-functionalized ssDNA (20 thymines with an amine modification on the 3' side) or dsDNA (10 base pair double strand with an amine modification on the 3' side and 10 thyimines on the 5' side) at ~9 μM final concentration. The reaction is allowed to run overnight, and then the excess ligands are removed using DPBS.

After purification, both solutions are separately mixed with Au NPs coated with the complementary ssDNA: poly-thymine (15T) coated, 5 nm in diameter for nanorods functionalized through thiol exchange; poly-adenine (20A) coated, 10 nm in diameter for nanorods functionalized through amide linkage. The NP concentration is ~5 nM, either in 1X DPBS or I 1X DPBS with 10 mM $MgCl_2$ (to

increase the hybridization probability). They are left to react overnight at room temperature prior TEM imaging (JEOL JEM-100CX). For TEM imaging, 5 μl of nanorods-NPs solution are deposited on amorphous carbon TEM grids (Ted Pella). After drying they are washed with 40 μl of DI water and fully dried in air or vacuum.

The DNA-functionalized nanorods are also incubated onto substrates with ssDNA functionalized pre-patterned Au features. In this case the substrate functionalization is done as explained in 2.3.2 and the nanorods are incubated for 4 hours, in humidified environment at room temperature, followed by ethanol/DI water wash (10 seconds in 50% ethanol 50% DI water, then 50 minutes in 90% ethanol 10% DI water). The samples are imaged with SEM and AFM.

4.5.2 Results and discussion

For ssDNA-functionalized nanorods, selective attachment to pre-patterned surfaces or NPs in solution is not found to be successful. Figure 4.19 shows TEM images of nanorods functionalized with ssDNA through thiol exchange (a) and amidation (b) and of nanorods functionalized with dsDNA with a sticky-end through thiol exchange (c) and amidation (d) and incubated with Au NPs functionalized with the complementary ssDNA. In (a) nanorods and NPs form separate aggregations while in (c) more mixing is observed. In general though, the expected attachment of NPs to the nanorods ends is not observed, and the

result is not much different from the outcome of a control experiment in which the nanorods are not DNA functionalized (Fig. 4.20). (b) and (d) show a somehow higher degree of mixing between the NPs and the nanorods, suggesting that the amidation reaction has higher yield than the thiol exchange.

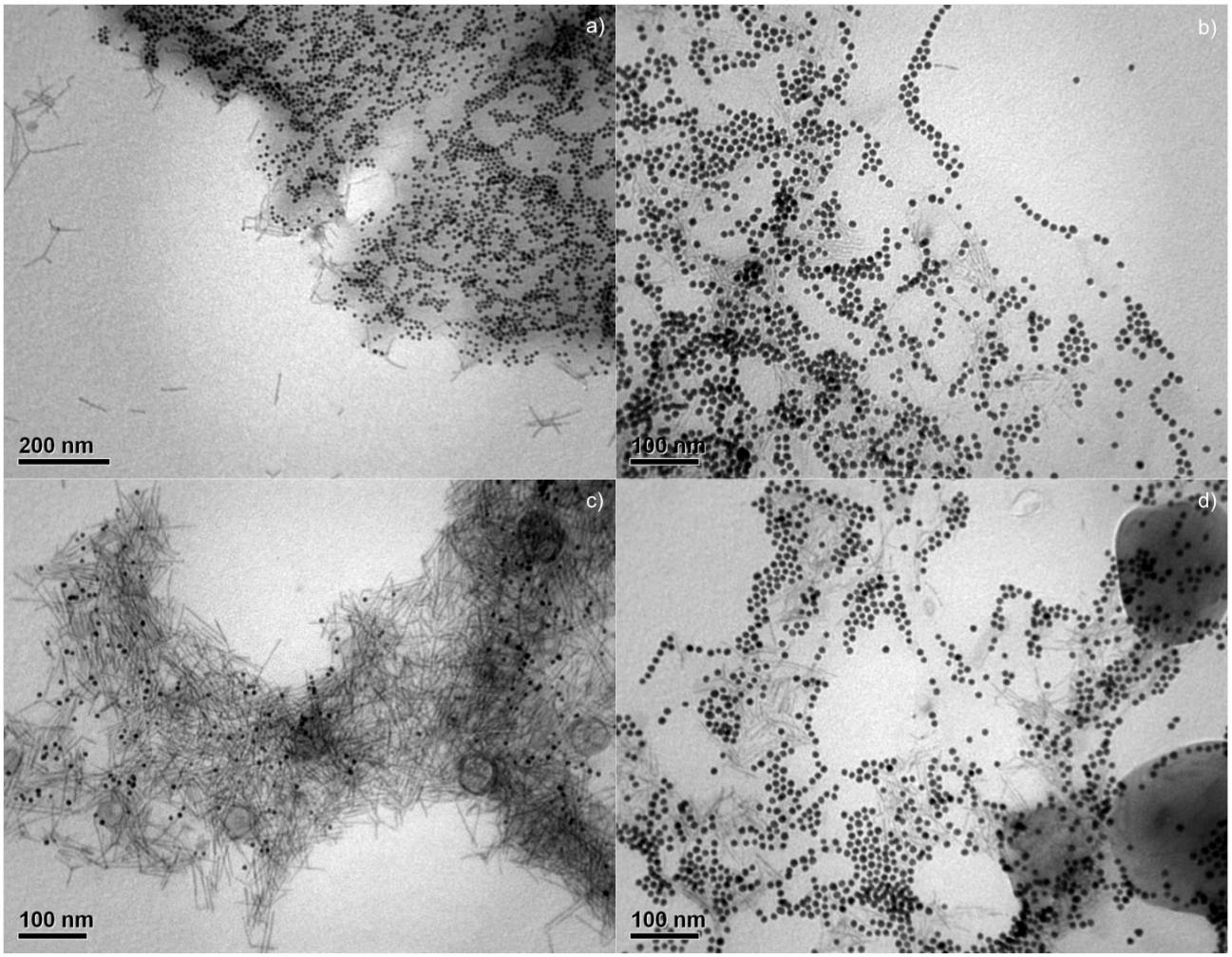

Figure 4.19: TEM images of DNA-functionalized nanorods after incubation with NPs coated with the complementary ssDNA. (a) Nanorods functionalized with ssDNA through thiol exchange. (b) Nanorods functionalized with ssDNA through amidation of the MUA carboxyl terminations. (c) Nanorods functionalized with dsDNA with a sticky-end through thiol exchange. (b) Nanorods functionalized with dsDNA with a sticky-end through amidation of the MUA carboxyl terminations.

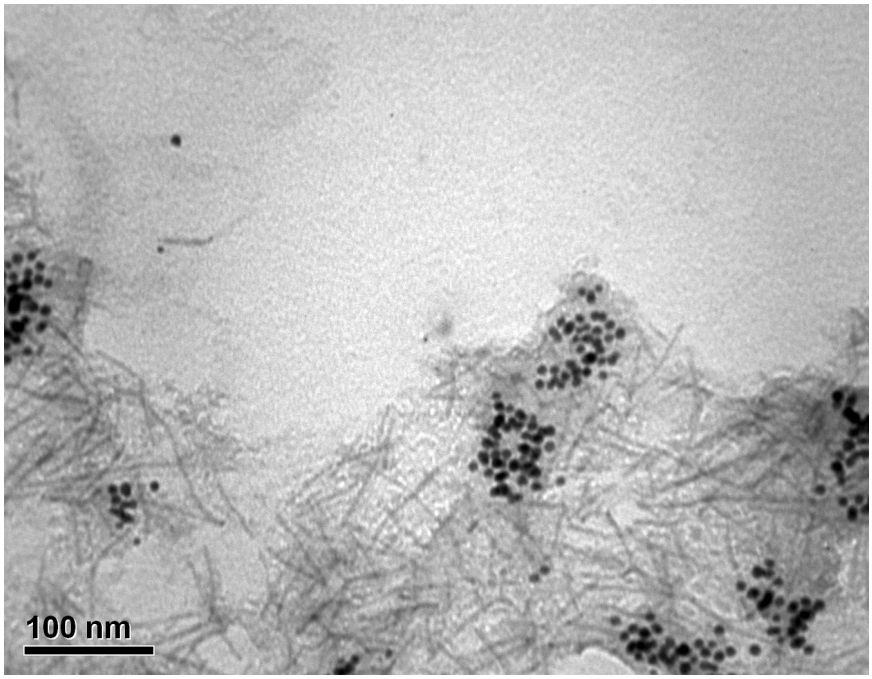

Figure 4.20: Control experiment in which non-DNA functionalized nanorods are incubated with ssDNA coated NPs. The two nanostructures mostly form separate aggregations.

As an attempt to increase the attachment between the DNA functionalized nanorods and the complementary DNA functionalized NPs, the hybridization is carried out in PBS with 10 mM Mg^{2+}. The result is displayed in the TEM image in Figure 4.21. The Mg^{2+} ions don't seem to improve the hybridization yield (comparing to 4.18 (c)) confirming that the main issue is probably the low degree of DNA functionalization achieved by thiol exchange.

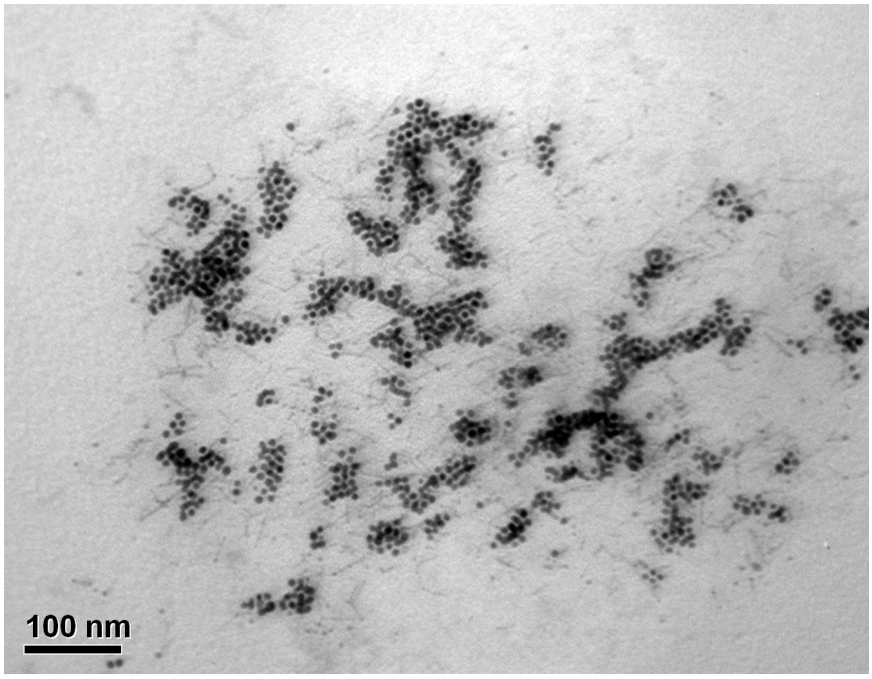

Figure 4.21: TEM images of nanorods functionalized with dsDNA with a sticky-end, through thiol exchange, and incubated with NPs coated with the complementary ssDNA in PBS with 10 mM Mg^{2+}.

A further proof of the poor functionalization of the nanorods is displayed in Fig. 4.22, in which Si substrates with patterned Au features functionalized with ssDNA are incubated with nanorods functionalized with the complementary ssDNA. No preferential binding of the nanorods to the Au is observed. The nanorods seem to mostly aggregate or are washed away (compare with figure 2.34 in which CNT visibly bind to functionalized Au features).

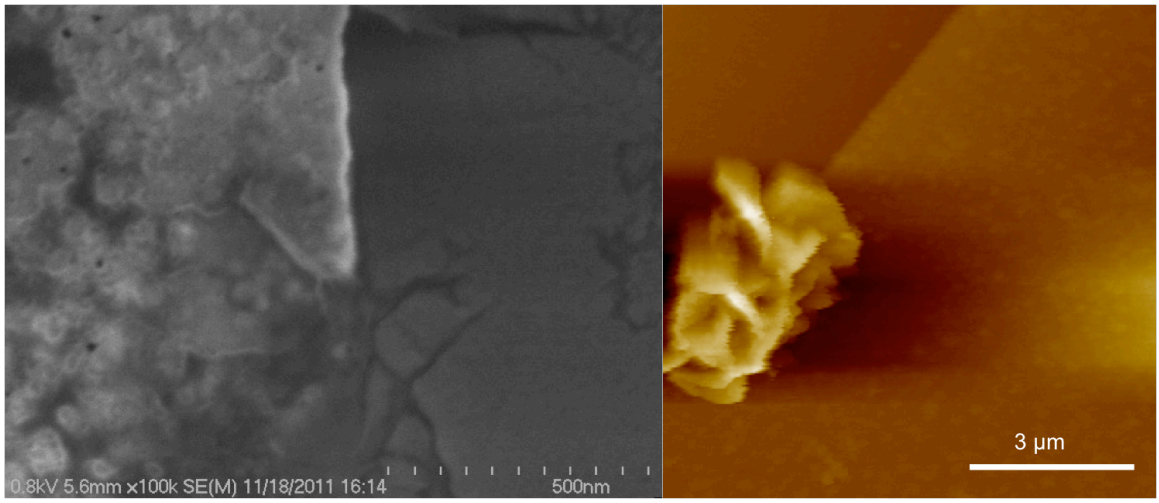

Figure 4.22: SEM image (left) and AFM image (right) of Si substrates with patterned Au features functionalized with ssDNA trough a thiol linkage, and incubated with nanorods functionalized with the complementary DNA. The nanorods are functionalized with dsDNA with a sticky-end by thiol exchange.

4.6 Electrical measurements

In this section SWCNT-dsDNA-SWCNT hybrids synthesized by the two steps reaction described in 4.3.3 are deposited on hard substrates and electrically probed. Two different methods are used, but only one gives a successful outcome. In the first approach, developed by the Porath lab at Hebrew University, Jerusalem, SWCNT-dsDNA complexes are deposited on mica and contacted on one side with a sharp electrode evaporated through an electrostatically clamped hard mask, and on the other side through conductive AFM (cAFM). The second method applies the directed assembly techniques developed in chapter 3 to create arrays of molecular devices. While the first

process allows great control of the measurement (it directly visualizes the nanostructure that's being probed) and allows measurement at different positions along the length of the molecule, the second approach is capable of producing thousands of devices in parallel, thereby providing much larger amount of data, and allows three-terminal measurements through the application of a gate potential, a critical factor not always implemented in molecular devices. The main problem encountered with this second approach is the lack of good electrical contact between the SWCNT and the electrodes, which ultimately prevents the probing of the DNA molecule.

4.6.1 Conductive AFM electrical measurements

SWCNT-dsDNA-SWCNT hybrids synthesized by the two steps reaction described in 4.3.3 are contacted on one side with a sharp electrode evaporated through an electrostatically clamped hard mask, and on the other side through cAFM (Fig. 4.23). The SWCNT-dsDNA complexes are deposited on an insulating substrate (muscovite mica) and stencil lithography is used to evaporate a thin uniform metal film on top of the SWCNT portion of the hybrid objects, which acts as a stationary electrode. Being the deposition done through a shadow mask, it does not require the use of resist, solvents or baking processes that would damage the DNA molecule. The choice of mica is due to its insulating properties and atomic flatness, which allow for effective clamping.

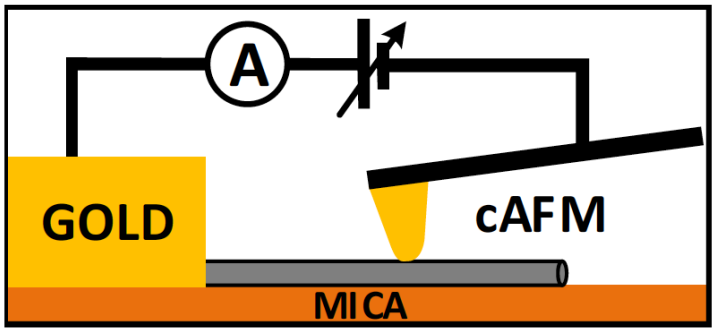

Fig 2.23: Schematic of the conductive AFM electrical measurement. (Figure courtesy of G. Livshits and D. Porath, Hebrew University.)

4.6.2 Sample preparation for conductive AFM electrical measurements

20-30 µl of SWCNT-dsDNA-SWCNT hybrids in 18 mM HEPES with 6.4 mM $MgCl_2$ are deposited on freshly cleaved mica, incubated in humidified atmosphere for 30 min, washed with distilled water and dried with nitrogen, yielding a surface density of ~6-10 molecules/μm^2.

The samples are scanned by AFM (Nanotec Electronica S.L. Madrid, dynamic mode) to verify surface coverage. They are then mounted under a stencil mask and transferred to a thermal evaporator (modified Edwards E306). When the base pressure ~ 2×10^{-6} Torr is reached, a cold trap is cooled down to about -190 °C with liquid nitrogen. To overcome blurring effects, the mask is electrostatically clamped to the substrate (300 V) based on the principles described by Couderc et al. [174]. The sample assembly is cooled by a circulating cooling agent. In the first 30 seconds the temperature drops to

about -11 °C, and then gradually to -25 °C. After temperature stabilization, Au is slowly evaporated (~ 1 Å/min) for 20 min. The evaporation rate is gradually increased by a factor of 2-4 towards the end of the deposition. An 18-35 nm thick layer is evaporated, typically within 60-90 min. The sample is transferred to a sample holder for conductivity measurements in a second AFM system (AIST-NT, SmartSPM™ 1000) equipped with a cAFM module. I-V characteristics are acquired using soft cantilevers (OMCL-RC800PSA, Olympus Optical Co., Ltd) of nominal force constant 0.3 N/m. The cantilevers are sputter-coated with 30-40 nm of Au/Pd, which alters the nominal resonance frequency from 75–80 kHz to 50-60 kHz and the tip radius from 15–20 nm to 30-50 nm (as measured by SEM). For cAFM measurements, a molecule protruding from under the evaporated electrode is located in dynamic mode. The tip is then brought into contact at a desired position. Several force values are attempted before a clear conductance signal appears. The force value is then maintained in all the subsequent measurements on that sample. The images are analyzed using Nanotec Electronica S.L (Madrid) WSxM imaging software [175].

4.6.3 Conductive AFM electrical measurements: results and discussion

A well-known problem in metal deposition through a stencil mask is the penetration of the evaporated metal under the mask. This problem is usually caused by the presence of a gap between the mask and the surface, as shown in

Fig. 4.24 (a) (modified from Vazquez-Mena et al. [176]). Such penetration strongly affects measurement on soft polymers, especially those with a length comparable or shorter than the penetration length, since the surface of the molecules gets covered by metal clusters and atoms, preventing reliable conduction measurements. Electrostatic clamping of the mask to the substrate is used to overcome the restoring mechanical forces responsible for the gap. This produces an electrode with a sharp border and a clean surface beyond the electrode border (Fig. 4.24 (g) and (h)). Figures 4.24 (c)-(f) show the metal penetration when the mask attachment to the surface is loose.

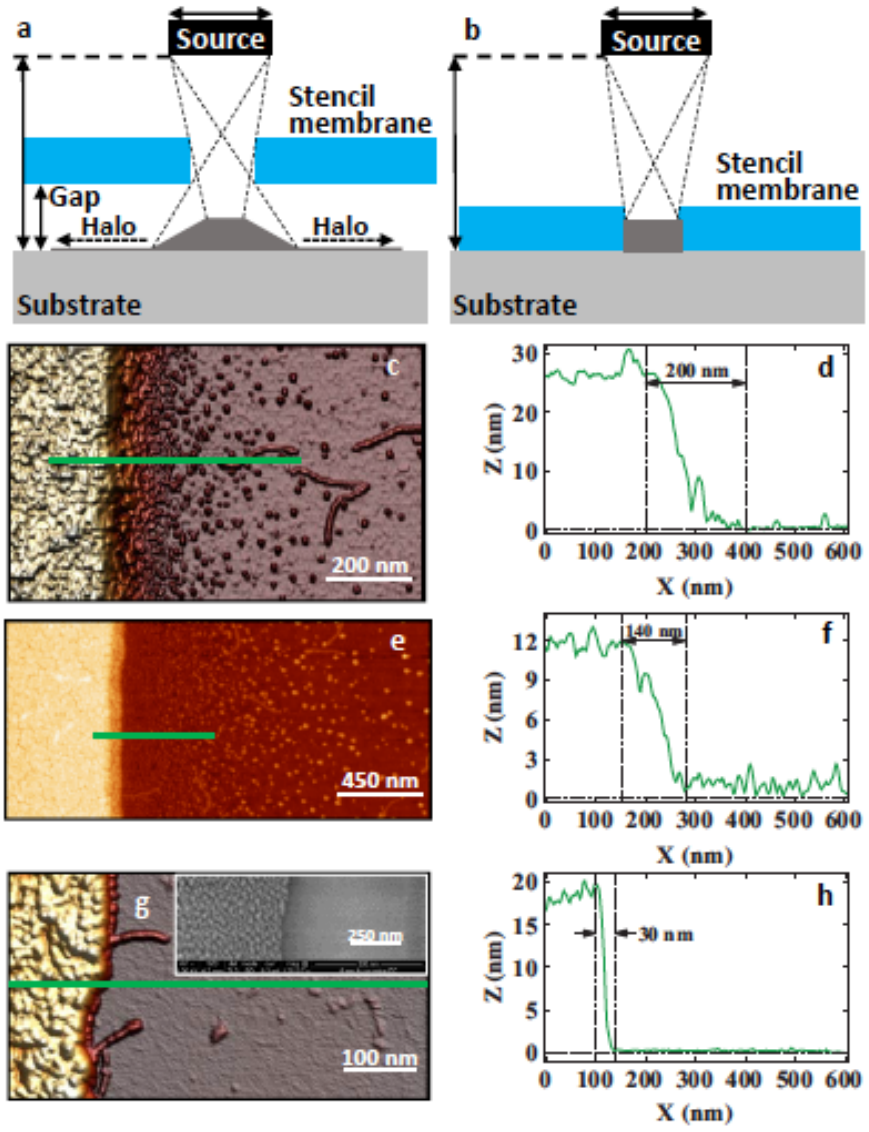

Figure 4.24: Electrode evaporation and metal penetration. (a) The gap between the mask and the substrate allows the evaporated metal to penetrate beyond the border of the aperture. (b) Metal penetration reduced by gap reduction. The gap reduction is obtained by electrostatically clamping the mask to the substrate. (c) and (e) are AFM images of two different samples in which metal penetrated under the mask, which is not well attached to the substrate. The nanostructures near the edge appear to be covered by scattered metal clusters, extending into the mica for hundreds of nanometers. The cross sections along the green lines in (c) and (e) are shown in (d) and (f). (g) AFM image of a sample with a sharp border. Top inset: SEM image of 6 nm of gold evaporated on mica. (h) Cross section along the green line in (g). (Figure courtesy of G. Livshits and D. Porath, Hebrew University.)

Measurements of DNA-wrapped SWCNT give linear I-Vs with resistance equal to the one of the resistor connected in series in order to limit the current through the circuit (Fig. 4.25). Measurements on the Au electrode give the same value of resistance (~18 MΩ). This ohmic contact is not always achieved and, in some cases, SWCNT that looked covered by the Au electrode conducted no current. A typical DNA-wrapped SWCNT profile is displayed in Fig. 4.25 as well.

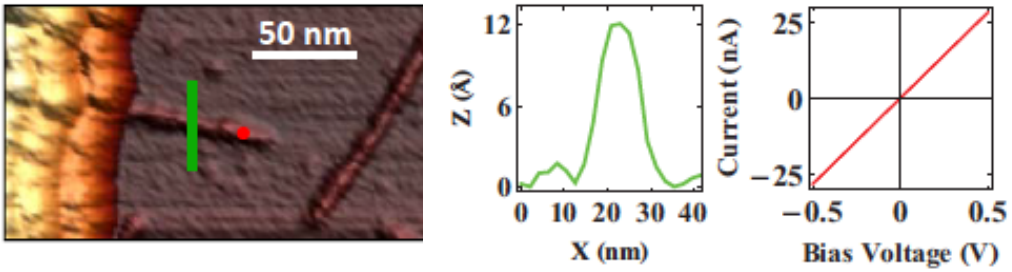

Figure 4.25: (Left) AFM image of DNA-wrapped SWCNT adsorbed on a mica substrate. One SWCNT is protruding from under an evaporated Au electrode. (Center) The SWCNT height profile is measured along the green segment and displayed in the green curve. (Right) Linear I-V curve measured 60 nm from the border (red dot in the AFM image). The slope yields the resistance of the current limiting series resistor (~18 MΩ). (Figure courtesy of G. Livshits and D. Porath, Hebrew University.)

When measurements are performed on a SWCNT-dsDNA hybrid structure protruding from underneath an evaporated Au electrode, the I-V curves are non-linear with a gap of ~ 0.4 – 0.5 V. The size of the gap and slope of the curve depend on the distance of the AFM from the electrode. Measurements on mica show no current while measurements on Au give linear I-V curves with slope

equal to the resistance of the resistor connected in series to limit the current through the circuit (in this case ~100 MΩ).

In general measurements result in different electric behaviors:

- Open circuit, probably reflecting bad contact with the Au electrode.
- Linear I-Vs with resistance equal to the one of the series resistor or bigger. The first case probably corresponds to measurements on DNA-wrapped SWCNT segments well contacted by both the evaporated Au electrode and the metal coated AFM tip. The second case probably corresponds to partial connection between the DNA-wrapped SWCNT segments, the evaporated Au electrode and the metal coated AFM tip. It could reflect the effect of an extra series resistance made by the DNA wrapping around the SWCNT. (As specified in chapter 2, the DNA wrapping around the nanotube has a periodicity of ~25 nm, leaving thus a vast part of the SWCNT uncovered.)
- Nonlinear I-Vs, with a gap of ~ 0.4 – 0.5 V. This is probably the case of a well connected SWCNT-dsDNA hybrid structure and it likely represents the I-V of the dsDNA molecule itself.

4.6.2 Electrical measurements through directed assembly

The dsDNA-SWCNT hybrid structures synthesized with the method explained in section 4.3 are well suited for directed deposition on pre-patterned electrodes applying the process described in chapter 3. In section 3.3 two methods are detailed, one involving patterning electrodes on top of SWCNTs, the other comprising the deposition of SWCNTs on top of electrodes. While the first method allows the formation of a better electrical contact, the second method is preferable when the final goal is to electrically probe a biomolecule like DNA. Indeed the patterning of electrodes necessitates a number of processes (deposition of resist, solvent treatments, high temperature produced by the e-beam deposition of metal, etc.) that would probably damage the biomolecule. On the other hand, for the deposition on top of electrodes none of these treatments is necessary after the dsDNA-SWCNT hybrids are deposited on the sample, since the assembly is done at the end, after all the lithographic steps. The main obstacle encountered in the application of this second method to the probing of the dsDNA-SWCNT structures is that, as explained in section 3.4, the deposition of DNA-wrapped SWCNT on top of electrodes does not result in a sufficient electrical connection. No electrical current is measured unless the SWCNTs are treated with a strong acid and high temperatures (boiling water and annealing at 350 °C) which are both procedures that would irremediably damage the dsDNA connected to the SWCNTs.

One possible solution, that will be tested soon, is to pre-pattern four Au electrodes instead of two, so that each SWCNT segment attached to the dsDNA

is connected to two of them. A high bias (some volts) can be applied separately to each couple of electrodes, in a way to obtain locally a partial removal of the DNA wrapping around the tube, and possibly a better contact.

Chapter 5

Conclusion

A key goal of Nanoscience and Nanotechnology is the control and manipulation of matter at nanoscale dimensions in order to (a) understand their properties and (b) use them to build devices and systems that will benefit the world at large. Nanoscience and Nanotechnology evolved from many disparate fields, and major advances can come from combining materials and features from different fields toward achieving these goals. In this work, tools that were originally developed by the semiconductor industry are combined with processes and materials typically found in chemistry and biochemistry laboratories in order to organize functional nanostructures into arbitrarily large arrays on a surface, with the purpose of constructing nanoscale devices. The nanostructures studied here include DNA molecules, proteins (streptavidins), DNA nanostructures (a double crossover 1D motif and DNA origami) and DNA-wrapped SWCNT segments, which are precisely organized onto surfaces pre-patterned by lithographic methods. By means of selectively functionalized metallic nanodots that are used as anchors, or by the selective modulation of local surface energy, individual nano-objects are deposited from solution, making them individually addressable for further manipulations. One example

of such scheme isolates dsDNA molecules on metallic nanoposts, and enables the visualization of their interaction with a restriction enzyme achieving single molecule resolution. In another case, SWCNTs of selected chirality are deposited from solution into single nanotube three terminal devices.

Another accomplishment of this work is the implementation a model system for the study of polyvalent interactions, by means of a rigid DNA nanostructure (DFX DNA) with specific binding points that interact with complementarily functionalized nanodots precisely arranged on a surface. The thermodynamics of binding is studied and compared to the results of the experiments.

Biomolecular interactions are also used to drive the assembly of multi-component nano-objects in solution, resulting in the formation of molecular junctions that can be electrically probed. Specifically, dsDNA-SWCNT heterostructures are probed by contact AFM.

While the techniques developed in this thesis display many strengths, namely the high resolution, the specificity, the programmability and the fact of working in parallel, which makes them fast end economical, some problems are encountered as well. The main hurdle has appeared to be the sensitivity of these processes to a variety of conditions (e.g., ambient conditions, such as temperature and humidity, and small amounts of contaminants) that are difficult to isolate and to control (this has led to a high degree of variability in the processes, which in turn has hindered the assessment of the success of each approach). One example of these issues is found in the directed placement

of DNA-wrapped SWCNT segments onto functionalized nanodot-anchors described in section 2.7. Many attempts were made to contact the assembled SWCNT segments to obtain three terminal devices, but the assembly was found to be so irregular and unpredictable that a functioning device was never achieved and, mainly because of time constrains, the task was, at least temporarily, set aside.

Rendering the directed assembly processes reliable and deterministic will definitely need a thorough study of the factors influencing their outcome, so that they can be controlled and aimed towards the specific goals of the case.

Despite the problems, plans for future work include the fabrication of carbon nanotube based electronic circuits by directed assembly, and the realization of molecular devices by linking single molecules to SWCNT in solution, and employing the SWCNT as electrodes, after selective deposition by directed assembly.

However, the applicability of the methods described in this thesis goes far beyond these two projects. Many studies in fields such as chemistry and biology necessitates of single molecule resolution. In addition, the approaches developed in this work may facilitate the advancement of new electronics technologies, including, but not limited to, future circuits based on single-wall carbon nanotubes with specific electronic properties.

Bibliography

1. Burda, C., et al., *Chemistry and properties of nanocrystals of different shapes.* Chemical Reviews, 2005. **105**(4): p. 1025-1102.

2. Xia, Y.N., et al., *One-dimensional nanostructures: Synthesis, characterization, and applications.* Advanced Materials, 2003. **15**(5): p. 353-389.

3. Watson, J. and F. Crick, *Molecular structure of nucleic acids; a structure for deoxyribose nucleic acid.* Nature, 1953. **171**(4356): p. 737-738.

4. Goodchild, J., *Conjugates of oligonucleotides and modified oligonucleotides: a review of their synthesis and properties.* Bioconjugate chemistry, 1990. **1**(3): p. 165-187.

5. Nielsen, P., et al., *Sequence-selective recognition of DNA by strand displacement with a thymine-substituted polyamide.* Science (New York, N.Y.), 1991. **254**(5037): p. 1497-1500.

6. Singh, S.K., et al., *LNA (locked nucleic acids): synthesis and high-affinity nucleic acid recognition.* Chemical Communications, 1998(4): p. 455-456.

7. Itakura, K., J. Rossi, and R. Wallace, *Synthesis and use of synthetic oligonucleotides.* Annual review of biochemistry, 1984. **53**: p. 323-356.

8. Boon, E., et al., *Mutation detection by electrocatalysis at DNA-modified electrodes.* Nature biotechnology, 2000. **18**(10): p. 1096-1100.

9. Evans, R., J. Johnson, and B. Haley, *5-Azido-2'-deoxyuridine 5'-triphosphate: a photoaffinity-labeling reagent and tool for the enzymatic synthesis of photoactive DNA.* Proceedings of the National Academy of Sciences of the United States of America, 1986. **83**(15): p. 5382-5386.

10. Seeman, N., *Nucleic acid junctions and lattices.* Journal of theoretical biology, 1982. **99**(2): p. 237-247.

11. Ofer, I.W. and W. Itamar, *Functionalized DNA Nanostructures.* Chemical Reviews, 2012. **112**.

12. Winfree, E., et al., *Design and self-assembly of two-dimensional DNA crystals.* Nature, 1998. **394**(6693): p. 539-544.

13. Fu, T. and N. Seeman, *DNA double-crossover molecules.* Biochemistry, 1993. **32**(13): p. 3211-3220.

14. LaBean, T.H., et al., *Construction, Analysis, Ligation, and Self-Assembly of DNA Triple Crossover Complexes.* Journal of the American Chemical Society, 2000. **122**(9): p. 1848-1860.

15. Zheng, J., et al., *From molecular to macroscopic via the rational design of a self-assembled 3D DNA crystal.* Nature, 2009. **461**(7260): p. 74-77.

16. Wilner, O.I. and I. Willner, *Functionalized DNA nanostructures.* Chem Rev, 2012. **112**(4): p. 2528-56.

17. Rothemund, P., *Folding DNA to create nanoscale shapes and patterns.* Nature, 2006. **440**(7082): p. 297-302.

18. (a) www.cdna.dk/origami (b) http://cadnano.org/.

19. Andersen, E., et al., *Self-assembly of a nanoscale DNA box with a controllable lid.* Nature, 2009. **459**(7243): p. 73-76.

20. Douglas, S., et al., *Self-assembly of DNA into nanoscale three-dimensional shapes.* Nature, 2009. **459**(7245): p. 414-418.

21. Ke, Y., et al., *Multilayer DNA origami packed on a square lattice.* Journal of the American Chemical Society, 2009. **131**(43): p. 15903-15908.

22. Dietz, H., S. Douglas, and W. Shih, *Folding DNA into twisted and curved nanoscale shapes.* Science (New York, N.Y.), 2009. **325**(5941): p. 725-730.

23. Han, D., et al., *DNA origami with complex curvatures in three-dimensional space.* Science (New York, N.Y.), 2011. **332**(6027): p. 342-346.

24. Wei, B., M. Dai, and P. Yin, *Complex shapes self-assembled from single-stranded DNA tiles.* Nature, 2012. **485**(7400): p. 623-626.

25. Xiao, S.J., et al., *Selfassembly of metallic nanoparticle arrays by DNA scaffolding.* Journal of Nanoparticle Research, 2002. **4**(4): p. 313-317.

26. Le, J.D., et al., *DNA-templated self-assembly of metallic nanocomponent arrays on a surface.* Nano Letters, 2004. **4**(12): p. 2343-2347.

27. Zheng, J., et al., *Two-dimensional nanoparticle arrays show the organizational power of robust DNA motifs.* Nano letters, 2006. **6**(7): p. 1502-1504.

28. He, Y., et al., *Antibody nanoarrays with a pitch of approximately 20 nanometers.* Journal of the American Chemical Society, 2006. **128**(39): p. 12664-12665.

29. Yan, H., et al., *DNA-templated self-assembly of protein arrays and highly conductive nanowires.* Science (New York, N.Y.), 2003. **301**(5641): p. 1882-1884.

30. Selmi, D., et al., *DNA-templated protein arrays for single-molecule imaging.* Nano letters, 2011. **11**(2): p. 657-660.

31. Ding, B., et al., *Gold nanoparticle self-similar chain structure organized by DNA origami.* Journal of the American Chemical Society, 2010. **132**(10): p. 3248-3249.

32. Bui, H., et al., *Programmable periodicity of quantum dot arrays with DNA origami nanotubes.* Nano letters, 2010. **10**(9): p. 3367-3372.

33. Wang, R., C. Nuckolls, and S. Wind, *Assembly of heterogeneous functional nanomaterials on DNA origami scaffolds.* Angewandte Chemie (International ed. in English), 2012. **51**(45): p. 11325-11327.

34. Maune, H., et al., *Self-assembly of carbon nanotubes into two-dimensional geometries using DNA origami templates.* Nature nanotechnology, 2010. **5**(1): p. 61-66.

35. Rinker, S., et al., *Self-assembled DNA nanostructures for distance-dependent multivalent ligand-protein binding.* Nature nanotechnology, 2008. **3**(7): p. 418-422.

36. Voigt, N., et al., *Single-molecule chemical reactions on DNA origami.* Nature nanotechnology, 2010. **5**(3): p. 200-203.

37. Wilner, O., et al., *Enzyme cascades activated on topologically programmed DNA scaffolds.* Nature nanotechnology, 2009. **4**(4): p. 249-254.

38. Niemeyer, C., J. Koehler, and C. Wuerdemann, *DNA-directed assembly of bienzymic complexes from in vivo biotinylated NAD(P)H:FMN oxidoreductase and luciferase.* Chembiochem : a European journal of chemical biology, 2002. **3**(2-3): p. 242-245.

39. Sönnichsen, C., et al., *A molecular ruler based on plasmon coupling of single gold and silver nanoparticles.* Nature biotechnology, 2005. **23**(6): p. 741-745.

40. Maye, M., et al., *Stepwise surface encoding for high-throughput assembly of nanoclusters.* Nature materials, 2009. **8**(5): p. 388-391.

41. Cheng, W., et al., *Free-standing nanoparticle superlattice sheets controlled by DNA.* Nature materials, 2009. **8**(6): p. 519-525.

42. Park, S., et al., *DNA-programmable nanoparticle crystallization.* Nature, 2008. **451**(7178): p. 553-556.

43. Nykypanchuk, D., et al., *DNA-guided crystallization of colloidal nanoparticles.* Nature, 2008. **451**(7178): p. 549-552.

44. ITRS roadmap:http://www.itrs.net/Links/2012ITRS/Home2012.htm

45. Braun, E., et al., *DNA-templated assembly and electrode attachment of a conducting silver wire.* Nature, 1998. **391**(6669): p. 775-778.

46. Keren, K., et al., *DNA-templated carbon nanotube field-effect transistor.* Science (New York, N.Y.), 2003. **302**(5649): p. 1380-1382.

47. Richter, J., et al., *Construction of highly conductive nanowires on a DNA template.* Applied Physics Letters, 2001. **78**(4): p. 536.

48. Dong, L., et al., *DNA-Templated Semiconductor Nanoparticle Chains and Wires.* Advanced Materials, 2007. **19**.

49. Genereux, J. and J. Barton, *Mechanisms for DNA charge transport.* Chemical reviews, 2010. **110**(3): p. 1642-1662.

50. Endres, R., D. Cox, and R. Singh, *Colloquium: The quest for high-conductance DNA.* Reviews of Modern Physics, 2004. **76**(1): p. 195.

51. Guo, X., et al., *Conductivity of a single DNA duplex bridging a carbon nanotube gap.* Nat Nanotechnol, 2008. **3**(3): p. 163-7.

52. Dresselhaus, M.S., G. Dresselhaus, and R. Saito, *Physics of carbon nanotubes.* Carbon, 1995. **33**.

53. Anantram, M.P. and F. Léonard, *Physics of carbon nanotube electronic devices.* Reports on Progress in Physics, 2006. **69**.

54. Charlier, J.-C. and S. Roche, *Electronic and transport properties of nanotubes.* Reviews of Modern Physics, 2007. **79**(2): p. 677-732.

55. Avouris, P., Z. Chen, and V. Perebeinos, *Carbon-based electronics.* Nature nanotechnology, 2007. **2**(10): p. 605-615.

56. Dresselhaus, M., et al., *Electronic, thermal and mechanical properties of carbon nanotubes.* Philosophical transactions. Series A, Mathematical, physical, and engineering sciences, 2004. **362**(1823): p. 2065-2098.

57. Dresselhaus, M., G. Dresselhaus, and S. Riichiro, *Carbon fibers based on C60 and their symmetry.* Physical Review B, 1992. **45**.

58. Mintmire, J.W., B.I. Dunlap, and C.T. White, *Are fullerene tubules metallic?* Physical Review Letters, 1992. **68**.

59. Avouris, P., et al., *Carbon nanotube optoelectronics.* Physica Status Solidi B-Basic Solid State Physics, 2006. **243**(13): p. 3197-3203.

60. Imry, Y. and R. Landauer, *Conductance viewed as transmission.* Reviews of Modern Physics, 1999. **71**(2): p. S306-S312.

61. Avouris, P., et al., *Carbon nanotube electronics.* Proceedings of the IEEE, 2003. **9**.

62. Javey, A., et al., *Ballistic carbon nanotube field-effect transistors.* Nature, 2003. **424**(6949): p. 654-657.

63. Wind, S., J. Appenzeller, and P. Avouris, *Lateral Scaling in Carbon-Nanotube Field-Effect Transistors.* Physical Review Letters, 2003. **91**(5).

64. Ando, T. and T. Nakanishi, *Impurity scattering in carbon nanotubes - Absence of back scattering.* Journal of the Physical Society of Japan, 1998. **67**(5): p. 1704-1713.

65. Dürkop, T., et al., *Extraordinary Mobility in Semiconducting Carbon Nanotubes.* Nano Letters, 2004. **4**.

66. Perebeinos, V., J. Tersoff, and P. Avouris, *Radiative lifetime of excitons in carbon nanotubes.* Nano letters, 2005. **5**(12): p. 2495-2499.

67. Zhou, X.J., et al., *Band structure, phonon scattering, and the performance limit of single-walled carbon nanotube transistors.* Physical Review Letters, 2005. **95**(14).

68. Yao, Z., C.L. Kane, and C. Dekker, *High-field electrical transport in single-wall carbon nanotubes.* Physical Review Letters, 2000. **84**(13): p. 2941-2944.

69. Javey, A., et al., *Carbon nanotube field-effect transistors with integrated ohmic contacts and high-k gate dielectrics.* Nano Letters, 2004. **4**(3): p. 447-450.

70. Chen, Y.F. and M.S. Fuhrer, *Electric-field-dependent charge-carrier velocity in semiconducting carbon nanotubes.* Physical Review Letters, 2005. **95**(23).

71. Ilani, S., et al., *Measurement of the quantum capacitance of interacting electrons in carbon nanotubes.* Nature Physics, 2006. **2**.

72. Burke, P.J., *AC performance of nanoelectronics: towards a ballistic THz nanotube transistor.* Solid-State Electronics, 2004. **48**(10-11): p. 1981-1986.

73. Tans, S., A. Verschueren, and C. Dekker, *Room-temperature transistor based on a single carbon nanotube.* Nature, 1998.

74. Martel, R., et al., *Single- and multi-wall carbon nanotube field-effect transistors.* Applied Physics Letters, 1998. **73**.

75. Heinze, S., et al., *Carbon Nanotubes as Schottky Barrier Transistors.* Physical Review Letters, 2002. **89**.

76. Chen, Z., et al., *The role of metal-nanotube contact in the performance of carbon nanotube field-effect transistors.* Nano letters, 2005. **5**(7): p. 1497-1502.

77. Javey, A., et al., *High performance n-type carbon nanotube field-effect transistors with chemically doped contacts.* Nano letters, 2005. **5**(2): p. 345-348.

78. Lin, Y.M., et al., *High-Performance Carbon Nanotube Field-Effect Transistor With Tunable Polarities.* IEEE transactions on nanotechnology, 2005. **4**(5): p. 481-489.

79. Franklin, A., et al., *Sub-10 nm carbon nanotube transistor.* Nano letters, 2012. **12**(2): p. 758-762.

80. Javey, A., et al., *High-kappa dielectrics for advanced carbon-nanotube transistors and logic gates.* Nature materials, 2002. **1**(4): p. 241-246.

81. Chen, Z., et al., *Externally Assembled Gate-All-Around Carbon Nanotube Field-Effect Transistor.* IEEE electron device letters, 2008. **29**(2): p. 183-185.

82. Appenzeller, J., et al., *Band-to-band tunneling in carbon nanotube field-effect transistors.* Physical review letters, 2004. **93**(19): p. 196805.

83. Chen, Z., et al., *An integrated logic circuit assembled on a single carbon nanotube.* Science (New York, N.Y.), 2006. **311**(5768): p. 1735.

84. Ebbesen, T.W. and P.M. Ajayan, *Large-scale synthesis of carbon nanotubes.* Nature, 1992. **358**.

85. Guo, T., et al., *Catalytic growth of single-walled manotubes by laser vaporization.* Chemical Physics Letters, 1995. **243**.

86. Endo, M., et al., *THE PRODUCTION AND STRUCTURE OF PYROLYTIC CARBON NANOTUBES (PCNTS).* Journal of Physics and Chemistry of Solids, 1993. **54**(12): p. 1841-1848.

87. Hersam, M., *Progress towards monodisperse single-walled carbon nanotubes.* Nature nanotechnology, 2008. **3**(7): p. 387-394.

88. Zheng, M., et al., *DNA-assisted dispersion and separation of carbon nanotubes.* Nature materials, 2003. **2**(5): p. 338-342.

89. Huang, X., R. McLean, and M. Zheng, *High-resolution length sorting and purification of DNA-wrapped carbon nanotubes by size-exclusion chromatography.* Analytical chemistry, 2005. **77**(19): p. 6225-6228.

90. Tu, X., et al., *DNA sequence motifs for structure-specific recognition and separation of carbon nanotubes.* Nature, 2009. **460**(7252): p. 250-253.

91. Collins, P., M. Arnold, and P. Avouris, *Engineering carbon nanotubes and nanotube circuits using electrical breakdown.* Science (New York, N.Y.), 2001. **292**(5517): p. 706-709.

92. Collins, P., et al., *Current saturation and electrical breakdown in multiwalled carbon nanotubes.* Physical review letters, 2001. **86**(14): p. 3128-31.

93. Kanungo, M., et al., *Suppression of metallic conductivity of single-walled carbon nanotubes by cycloaddition reactions.* Science (New York, N.Y.), 2009. **323**(5911): p. 234-237.

94. Jin, S., et al., *Using nanoscale thermocapillary flows to create arrays of purely semiconducting single-walled carbon nanotubes.* Nature nanotechnology, 2013. **8**(5): p. 347-355.

95. Hu, H., M. Gopinadhan, and C. Osuji, *Directed self-assembly of block copolymers: a tutorial review of strategies for enabling nanotechnology with soft matter.* Soft matter, 2014.

96. Kim, S.O., et al., *Epitaxial self-assembly of block copolymers on lithographically defined nanopatterned substrates.* Nature, 2003. **424**(6947): p. 411-414.

97. Stoykovich, M., et al., *Directed assembly of block copolymer blends into nonregular device-oriented structures.* Science (New York, N.Y.), 2005. **308**(5727): p. 1442-1446.

98. Cui, Y., et al., *Integration of colloidal nanocrystals into lithographically patterned devices.* Nano Letters, 2004. **4**(6): p. 1093-1098.

99. Malaquin, L., et al., *Controlled particle placement through convective and capillary assembly.* Langmuir : the ACS journal of surfaces and colloids, 2007. **23**(23): p. 11513-11521.

100. Abramson, J., et al., *Quantum dot nanoarrays: self-assembly with single-particle control and resolution.* Adv Mater, 2012. **24**(16): p. 2207-11.

101. Fan, Z., et al., *Wafer-scale assembly of highly ordered semiconductor nanowire arrays by contact printing.* Nano letters, 2008. **8**(1): p. 20-25.

102. Bulyk, M., et al., *Quantifying DNA-protein interactions by double-stranded DNA arrays.* Nature biotechnology, 1999. **17**(6): p. 573-577.

103. Demers, L., et al., *Direct patterning of modified oligonucleotides on metals and insulators by dip-pen nanolithography.* Science (New York, N.Y.), 2002. **296**(5574): p. 1836-1838.

104. Rodolfa, K., et al., *Two-component graded deposition of biomolecules with a double-barreled nanopipette.* Angewandte Chemie (International ed. in English), 2005. **44**(42): p. 6854-6859.

105. Akbulut, O., et al., *Application of supramolecular nanostamping to the replication of DNA nanoarrays.* Nano letters, 2007. **7**(11): p. 3493-3498.

106. Drmanac, R., et al., *Human genome sequencing using unchained base reads on self-assembling DNA nanoarrays.* Science (New York, N.Y.), 2010. **327**(5961): p. 78-81.

107. Kershner, R., et al., *Placement and orientation of individual DNA shapes on lithographically patterned surfaces.* Nature nanotechnology, 2009. **4**(9): p. 557-561.

108. Hung, A.M., et al., *Large-area spatially ordered arrays of gold nanoparticles directed by lithographically confined DNA origami.* Nature Nanotechnology, 2010. **5**(2): p. 121-126.

109. Gerdon, A., et al., *Controlled delivery of DNA origami on patterned surfaces.* Small (Weinheim an der Bergstrasse, Germany), 2009. **5**(17): p. 1942-1946.

110. Yun, J.M., et al., *DNA Origami Nanopatterning on Chemically Modified Graphene.* Angewandte Chemie-International Edition, 2012. **51**(4): p. 912-915.

111. Ding, B., et al., *Interconnecting gold islands with DNA origami nanotubes.* Nano letters, 2010. **10**(12): p. 5065-5069.

112. Pearson, A., et al., *Chemical alignment of DNA origami to block copolymer patterned arrays of 5 nm gold nanoparticles.* Nano letters, 2011. **11**(5): p. 1981-1987.

113. Rao, S., et al., *Nanotube electronics: large-scale assembly of carbon nanotubes.* Nature, 2003. **425**(6953): p. 36-37.

114. Vijayaraghavan, A., et al., *Ultra-large-scale directed assembly of single-walled carbon nanotube devices.* Nano letters, 2007. **7**(6): p. 1556-1560.

115. Park, H., et al., *High-density integration of carbon nanotubes via chemical self-assembly.* Nature nanotechnology, 2012. **7**(12): p. 787-791.

116. Han, S.-p., et al., *DNA-linker-induced surface assembly of ultra dense parallel single walled carbon nanotube arrays.* Nano letters, 2012. **12**(3): p. 1129-1135.

117. Stokes, P. and S.I. Khondaker, *High quality solution processed carbon nanotube transistors assembled by dielectrophoresis.* Applied Physics Letters, 2010. **96**(8).

118. Kang, S., et al., *High-performance electronics using dense, perfectly aligned arrays of single-walled carbon nanotubes.* Nature nanotechnology, 2007. **2**(4): p. 230-236.

119. Ho, X., et al., *Scaling properties in transistors that use aligned arrays of single-walled carbon nanotubes.* Nano letters, 2010. **10**(2): p. 499-503.

120. Cao, Q., et al., *Evaluation of field-effect mobility and contact resistance of transistors that use solution-processed single-walled carbon nanotubes.* ACS nano, 2012. **6**(7): p. 6471-6477.

121. Mammen, M., S.-K. Choi, and G.M. Whitesides, *Polyvalent Interactions in Biological Systems: Implications for Design and Use of Multivalent Ligands and Inhibitors.* Angewandte Chemie International Edition, 1998. **37**(20): p. 2754-2794.

122. Badjić, J., et al., *Multivalency and cooperativity in supramolecular chemistry.* Accounts of chemical research, 2005. **38**(9): p. 723-732.

123. Schvartzman, M. and S. Wind, *Robust pattern transfer of nanoimprinted features for sub-5-nm fabrication.* Nano letters, 2009. **9**(10): p. 3629-3634.

124. Guo, L.J., *Recent progress in nanoimprint technology and its applications.* Journal of Physics D: Applied Physics, 2004. **37**.

125. Hua, F., et al., *Polymer imprint lithography with molecular-scale resolution.* Nano Letters, 2004. **4**(12): p. 2467-2471.

126. Namatsu, H., et al., *Three-dimensional siloxane resist for the formation of nanopatterns with minimum linewidth fluctuations.* Journal of Vacuum Science & Technology B, 1998. **16**(1): p. 69-76.

127. Love, J., et al., *Self-assembled monolayers of thiolates on metals as a form of nanotechnology.* Chemical reviews, 2005. **105**(4): p. 1103-1169.

128. Cherniavskaya, O., et al., *Fabrication and surface chemistry of nanoscale bioarrays designed for the study of cytoskeletal protein binding interactions and their effect on cell motility.* Journal of Vacuum Science & Technology B: Microelectronics and Nanometer Structures, 2005. **23**.

129. Herne, T.M. and M.J. Tarlov, *Characterization of DNA probes immobilized on gold surfaces.* Journal of the American Chemical Society, 1997. **119**(38): p. 8916-8920.

130. Levicky, R., et al., *Using self-assembly to control the structure of DNA monolayers on gold: A neutron reflectivity study.* Journal of the American Chemical Society, 1998. **120**(38): p. 9787-9792.

131. Murphy, J., et al., *On the nature of DNA self-assembled monolayers on Au: measuring surface heterogeneity with electrochemical in situ fluorescence microscopy.* Journal of the American Chemical Society, 2009. **131**(11): p. 4042-4050.

132. Ladd, J., et al., *DNA-directed protein immobilization on mixed self-assembled monolayers via a streptavidin bridge.* Langmuir : the ACS journal of surfaces and colloids, 2004. **20**(19): p. 8090-8095.

133. Smith, C., J. Milea, and G. Nguyen, *Immobilization of nucleic acids using biotin-strept (avidin) systems.* Immobilisation of DNA on Chips II, 2005.

134. Palma, M., et al., *Selective biomolecular nanoarrays for parallel single-molecule investigations.* J Am Chem Soc, 2011. **133**(20): p. 7656-9.

135. Athanasiadis, A., et al., *Crystal structure of PvuII endonuclease reveals extensive structural homologies to EcoRV.* Nature structural biology, 1994. **1**(7): p. 469-475.

136. Lu, H., L. Xun, and X. Xie, *Single-molecule enzymatic dynamics.* Science (New York, N.Y.), 1998. **282**(5395): p. 1877-1882.

137. Xie, F. and C. Dupureur, *Kinetic analysis of product release and metal ions in a metallonuclease.* Archives of biochemistry and biophysics, 2009. **483**(1): p. 1-9.

138. Xie, F., et al., *One- and two-metal ion catalysis: global single-turnover kinetic analysis of the PvuII endonuclease mechanism.* Biochemistry, 2008. **47**(47): p. 12540-12550.

139. Simoncsits, A., et al., *Covalent joining of the subunits of a homodimeric type II restriction endonuclease: single-chain PvuII endonuclease.* Journal of molecular biology, 2001. **309**(1): p. 89-97.

140. Sa-Ardyen, P., A.V. Vologodskii, and N.C. Seeman, *The flexibility of DNA double crossover molecules.* Biophysical Journal, 2003. **84**(6): p. 3829-3837.

141. Wang, R.S., et al., *Lithographically directed assembly of one-dimensional DNA nanostructures via bivalent binding interactions.* Nano Research, 2013. **6**(6): p. 409-417.

142. Seeman, N.C., De novo design of sequences for nucleic-acid structural-engineering. J Biomol Struct Dyn, 1990. 8: p. 573-581.

143. SantaLucia, J. and D. Hicks, *The thermodynamics of DNA structural motifs.* Annual review of biophysics and biomolecular structure, 2004. **33**: p. 415-440.

144. Owczarzy, R., et al., *Stability and mismatch discrimination of locked nucleic acid-DNA duplexes.* Biochemistry, 2011. **50**(43): p. 9352-9367.

145. SantaLucia, J., *A unified view of polymer, dumbbell, and oligonucleotide DNA nearest-neighbor thermodynamics.* Proceedings of the National Academy of Sciences of the United States of America, 1998. **95**(4): p. 1460-1465.

146. Xia, T., et al., *Thermodynamic parameters for an expanded nearest-neighbor model for formation of RNA duplexes with Watson-Crick base pairs.* Biochemistry, 1998. **37**(42): p. 14719-14735.

147. Badia, A., R. Lennox, and L. Reven, *A dynamic view of self-assembled monolayers.* Accounts of chemical research, 2000. **33**(7): p. 475-481.

148. Poirier, G. and M. Tarlov, *Molecular ordering and gold migration observed in butanethiol self-assembled monolayers using scanning tunneling microscopy.* The Journal of Physical Chemistry, 1995.

149. Bucher, J., L. Santesson, and K. Kern, *Thermal healing of self-assembled organic monolayers: hexane-and octadecanethiol on Au (111) and Ag (111).* Langmuir, 1994.

150. Mack, E., et al., *Dependence of avidity on linker length for a bivalent ligand-bivalent receptor model system.* Journal of the American Chemical Society, 2012. **134**(1): p. 333-345.

151. González, M., et al., *Interaction of biotin with streptavidin. Thermostability and conformational changes upon binding.* The Journal of biological chemistry, 1997. **272**(17): p. 11288-94.

152. Kaempgen, M., et al., *Sonochemical Optimization of the Conductivity of Single Wall Carbon Nanotube Networks.* Advanced Materials, 2008. **20**.

153. Riesz, P. and T. Kondo, *Free radical formation induced by ultrasound and its biological implications.* Free radical biology & medicine, 1992. **13**(3): p. 247-270.

154. Penzo, E., et al., *Selective placement of DNA origami on substrates patterned by nanoimprint lithography.* Journal of Vacuum Science & Technology B, 2011. **29**: p. 5.

155. Kershner, R.J., et al., *Placement and orientation of individual DNA shapes on lithographically patterned surfaces.* Nature Nanotechnology, 2009. **4**(9): p. 557-561.

156. Schvartzman, M., et al., *Fluorinated diamondlike carbon templates for high resolution nanoimprint lithography.* Journal of Vacuum Science & Technology B, 2008. **26**(6): p. 2394-2398.

157. Schvartzman, M., et al., *Plasma fluorination of carbon-based materials for imprint and molding lithographic applications.* Applied Physics Letters, 2008. **93**(15): p. -.

158. Rothemund, P.W.K., *Folding DNA to create nanoscale shapes and patterns.* Nature, 2006. **440**(7082): p. 297-302.

159. Khripin, C., J. Fagan, and M. Zheng, *Spontaneous partition of carbon nanotubes in polymer-modified aqueous phases.* Journal of the American Chemical Society, 2013. **135**(18): p. 6822-6825.

160. The assembly yield is found to greatly vary from sample to sample, from nearly 100% to 0%. The reasons for this behavior can be many: from small variations in the lithography to enviromental conditions affecting the chemistry and/or the selectivity of the assembly.

161. Zhang, L., et al., *Assessment of chemically separated carbon nanotubes for nanoelectronics.* Journal of the American Chemical Society, 2008. **130**(8): p. 2686-2691.

162. Zhang, L., et al., *Optical characterizations and electronic devices of nearly pure (10,5) single-walled carbon nanotubes.* Journal of the American Chemical Society, 2009. **131**(7): p. 2454-2455.

163. Park, H., et al., *High-density integration of carbon nanotubes via chemical self-assembly.* Nat Nanotechnol, 2012. **7**(12): p. 787-91.

164. Liu, J., et al., *Chirality-controlled synthesis of single-wall carbon nanotubes using vapour-phase epitaxy.* Nature Communications, 2012. **3**.

165. Palma, M., et al., *Controlled formation of carbon nanotube junctions via linker-induced assembly in aqueous solution.* Journal of the American Chemical Society, 2013. **135**(23): p. 8440-8443.

166. Grimm, D., et al., *Synthesis of SWCNT rings made by two Y junctions and possible applications in electron interferometry.* Small (Weinheim an der Bergstrasse, Germany), 2007. **3**(11): p. 1900-1905.

167. Grimm, D., R. Muniz, and A. Latgé, *From straight carbon nanotubes to Y-shaped junctions and rings.* Physical Review B, 2003. **68**.

168. Cohen, H., et al., *Direct measurement of electrical transport through single DNA molecules of complex sequence.* Proceedings of the National Academy of Sciences of the United States of America, 2005. **102**(33): p. 11589-11593.

169. Guo, X., et al., *Covalently bridging gaps in single-walled carbon nanotubes with conducting molecules.* Science, 2006. **311**(5759): p. 356-9.

170. Guo, X., et al., *Single-molecule devices as scaffolding for multicomponent nanostructure assembly.* Nano Lett, 2007. **7**(5): p. 1119-22.

171. Weizmann, Y., D.M. Chenoweth, and T.M. Swager, *Addressable Terminally Linked DNA-CNT Nanowires.* Journal of the American Chemical Society, 2010. **132**(40): p. 14009-14011.

172. Mokari, T., et al., *Selective growth of metal tips onto semiconductor quantum rods and tetrapods.* Science, 2004. **304**(5678): p. 1787-90.

173. Salant, A., E. Amitay-Sadovsky, and U. Banin, *Directed self-assembly of gold-tipped CdSe nanorods.* Journal of the American Chemical Society, 2006. **128**(31): p. 10006-10007.

174. Couderc, S., V. Blech, and B. Kim, *New Surface Treatment and Microscale/Nanoscale Surface Patterning Using Electrostatically Clamped Stencil Mask.* Japanese Journal of Applied Physics, 2009. **48**(9).

175. Horcas, I., et al., *WSXM: a software for scanning probe microscopy and a tool for nanotechnology.* The Review of scientific instruments, 2007. **78**(1): p. 13705.

176. Vazquez-Mena, O., et al., *Analysis of the blurring in stencil lithography.* Nanotechnology, 2009. **20**(41): p. 415303.